

**Spectroscopy and characterisation of high  
multipolarity transitions depopulating the  
metastable state in  $^{53}\text{Fe}$**

**Thomas Palazzo**

**A thesis submitted for the degree of  
Master of Philosophy  
The Australian National University**

**December, 2017**

# Preface

---

This work describes an investigation of the high multipolarity transitions depopulating the metastable state in  $^{53}\text{Fe}$ . The idea for this project arose in discussions between Prof. A. E. Stuchery, Dr T. Kibedi, Dr F. G. Kondev and Prof. P. Regan after listening to a talk given by Prof. B. A. Brown (who subsequently provided shell model calculations for this project). Dr. G. J. Lane proposed the methodology using the  $^6\text{Li} + ^{51}\text{V}$  reaction and the fact that  $^{53m}\text{Fe}$  has a unique lifetime separate from the other mostly long-lived activities. The spectroscopic measurements were performed at the Australian National University using the 14UD Pelletron accelerator and the CAESAR array. Successful operation of the experiments relied upon help from Dr. G. J. Lane, Dr. A. J. Mitchell, Dr. M. W. Reed, Prof. A. E. Stuchbery, Mr A. Akber and Mr M. S. M. Gerathy. Parts of the experimental analysis was performed by the author using computer codes developed by a number of people over many years. The shell model calculation presented in Chapter 5 was performed by Prof. A. E. Stuchbery.

The paper:

- High-spin spectroscopy and shell-model interpretation of the  $N < 126$  radium isotopes  $^{212}\text{Ra}$  and  $^{213}\text{Ra}$

presented in the appendix of this work was written during the course of the present work, with contributing authors as listed. The shell-model interpretation presented in the discussion of this paper was developed with the help of Prof. A. E. Stuchbery in the drafting of the paper.

# Declaration

---

Except where acknowledged in the customary manner, the material presented in both the first and corrected editions of this thesis is original, and has not been submitted in whole or part for a degree at any other university.

Thomas Palazzo December, 2017

# Acknowledgements

---

Before I begin I would like to thank the Department of Nuclear Physics and the Research School of Physics and Engineering for awarding me the scholarship that has allowed me to complete this work.

Another year another thesis. A profuse thank you to the members of my supervisory panel: Greg Lane, Andrew Stuchbery, AJ Mitchell, Tibor Kibedi and Matt Reed - your help has been invaluable over the past one and a bit years, thank you for your assistance and **perseverance**. I have learned a lot over the course of this degree and while I am sure my radware skills will be transferable to all areas of aerospace engineering the most important experience of this whole degree was watching my supervisors get completely trashed at INPC and embark on a three hour karaoke binge. In all seriousness... No, who am I kidding, that takes the cake.

To my friends Camilla and Ken – thank you for distracting me with the occasional lunch and picking my brain for Game of Thrones theories. Aqeel – I am sure that hour-long discussions of coffee brew techniques and bean varieties enhanced my productivity at some point. I am sorry for what I am about to do but you must understand: it was mine by rights. Anika – the use of your ridiculously nice house (ah, the perks of still living with the parents), continuous supply of snack foods and constant injections of gossip helped me go from a three-chapter skeleton to a five-chapter draft. Frank and Ellen – although you both have the capacity to drive me insane (not allowing time for meals when scheduling activities on holidays is not okay, Frank), this thesis would not have been possible without your friendship. Ellen, I wish you the best of luck in your thesis writing and Frank, I expect you to take me flying in your plane as soon as you get your license.

Finally, I would like to thank my family. Thank you for cooking most of my meals

towards the end and then driving me home afterward with neatly packed leftovers. Thank you for the wisdom and advice that was instrumental in the completion of this work and thank you for the terrifying Australian Defence Force stories that have kept me amused throughout the year. Good luck with the transition from city folk to hobby farmers and please take good care of my cat. Congrats on moving to the most contested electorate in Australia, I am sure the perks will be endless.

And to Jane, I made it to the end because of you. Thank you for being the most elegant creature in the world.

Oh and Greg, good luck finding the Gnome.

# Abstract

---

This thesis reports the observation of high multipolarity transitions depopulating the  $T_{1/2} = 2.54$  minute,  $J^\pi = 19/2^-$  state in  $^{53}\text{Fe}$ , populated via the  $^{51}\text{V}(^6\text{Li},4\text{n})$  and  $^{24}\text{Mg}(^{32}\text{S},2\text{pn})$  reactions at 50 and 90 MeV, respectively. Excited states were populated using beams pulsed on multi-minute timescales delivered from the ANU 14UD accelerator, with  $\gamma$ -ray decays collected over 20 minute cycles. A time subtraction of the latter 10 minutes of data collection from the first 10 minutes, obtained relatively clean spectra, free from background contamination. Sum-coincidence contributions to the weak E6 and M5 decay branches have been quantified using two different detector geometries, while several methods for the estimation and measurement of sum-coincidence intensity have been employed, obtaining final  $\gamma$ -ray branching ratios of 0.0059(7) and 0.0112(7) for the E6 and M5 transitions, respectively. A comprehensive review of E4, M5 and E6 transitions in atomic nuclei has been attempted and the nature of these transitions has been discussed within the shell model framework.

# Contents

---

<b>Declaration</b>	ii
<b>Acknowledgements</b>	iii
<b>Abstract</b>	v
<b>1 Chapter 1</b>	
<b>Introduction and background theory</b>	1
1.1 Prior studies of $^{53}\text{Fe}$ . . . . .	5
1.1.1 Observation of the E6 branch . . . . .	5
<b>2 Chapter 2</b>	
<b>Experimental methods</b>	8
2.1 The CAESAR Array . . . . .	8
2.1.1 Data acquisition methods . . . . .	9
2.1.2 Data sorting techniques . . . . .	12
2.1.3 CAESAR efficiency . . . . .	14
2.2 Gamma-ray summing . . . . .	15
2.2.1 Sum-coincidences from direct calculation – Theoretical method (TM) . . . . .	17
2.2.2 Measuring sum-coincidence intensity from the 2029-keV transition – Sum-coincidence method (SM) . . . . .	20

2.2.3	Measuring sum-coincidence intensity from the change in detector geometry – Geometric method (GM) . . . . .	21
2.3	Monte Carlo simulations of $^{53m}\text{Fe}$ decay . . . . .	22
<b>3</b>	<b>Chapter 3</b>	
	<b>Analysis and results</b>	<b>25</b>
3.1	Experiment summaries . . . . .	26
3.1.1	March experiment . . . . .	27
3.1.2	May experiments . . . . .	28
3.1.3	December experiment . . . . .	32
3.2	Experimental results . . . . .	32
3.2.1	Initial results . . . . .	32
3.2.2	Measuring sum-coincidence intensities . . . . .	35
3.2.3	Measuring $^{53m}\text{Fe}$ state branching ratios . . . . .	41
3.3	Investigation of inconsistent transition intensities . . . . .	41
3.3.1	Investigating the effects of count rate, detector position and efficiency . . . . .	46
<b>4</b>	<b>Chapter 4</b>	
	<b>Monte Carlo simulation of <math>^{53m}\text{Fe}</math> decay</b>	<b>56</b>
4.1	Simulation conditions . . . . .	57
4.2	Simulation results and comparison to experiment . . . . .	60
<b>5</b>	<b>Chapter 5</b>	
	<b>Discussion</b>	<b>67</b>
5.1	Experimental transition strengths . . . . .	67
5.2	Shell-model calculations . . . . .	68
5.2.1	Model spaces and interactions . . . . .	68
5.3	Shell-model interpretation of high-multipolarity transitions . . . . .	70

---

<b>6 Chapter 6</b>	
<b>Conclusions and future outlook</b>	<b>78</b>
<b>Appendices</b>	<b>80</b>
<b>A J624 operation</b>	<b>81</b>
<b>B Raw experimental values</b>	<b>83</b>
<b>C A method for correcting the sulfur-magnesium transition intensities</b>	<b>85</b>
<b>Paper: High-spin spectroscopy and shell-model interpretation of the</b>	
<b><math>N &lt; 126</math> radium isotopes <math>^{212}\text{Ra}</math> and <math>^{213}\text{Ra}</math></b>	<b>91</b>
<b>Bibliography</b>	<b>114</b>

# List of Figures

---

1.1	Illustration of the experimentally observed <i>magic numbers</i> . . . . .	3
1.2	Level scheme of $^{53m}\text{Fe}$ as obtained by Black et al . . . . .	4
2.1	Schematic diagram of the CAESAR array . . . . .	10
2.2	Demonstration of a time-subtracted spectrum . . . . .	12
2.3	Absolute efficiency curves for the CAESAR array . . . . .	16
2.4	Example level scheme with three levels. . . . .	17
3.1	Level scheme for $^{53m}\text{Fe}$ from the present work . . . . .	26
3.2	Gamma-ray spectrum of $^{53m}\text{Fe}$ decay obtained by Black et al . . . . .	27
3.3	Statistical model calculations of the products of the $^6\text{Li}+^{51}\text{V}$ reaction. . . . .	30
3.4	Statistical model calculations of the products of the $^{32}\text{S}+^{24}\text{Mg}$ reaction. . . . .	31
3.5	Gamma-ray spectra obtained for the lithium-vanadium and sulfur-magnesium experiments . . . . .	33
3.6	Literature and present experimental values for the 2340-keV state branching ratio. . . . .	36
3.7	Lifetime curves for strong transitions in the decay of $^{53m}\text{Fe}$ . . . . .	44
3.8	Coincidence $\gamma$ -ray spectra for transitions in $^{53m}\text{Fe}$ . . . . .	45
3.9	$\Gamma_{2340}$ plotted against detector position . . . . .	48
3.10	$\Gamma_{2340}$ plotted against detector efficiency . . . . .	48
3.11	$\Gamma_{2340}$ for selected detectors in each run file in the May experiments. .	51

3.12	Overlaid scaled spectra of Detectors 4, 5 and 6. . . . .	53
3.13	Ratio of the peak areas measured in Detector 6 to the areas measured in Detector 4. . . . .	54
4.1	Angular correlations for the 701–2340-keV and 701–1012-keV cascades in $^{53m}\text{Fe}$ . . . . .	58
4.2	3041-keV and 1713-keV transition total intensities plotted as a function of branching ratio for the close geometry. . . . .	62
4.3	3041-keV and 1713-keV transition total intensities plotted as a function of branching ratio for the far geometry. . . . .	63
5.1	Comparison of experimental and calculated excited state energies in $^{53}\text{Fe}$ within the $f_{7/2}$ model space. . . . .	71
5.2	Ratio of theoretical to experimental transition strength as a function of the $(f_{7/2})^{-4}(f_{5/2})^1$ admixture in the $J^\pi = 19/2^-$ and $7/2^-$ states. .	77
C.1	Number of counts in each peak plotted against the efficiency of each detector for the (far geometry) sulfur-mangesium data . . . . .	87
C.2	Number of counts in each peak plotted against the efficiency of each detector for the (close geometry) lithium-vanadium data . . . . .	88
C.3	Counts in the 1328-keV peak following the application of scaled-redistribution coefficients to the data. . . . .	90

# List of Tables

---

1.1	Transition energies and intensities relative to the 701-keV transition obtained in the prior works by Black et al. . . . . .	7
2.1	Positions of the HPGe detectors in spherical polar coordinates in the CAESAR array. . . . .	9
3.1	Products of the $^{51}\text{Va}(^{6}\text{Li}, 4\text{n})^{53}\text{Fe}$ and $^{24}\text{Mg}(^{32}\text{S}, 2\text{pn})^{53}\text{Fe}$ reactions. . . . .	29
3.2	Normalised intensities of $\gamma$ rays emitted in the decay of the $J^\pi = 19/2^-$ isomer in $^{53}\text{Fe}$ . . . . .	34
3.3	Gamma ray branching ratios for the 2340-keV state from each of the measurements in this work and values from the literature . . . . .	35
3.4	Ratios of transition intensity between each geometry for real and sum peaks, respectively. . . . .	37
3.5	Experimentally measured peak areas for each peak with a sum-coincidence component as well as the number of sum-coincidence events evaluated according to the GM and SM. . . . .	38
3.6	Number of sum-coincidence counts predicted using the TM and scaled TM (see text for description) in each peak . . . . .	38
3.7	Measured $\gamma$ -ray branching ratios, obtained using the lithium-vanadium data, for the 3041-keV and 2340-keV states in $^{53m}\text{Fe}$ , accounting for the subtraction of sum-coincidence events. . . . .	42
3.8	Intensity balances for the 1328- and 2340-keV states for each experiment	43

---

3.9	$\gamma$ -ray intensities measured in run file 12 for each of the detectors. . . . .	49
3.10	Peak areas obtained for lines in $^{53m}\text{Fe}$ decay with Detectors 4, 5 and 6 following the normalisation discussed in the text. . . . .	52
4.1	Input branching ratios for the decay from the $J^\pi = 19/2^-$ state used in each simulation. . . . .	59
4.2	Angular correlation at $0^\circ$ for each of the possible $\gamma$ -ray cascades in $^{53m}\text{Fe}$ . . . . .	59
4.3	Comparison of simulation results with and without the effects of angular correlations. . . . .	60
4.4	Ratio of simulated to experimental counts measured for each real and sum-coincidence peak in $^{53m}\text{Fe}$ , for the close geometry, as a function of the input branching ratios. . . . .	60
4.5	Ratio of simulated to experimental counts measured for each real and sum-coincidence peak in $^{53m}\text{Fe}$ , for the far geometry, as a function of the input branching ratios. . . . .	61
4.6	Sum-coincidence component of $^{53m}\text{Fe}$ decay peaks averaged over all of the simulations. . . . .	66
5.1	Experimental strengths of the E4, M5 and E6 transitions obtained by Black et al and from the present work . . . . .	68
5.2	Shell model interactions used in the sampled literature for calculation of high multipolarity transition properties . . . . .	69
5.3	The results of $2^+ \rightarrow 0^+$ and $4^+ \rightarrow 0^+$ calculations performed by Jaqaman and Zamick using the SII interaction. . . . .	72
5.4	Table of experimental and theoretically calculated E4 transition strengths taken from Gadea et al . . . . .	72
5.5	Summary of matrix elements for a number of different interactions and model spaces . . . . .	74

A.1	Possible time windows produced using the default J624 clock settings and clock frequencies. . . . .	82
B.1	Raw experimental peak areas for the far geometry as measured in the three moveable detectors. The total detection efficiency at that energy is also included for reference. . . . .	83
B.2	Raw experimental peak areas for the close geometry as measured in the three moveable detectors. The total detection efficiency at that energy is also included for reference. . . . .	84
C.1	Redistribution coefficients for the sulfur-magnesium experiment in the far geometry . . . . .	86
C.2	Redistribution coefficients for the lithium-vanadium experiment in the close geometry . . . . .	86
C.3	Scaled redistribution coefficients for the sulfur-magnesium experiment in the far geometry . . . . .	89
C.4	Intensities of transitions in $\text{Fe}^{53m}$ . . . . .	90

# 1

## Chapter 1

# Introduction and background theory

---

Nuclear physics as a field sits at the intersection of every major area of physics. The nucleus itself is a quantum mechanical object whose interactions with the universe around it are governed by both the modern theories of quantum mechanics and relativity as well as the more classical pictures of mechanics and electromagnetism. Nuclear science has far-reaching implications spanning many orders of magnitude, from the study of the smallest fundamental particles to the cosmic creation of the elements in nucleosynthesis. On more human scales, nuclear physics applied to medicine has led to many breakthroughs which today are commonplace; medical imaging devices and cardiac pacemakers are examples [Kra87].

Nuclear theory usually considers the nucleus as a collection of interacting nucleons (protons and neutrons) bound together; to understand the nucleus is thus to understand the interactions between constituent nucleons. This is not as simple as it may sound, taking a first-principles approach and modeling all of the nucleon-nucleon interactions becomes computationally prohibitive beyond  $A \approx 12$ . After

the addition of a few nucleons, the number of possible interacting pairs increases combinatorically. Thus, nuclear physicists have relied on approximations to drastically reduce the computational space. The nuclear shell model [May49] is one of many such approximations with a strong empirical backing. Analogous to the atomic shell model, whereby electrons occupy shells, with set capacity, and which become fully occupied at the noble gases, the nuclear shell model explains the structure of the nucleus in terms of the interaction and movement of valence nucleons or, nucleon holes, within analogous nuclear shells outside of an inert core. Empirical evidence of shell structure is manifold. For example, it can be seen when the binding energy per nucleon (generally associated with stability) of every nucleus is plotted as a function of proton and neutron number. This is shown in Figure 1.1, where the colour scale indicates the binding energy per nucleon of the nucleus. The regions of high binding energy that occur at  $N$  or  $Z$  equal to 2, 8, 20, 28, 50, 82 and  $N = 126$ , sometimes called magic numbers, define the closed (or filled) shells, that form the basis of the shell model. Within a given nucleus, the excited states and transitions between them can be understood through the interaction and movement of valence nucleons in orbitals around the inert core.

Through studying the  $\gamma$ -ray transitions emitted in the decay of an excited nucleus, structural information about that nucleus can be obtained. Excited states in the nucleus have a well defined energy, spin and parity produced from the coupling of the valence nucleons to one another and from their interactions with the core. Transitions between excited states generally occur via the emission of  $\gamma$  rays, which carry angular momentum ( $L$ ) determined by the difference in angular momentum between the excited states and are constrained by various conservation laws. They can be either magnetic or electric in nature, depending on the parity of the initial and final states in the decay. In the context of the shell model, transitions can be understood as a re-coupling of the angular momentum of valence nucleons within orbitals, or as the movement of one or more nucleons between orbitals.

The angular momentum change between excited states gives detailed information on the configurations of the nucleons. Across the nuclear landscape, transitions carrying 1 or  $2\hbar$  units of angular momentum are common. Electric quadrupole

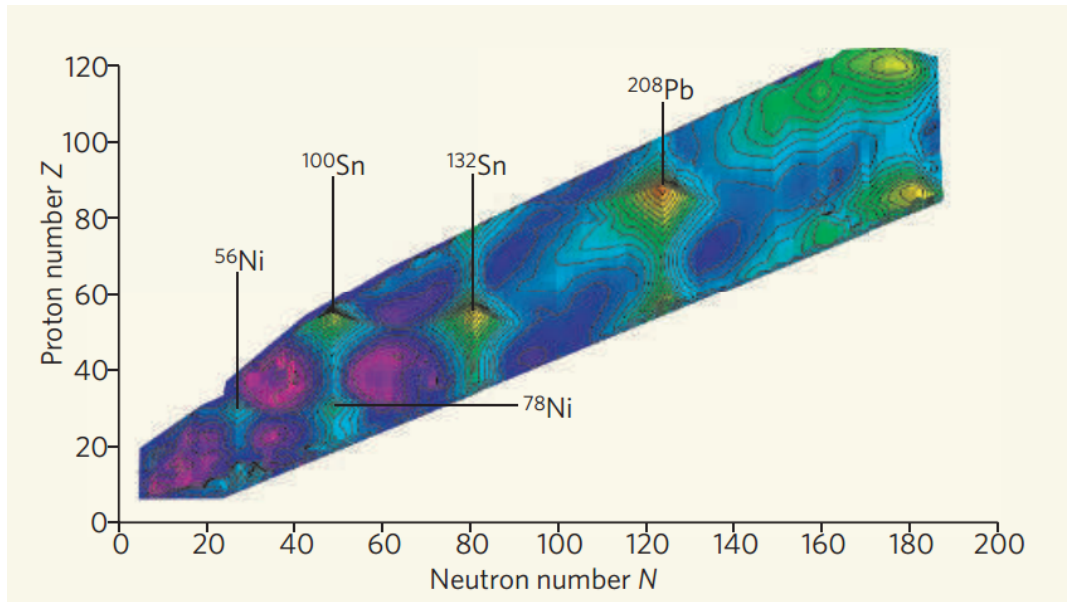


**Figure 1.1:** The islands of stability. The colour spectrum from violet through green to yellow and to red indicates the changing binding energy per nucleon from less to more bound. The magic numbers at, for example, 28, 50, 82 and 126 are evidenced by the ridges and islands at specific nucleon numbers. Picture taken from Ref. [Ben07].

( $L = 2$ ) transitions are often seen as a signature for the movement away from shell-model individual particle motion into more collective structures pictured as rotations or vibrations. On the other hand, high angular momentum transitions (generally speaking, transitions carrying more than  $2\hbar$  of angular momentum) are rare and provide special windows into the nuclear structure. For example, nuclei in the vicinity of the  $^{208}\text{Pb}$  double closed shell are known to exhibit strong E3 transitions arising from the coupling of excited states to the octupole vibration in  $^{208}\text{Pb}$  [Stu92, Pal17, Dra08]. At higher angular momentum still, spin-gap isomers and *yrast* traps occur where the available particle excitations give rise to E4 or even E5 transitions [Gad05, Soo95]. Such instances are few and far between; in approximately 3000 known nuclei only 47 E4 transitions are known. This number drops to 24 for E5 transitions and is even lower for the M5 magnetic counterparts. Most elusive, however, is the E6 transition in  $^{53}\text{Fe}$ , of which there is only one example suggested to have been observed across the entire nuclear landscape.

The nucleus  $^{53}\text{Fe}$  is two protons and one neutron removed from the doubly magic  $N = 28, Z = 28$  closed shells at  $^{56}\text{Ni}$ . It is a notable nucleus, not only for the

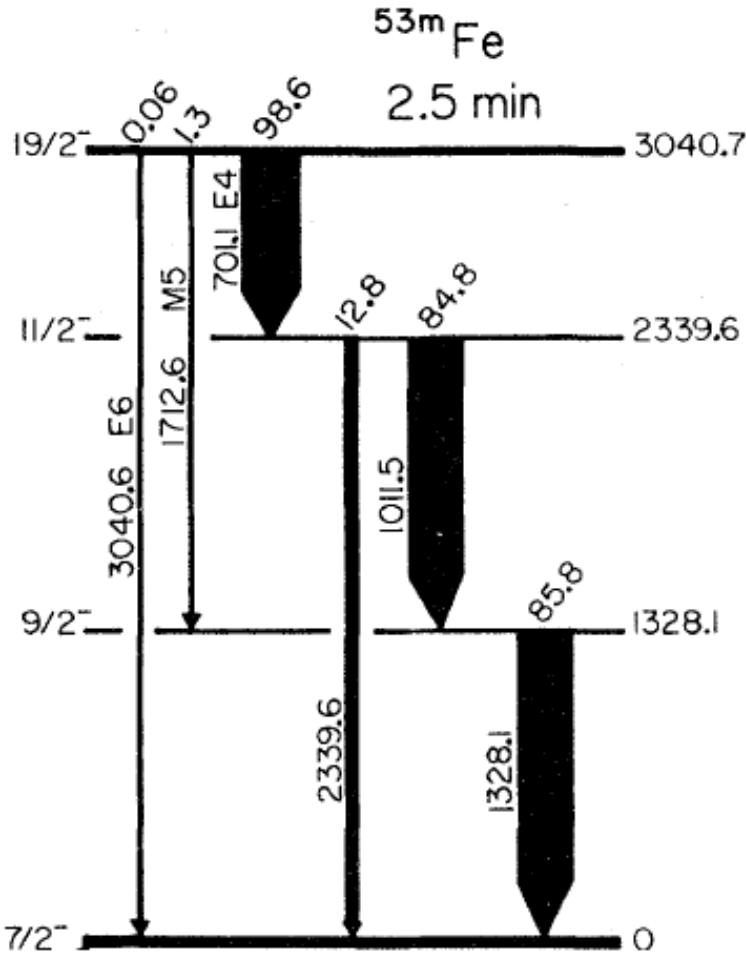


**Figure 1.2:** Level scheme of  $^{53m}\text{Fe}$  as obtained by Black et al [Bla75].

potential E6 transition between the  $J^\pi = 19/2^-$  and  $7/2^-$  states, but for the E4 and M5<sup>1</sup> transitions also depopulating the  $J^\pi = 19/2^-$  spin-gap isomer. Whether the E6 transition actually exists is open to question. It is an extraordinarily weak decay branch, taking only 0.06% of the total decay of the  $J^\pi = 19/2^-$  state [Bla75] (see the level scheme in Figure 1.2 for further details). Consequently, it is possible that the branch is not in fact real and the ‘observed’  $\gamma$  ray may occur artificially as the energy sum of the transitions in cascade in the detector due to the short lifetimes of the intermediate states. This thesis will attempt to rule definitively whether or not the high-multipolarity E6 transition in  $^{53}\text{Fe}$  exists.

<sup>1</sup>The 1713-keV M5 transition is potentially the only known M5 transition across the nuclear chart as the only other M5 assignments in  $^{31}\text{P}$  are not observations but rather limits on the intensities of the transitions [Oue13].

## 1.1 Prior studies of $^{53}\text{Fe}$

$^{53}\text{Fe}$  has been the subject of numerous experimental and theoretical studies. Early experimental work in the late 1950s measured the half-life of the  $^{53}\text{Fe}$  ground state and deduced the resulting  $\gamma$  rays and level schemes populated in  $^{53}\text{Mn}$  following its  $\beta$  decay [Jul59]. In 1971, Black et al [Bla71] first reported on the existence of the E6 and M5 branches depopulating the  $J^\pi = 19/2^-$  state (level scheme shown in Figure 1.2). This work was later followed up in 1975 by the same authors with a more comprehensive presentation of the  $\gamma$  and  $\beta$  decay in the  $^{53m}\text{Fe}$  level scheme [Bla75]. In an unpublished thesis by D. Geesaman [Gee76], the E6 transition was also observed and similar conclusions to Black et al were drawn. Parallel to this, many *low-spin* studies of the  $\gamma$  rays populated in-beam (thus excluding the immediate decays from the  $J^\pi = 19/2^-$  isomer) were reported in Refs. [Coc71, Nel73, Saw73]. Both Sawa [Saw73] and Nelson [Nel73] measured mixing ratios for the 1012-keV,  $J^\pi = 11/2^- \rightarrow 9/2^-$  and 1328-keV,  $J^\pi = 9/2^- \rightarrow 7/2^-$  M1 transitions, while Cochavi et al [Coc71] reported on the existence of a cascade parallel to the 1012–1328-keV cascade and measured the lifetime of a new isomeric state at 741-keV. Later, *high-spin* studies by Rietz et al [Rie05] greatly extended the known level scheme, observing two main components: one feeding the  $J^\pi = 19/2^-$  state, and one bypassing it completely. Theoretical interpretations of the  $^{53m}\text{Fe}$  decay structure are few, and most have focused on the existence of the E6 branch [Bro11, Glo75], however, Metsch et al calculated transition strengths and state excitation energies for the entirety of the  $^{53m}\text{Fe}$  decay [Met81]. These works and the theoretical interpretation of the  $^{53m}\text{Fe}$  decay scheme will be discussed in greater detail in Chapter 5.

### 1.1.1 Observation of the E6 branch

The 1971 and 1975 publications by Black et al provided the first experimental evidence for the M5 and E6 transitions depopulating the  $J^\pi = 19/2^-$  metastable state. The level scheme and transition intensities relative to the 701-keV transition,

---

for each work, are shown in Figure 1.2 and Table 1.1. There is a remarkable difference in the reported transition intensities, for example, the 3041-keV E6 transition intensity is a factor of three larger in the later work.

Black et al cite several pieces of evidence that the M5 and E6 peaks are real transitions. Primarily, they point towards the lack of a measurable 2029-keV sum-coincidence peak (between the 701-keV and 1328-keV transitions) as evidence that sum events were not a significant component of the data, commenting that between several repeat measurements, using different detector geometries, a 2029-keV sum-coincidence peak was never observed [Bla75]. On top of this, lifetime measurements for the 1713-keV M5 and 3041-keV E6 branches show the same 2.5-minute lifetime as the 701-keV transition depopulating the  $J^\pi = 19/2^-$  isomer. Finally, Black points to the peak widths of the 1713-keV and 3041-keV transitions in the  $\gamma$ -ray spectrum as evidence that no sum-coincidences within the cascade are present as the peak widths are comparable to the other real transitions. Black et al provide no quantitative evidence of any of these arguments, suggesting only that the sum-coincidence proportion of the 1713-keV peak must be close to 0.1% of the total area and 10% of the total 3041-keV peak area. Geesaman observes a similar E6 branching ratio as Black et al of 0.56(10) [Gee76, Bla75], however, he suggests that sum-coincidences make up a much more significant proportion of the peak area (30(10)%).

The experiments conducted as part of this thesis were an attempt to measure the sum-coincidence intensity of the 1713-keV, 2340-keV and 3041-keV  $\gamma$ -decay branches in  $^{53\text{m}}\text{Fe}$  and determine if the high-multipolarity transitions depopulating the  $J^\pi = 19/2^-$  metastable state are in fact real decays and not sum-coincidence events. The following chapters will outline the experimental methodology used to obtain a measurement of the 3041-keV E6 branching ratio (Chapter 2), report on the analysis of these data and the results of these experiments (Chapter 3) and interpret the experimental results in the context of a Monte Carlo simulation of  $^{53\text{m}}\text{Fe}$  (Chapter 4). The experimental results are discussed with reference to a number of theoretical and experimental works on high-multipolarity decays in Chapter 5.

**Table 1.1:** Transition energies and intensities relative to the 701-keV transition obtained in the prior works by Black et al [Bla71, Bla75]. Note the large difference in the reported intensities as described also in the text.

[Bla71]		[Bla75]	
$E_\gamma$	$I_\gamma$	$E_\gamma$	$I_\gamma$
701.0(1)	$\equiv 100$	701.1(1)	$\equiv 100$
1011.5(1)	86(9)	1011.5(1)	86(9)
1328.1(1)	97(10)	1328.1(1)	87(8)
1712.6(3)	0.7(1)	1712.6(3)	1.3(1)
2339.6(1)	13(2)	2339.6(1)	13(2)
3040.6(5)	0.020(5)	3040.6(5)	0.06(1)

# 2

## Chapter 2

## Experimental methods

---

The principal motivation for this work was to provide experimental confirmation of the E6 transition in  $^{53m}\text{Fe}$ , with an evaluation of the sum-coincidence contribution to the total peak area. This chapter will describe the experimental apparatus and methods developed to achieve this aim.

### 2.1 The CAESAR Array

The Compton-suppressed array (CAESAR) of the Heavy Ion Accelerator Facility (HIAF) at the Australian National University (ANU) features nine Compton-suppressed high-purity germanium (HPGe) detectors, three of which are placed on rails allowing movement of the detectors radially outward from the target position. The remaining six HPGe detectors are fixed in the vertical plane, through the beam axis. A schematic diagram of the six detector arrangement is shown in Figure 2.1. Alternate configurations of the array feature two low-energy photon spectrometers (LEPS) for enhanced energy resolution and detection efficiency of low-energy photons, and between four and six lanthanum bromide ( $\text{LaBr}_3$ ) detect-

**Table 2.1:** Positions of the HPGe detectors in spherical polar coordinates in CAESAR oriented such that detectors one through six are positioned in the vertical plane perpendicular to the beam axis. Detector distances ( $r$ ) from the target chamber are approximate. In this work, detectors 7, 8 and 9 were used in two geometries, one with the detectors at the positions given in the table below (close geometry) and the other with the detectors pulled backwards a distance of 3.5 cm (far geometry).

Detector	$r$ (cm)	$\theta$ (°)	$\phi$ (°)
1	~ 12	145	90
2	~ 12	97	90
3	~ 12	48	90
4	~ 12	146	270
5	~ 12	98	270
6	~ 12	50	270
7	~ 17	53	172
8	~ 17	132	168
9	~ 17	49	0

ors for fast-timing measurements. For the purpose of the  $^{53m}\text{Fe}$  measurement, only the HPGe detectors are of interest as the  $\gamma$ -ray energy and level lifetime scales that are associated with the  $^{53m}\text{Fe}$  decay limit the usefulness of LEPS or  $\text{LaBr}_3$  detectors. The angular positions of the HPGe detectors are shown in Table 2.1.

### 2.1.1 Data acquisition methods

#### Compton suppression

Compton scattering occurs when an incident  $\gamma$  ray in the detector scatters off an atomic electron of the absorbing material, creating a scattered photon with reduced energy and a recoiling electron. The electron recoil can deposit its energy in the active detector volume, while the scattered photon can escape. The partial absorption of the  $\gamma$ -ray energy gives rise to a continuous background in the collected  $\gamma$ -ray spectrum up to the energy of the Compton edge. Compton associated background can obscure low-intensity peaks of interest, and as such presents an obstacle to  $\gamma$ -ray spectroscopy. In CAESAR, suppression of Compton events is performed by surrounding the HPGe detectors with bismuth germanate (BGO) suppressors. The high Z of bismuth leads to a high interaction (and detection) probability for the scattered  $\gamma$  rays. When an event in the suppressor is detected in coincidence with

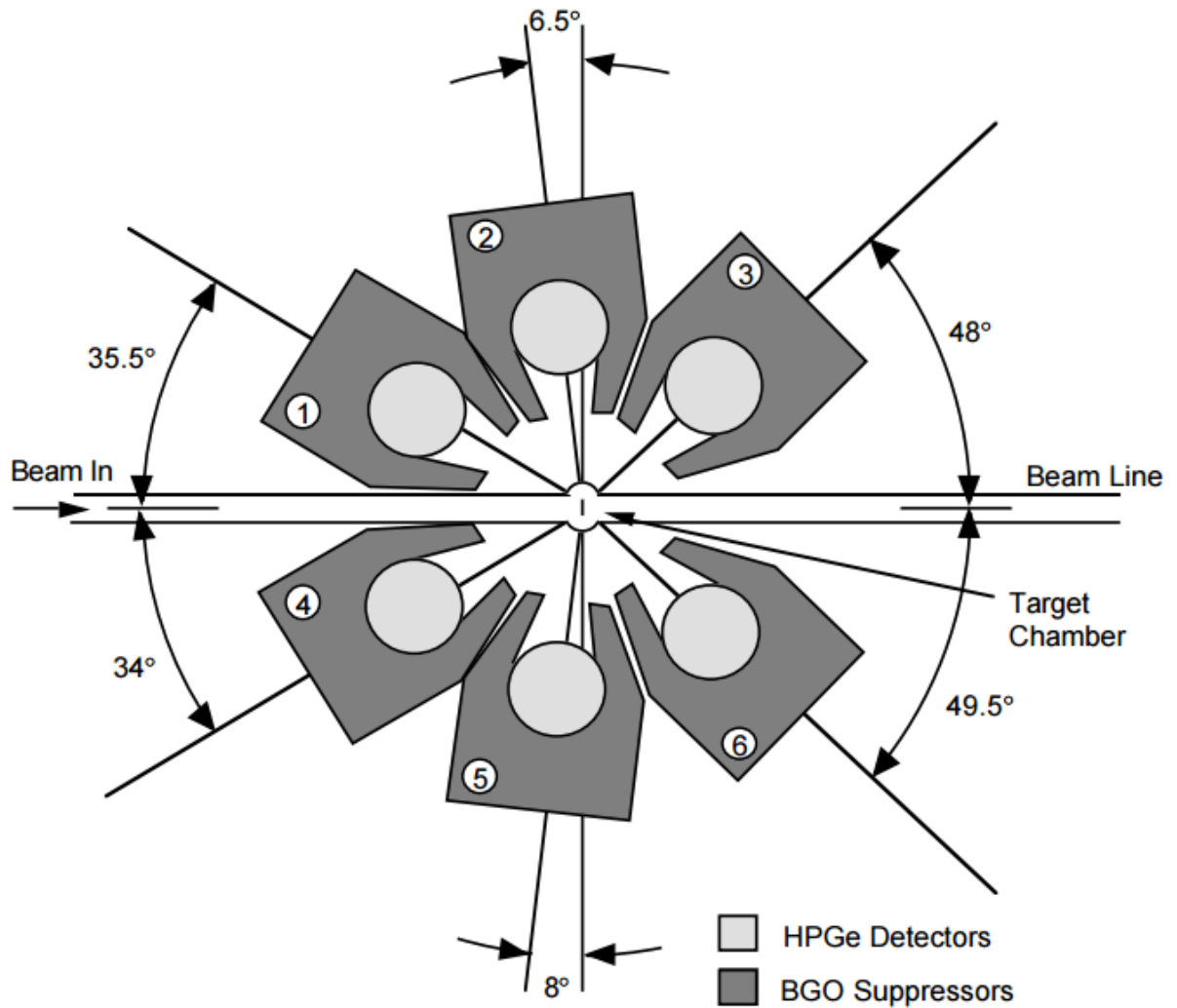


**Figure 2.1:** Schematic diagram of the six Compton-suppressed, fixed position, HPGe detectors in the CAESAR array. These detectors, aligned perpendicular to the beam axis and in the vertical plane ( $\phi = 90^\circ$  and  $270^\circ$ ) at the angles shown, may be used for angular correlation measurements and account for approximately 50% of the total HPGe efficiency of the array. The remaining three HPGe detectors lie approximately in the plane through the beam axis and perpendicular to the page; their positions are shown in Table 2.1.

an event in the HPGe detector, the detection logic vetoes the event and nothing is recorded. In doing so, the efficiency of each detector is reduced, however, the Compton background is almost totally removed from the spectrum.

### **The J624 module and event collection protocol**

The J624 module is used in conjunction with the data acquisition system for CAESAR. It provides a time stamp as ADC event data are transferred to the interface. The module is essentially a clock that labels events over a period of time before resetting back to time-zero after it receives a reset pulse. The reset is usually set to match the beam pulsing so as to collect events between successive beam bunches. Alternatively, it may be driven by a 5V voltage signal of the desired frequency. The default clock range varies from 2.1 ms to 5.8 hours over 8192 channels (13 bits of resolution). An external clock to produce arbitrarily long or short time-spectrum widths can be used, however, this functionality was not required for the timescales of the present work.

In this experiment, the J624 was used to time-stamp decay events over a 2621-second range. A DC beam was used to irradiate the target for about three half-lives of the metastable state in  $^{53m}\text{Fe}$  (7.5 minutes in total). The beam was taken off target by inserting a Faraday cup and decay data were collected for eight half-lives (20 minutes). After this period the cup was removed, triggering the reset pulse for the J624 clock and re-initiating the irradiation of the target. By gating on different time regions of the J624 spectrum, short-lived or long-lived reaction products can be isolated. Subtraction of the constant (on these time scales) background due to long-lived reaction products was performed by subtracting the second half of the J624 time spectrum (a 10-minute gate) from the first half. Figure 2.2a shows an example J624 spectrum of the decay from the irradiated target in this experiment, along with the time gates used for subtraction of the long-lived activity. The  $^{53m}\text{Fe}$  present in the final 10 minutes of data collection constitutes 6% of the total populated at the time the beam is turned off, so the number of  $^{53m}\text{Fe}$  decay events lost in the subtraction is not appreciable, while the vast majority of the decay lines due to the activity build up are removed. This process is illustrated in panels (b) and (c)

of Figure 2.2 and will be described in more detail in the Chapter 3. The method for calculating the time per channel as well as the full spectrum widths using the default clock settings and an example of the long, beam-pulsing script are shown in Appendix A.

### 2.1.2 Data sorting techniques

Raw event data collected with a  $\gamma$ -ray singles trigger using the CAESAR array were written into run-files which were stored locally on a server. This process divided the collected data into smaller segments, that can be used to correct for gain shifts that may occur over time. No set time was used for run files. They were closed and opened at times convenient for the flow of the experiment, such as between shift changeovers, or during beam-tuning or target cycling; the use of small raw data

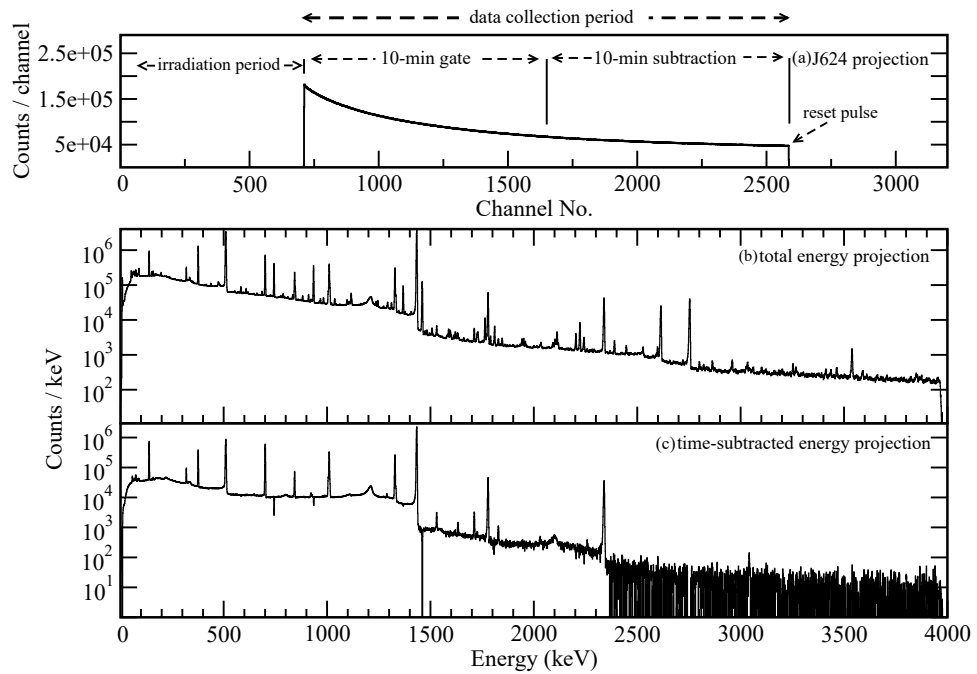


**Figure 2.2:** (a) J624 histogram with time gates indicated. (b) Total energy projection prior to time subtraction. (c) Time-subtracted spectra using a gate on the first 10-minutes of data collection and subtracting the final 10-minutes.

files allows for easy on-line monitoring, sorting and gain matching of the data.

### **Detector calibration**

The gain of each amplifier was set so that all nine of the detectors used 1-keV/channel energy scales. With the 12-bit resolution of the ADCs, this gave a 4-MeV energy range. Rough matching of the analogue signals was achieved with the amplifier settings; however, detailed matching of the detector gains was performed offline using spectra from  $^{152}\text{Eu}$  and  $^{56}\text{Co}$   $\gamma$ -ray sources to calibrate the detector gains to match known photo-peak energies. Further adjustments were subsequently performed to each individual run-file using two photo-peaks, one at low energy and one at high energy, to accommodate any gain shifts during the experiment. In this work, the 140-keV  $^{75}\text{Ge}$  line, produced in the neutron activation of the 26% abundant  $^{74}\text{Ge}$  present in the natural germanium of the detector, and the 2614-keV thorium-decay-series background line, were used to gain match between these energies. There were no strong lines above 2614-keV to reliably gain match, consequently, some gain mismatches at the 3041-keV peak may occur, however, the error that can occur over the  $\sim$ 400-keV extrapolation should be minor.

### **Matrix construction for off-line analysis**

The raw data collected were sorted in many different ways depending on the analysis required. Singles data were usually sorted into a matrix with the J624 spectrum on one axis and the  $\gamma$ -ray energy (usually the sum of all the detectors or an individual detector) on the other. This matrix allowed subtraction of long-lived activity by gating on and subtracting selected time regions in the J624 spectrum. The J624- $\gamma$  energy matrix could also be projected to perform lifetime measurements. By gating on an energy region and projecting the matrix onto the J624 axis, a histogram of  $\gamma$ -ray counts against time after the beam was switched off could be produced.

For  $\gamma$ - $\gamma$  coincidence data matrices, the energy of a detected  $\gamma$ -ray event was sorted on one axis and the energies of  $\gamma$  rays coincident with it were placed on the other.

The  $\gamma$ - $\gamma$  coincidence matrices can be sorted in a variety of ways to extract information by gating on different time regions within and after a beam pulse. *Prompt* matrices can be produced by selecting  $\gamma$ -rays detected immediately around the beam pulse, while *isomeric decay* is isolated by gating later in time after the beam pulse (*out-of-beam*). Decay above and below isomeric states can be differentiated by gating on a transition created in the decay of an isomer and projecting coincident events detected *early* in time with respect to the *delayed* gating transition, or vice versa. As the beam pulses were several minutes wide in these experiments, correlation of decay above and below the metastable state in  $^{53}\text{Fe}$  was impossible and, therefore, essentially all analysis was performed using long, *out-of-beam* time cuts with no need for *prompt* or *early-delayed* matrix construction. The  $\gamma$ - $\gamma$  coincidence data were instead used to rule out side feeding and for measuring the branching ratio of the  $J^\pi = 11/2^-$  state when gating on the 701-keV  $\gamma$ -ray.

### 2.1.3 CAESAR efficiency

Efficiency calibration of the detectors is necessary due to their changing response as a function of energy. In this experiment, two different detector geometries are considered, and an accurate determination of sum contributions to low-intensity decay branches is also required. This necessitates determining the absolute efficiency of the detectors, that is, the absolute probability of detection for a  $\gamma$  ray of particular energy emitted randomly into the total solid angle, rather than just the efficiency of the detectors relative to each other.

Calibration sources of  $^{152}\text{Eu}$  and  $^{56}\text{Co}$  mounted on target frames similar to those used for the  $^{53m}\text{Fe}$  production were placed in the array covering an energy range from 40 keV to 3500 keV. The J624 was switched to a clock frequency such that the total time spectrum counted for six hours across 8192 channels before wrapping around to channel 1 in order to precisely determine the collection times for each source. Event data were recorded to track possible gain shifts in the detectors. Peak areas were fitted using a Gaussian function above a background with tail and step components when appropriate. The measured number of counts in each

peak was normalised against their relative intensity to produce a relative efficiency curve as a function of energy  $x$  (in keV) with a form described in the Radware<sup>1</sup> documentation [Rad95]:

$$\epsilon(x) = \text{Exp}([a+b\log(\frac{x}{100})+c\log(\frac{x}{100})^2]^{-g}+[d+e\log(\frac{x}{1000})+f\log(\frac{x}{1000})^2]^{-g})^{\frac{-1}{g}}, \quad (2.1)$$

where parameters  $a$  through  $c$  and  $d$  through  $f$  fit the curve in two energy regions (100 and 1000 keV scales) to the data points, while parameter  $g$  smooths the intersection between the two curve components. For the detectors that were moved radially outwards in the array, the same efficiency curve was used in both geometries except for a fitted normalisation factor. The absolute activity of the mountable CAESAR calibration sources is unknown and so they had to be compared to calibration sources of known activity. Hence, the CAESAR calibration sources were measured with a lead-shielded (almost background-free) HPGe detector along with a  $^{152}\text{Eu}$  calibration source with activity known to  $\sim 5\%$ . The absolute efficiency of the detector was measured using the known activities and hence the activities of the CAESAR calibration sources were determined. With the activities and collection times known, the relative efficiency measurements could be normalised to an absolute measurement by simple scaling. The absolute efficiency of each individual detector, the sum of all detectors, as well as the sum of just the three moveable detectors in both geometries were measured. Figure 2.3a shows the efficiency curve for the full array of nine HPGe detectors, while Figure 2.3b shows the curve for the three moveable detectors alone when in the close-packed geometry.

## 2.2 Gamma-ray summing

Gamma-ray summing in detectors takes place when two or more  $\gamma$  rays are incident in the same detector in a time window unresolvable by the detector. The energy

---

<sup>1</sup>Radware is a series of programs used for the analysis of  $\gamma$ -ray spectroscopic data.

signals are summed together and instead of detecting two events at energies  $E_1$  and  $E_2$ , a single event at  $E_1 + E_2$  is recorded. For HPGe detectors, the time resolution capabilities make it reasonable to assume that transitions across states with sub-nanosecond lifetimes will be capable of producing sum-coincidence peaks. Detectors placed in a close geometry, by virtue of the percentage of solid angle covered by the detector, will be more susceptible to  $\gamma$ -ray summing. This presents a trade-off when positioning detectors; too close to the  $\gamma$ -ray source and sum-contributions become significant, too far and the efficiency of the system is greatly reduced.

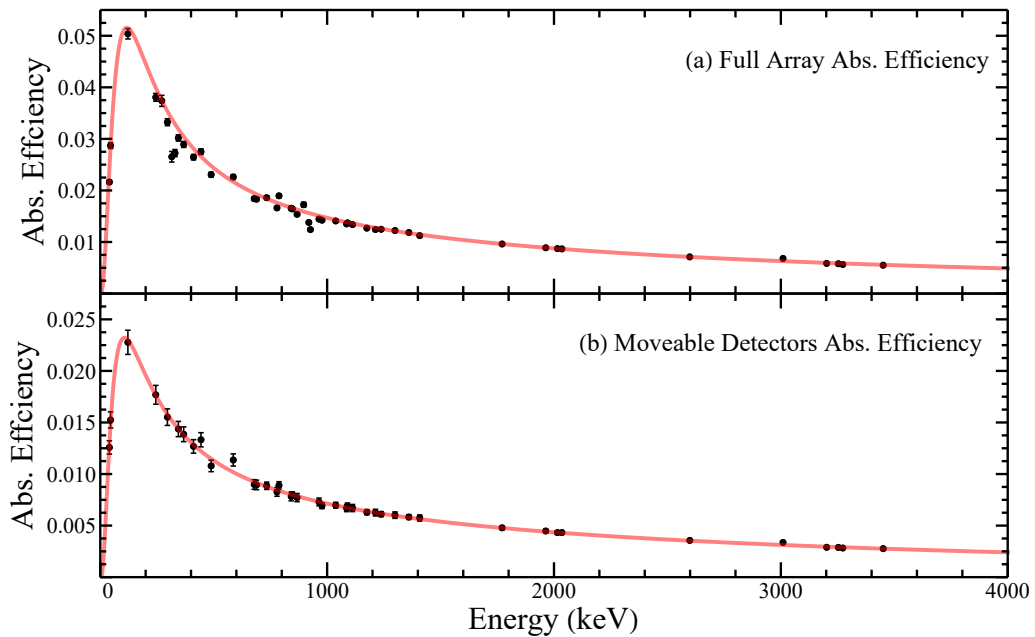


**Figure 2.3:** Absolute efficiency curves for the CAESAR array with (a) all nine HPGe detectors in the close-packed geometry, as well as (b) the three moveable detectors alone in the close geometry. The three moveable detectors in the close geometry account for approximately 50% of the total array efficiency of 1.8% at 700 keV.

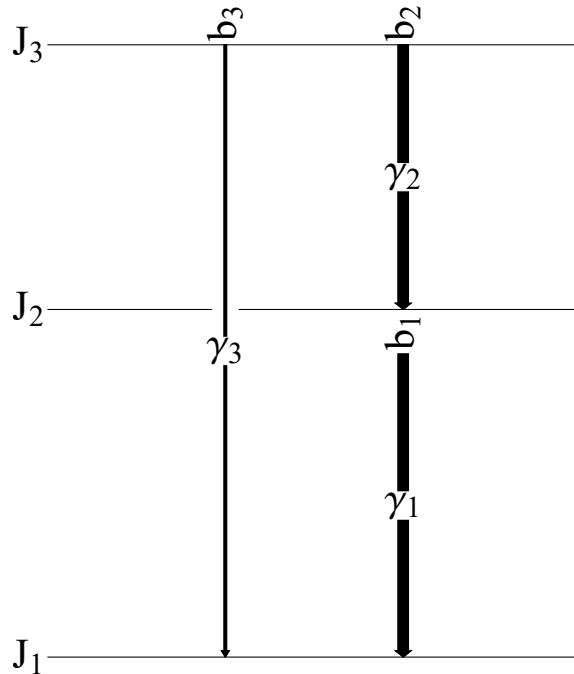


**Figure 2.4:** Example level scheme with three levels. The state  $J_3$  has branching ratios  $b_2$  and  $b_3$  for the transitions  $\gamma_2$  and  $\gamma_3$ , respectively.

### 2.2.1 Sum-coincidences from direct calculation – Theoretical method (TM)

Estimating the sum contributions to the weak M5 and E6  $\gamma$ -ray branches in the  $^{53m}\text{Fe}$  decay scheme is essential to obtain their associated transition strengths correctly. General methods for sum-coincidence estimation are presented in Refs. [Kno10, McC75, Geh77] all of which are largely based on an earlier paper [And72]. For the general three-level system illustrated in Figure 2.4, the peak area of  $\gamma_3$ , denoted  $A'_3$ , including the summing of  $\gamma_1$  and  $\gamma_2$  transitions, can be determined as follows:

$$A'_3 = I_3 \epsilon_3 + I_2 b_1 \epsilon_1 \epsilon_2 \overline{W_{1,2}(\theta)}, \quad (2.2)$$

where  $I_i$  gives the intensity of the transition,  $\epsilon_i$  is the detection efficiency at the

energy of  $\gamma_i$ ,  $b_j$  is the product of the state branching ratios in the branch from  $\gamma_i$  to  $\gamma_j$  and  $\overline{W_{i,j}(\theta)}$  is the angular correlation averaged over the solid angle subtended by the detector. Using these methods, equations for the sum contributions to each of the potential sum peaks in  $^{53m}\text{Fe}$  can be derived and are shown below:

$$A'_{2340} = I_{2340}\epsilon_{2340} + I_{1012}b_{1328}\epsilon_{1012}\epsilon_{1328}\overline{W_{1012,1328}(\theta)} \quad (2.3)$$

$$A'_{2029} = I_{701}b_{1012}b_{1328}\epsilon_{701}\epsilon_{1328}\overline{W_{701,1328}(\theta)} \quad (2.4)$$

$$A'_{1713} = I_{1713}\epsilon_{1713} + I_{701}b_{1012}\epsilon_{701}\epsilon_{1012}\overline{W_{701,1012}(\theta)} \quad (2.5)$$

$$\begin{aligned} A'_{3041} = & I_{3041}\epsilon_{3041} &+ \\ & I_{701}\epsilon_{701}b_{2340}\epsilon_{2340}\overline{W_{701,2340}(\theta)} &+ \\ & I_{1713}b_{1328}\epsilon_{1713}\epsilon_{1328}\overline{W_{1713,1328}(\theta)} &+ \\ & I_{701}b_{1012}b_{1328}\epsilon_{701}\epsilon_{1012}\epsilon_{1328}\overline{W_{701,1012,1328}(\theta)} \end{aligned} \quad (2.6)$$

The product of the efficiency terms means that in the CAESAR array, double sum-coincidence events will be a factor of  $\sim 100$  less intense than the real transitions producing them. For triple sum-coincidences this effect compounds again, making them  $\sim 100$  times weaker than the double-sum component. Using the branching ratios reported by Black et al [Bla75] and the measured efficiency of the CAESAR array in the far geometry (see Section 2.1.3), the proportion of 3041-keV peak due to sum-coincidences can be estimated to be 56% of the total intensity for this transition, with 1% of this owing to triple sum coincidence events. This calculation used theoretically calculated E4/E2, E4/M1 and M5/M1 angular correlations evaluated at  $0^\circ$  with values of 1.202, 0.956 and 0.946, respectively. For the 1713-keV and 2340-keV transitions, sum-coincidence events are expected to account for 21% and 2% of the total peak intensity, respectively. Consequently, it will be more difficult to detect changes in the intensity due to a decrease in sum-coincidences for these transitions compared to the 3041-keV transition.

If the efficiency of the detectors is decreased by pulling them back from the target, the sum-coincidence probability will decrease in a different ratio compared to the intensity of real peaks. For real events, a  $\Delta\epsilon_i$  change would be expected in the observed intensity, where  $\Delta\epsilon_i$  is the ratio of the efficiencies between the two configurations. For double-sum events, the efficiency product term in Equation 2.2 means a change of  $\Delta\epsilon_i\Delta\epsilon_j$  in the sum intensity will be observed. Similarly, for triple-sum events, a change of  $\Delta\epsilon_i\Delta\epsilon_j\Delta\epsilon_k$  will be observed.

In this work, detectors were moved by a distance of approximately 3.5 cm with the goal of achieving close to a  $\sqrt{2}$  reduction in the solid angle coverage of the three moveable detectors and therefore an approximately  $\sqrt{2}$  reduction in the efficiency. Since the efficiency of the detectors when pulled back was determined using a normalisation to the close-packed geometry efficiency curve, the  $\Delta\epsilon_i$  terms will all be equal to the normalisation factor. The average of the normalisation factors for the three moveable detectors was  $\Delta\epsilon = 1.40(4)$ . For this reason,  $\Delta\epsilon_i\Delta\epsilon_j$  and  $\Delta\epsilon_i\Delta\epsilon_j\Delta\epsilon_k$  can be reduced to constants,  $\Delta\epsilon^2$  and  $\Delta\epsilon^3$ . This means that for real, double-sum and triple-sum events, the intensity will change by factors of 1.40(4), 1.96(9) and 2.74(17) for each kind of event, respectively. This provides a means for assessing the character of a peak. Real  $\gamma$  rays should be unchanged in their absolute intensity between each geometry after accounting for the 1.40(4) change in the absolute efficiency. The change due to double-sum events should show a larger factor of 1.96(9) reduction in the intensity and, the intensity of triple-sum events will be reduced even further by a factor of 2.74(17). By comparing the ratios of transition intensities between the two geometries, the proportion of a peak owing to sum-coincidences can be examined. If the 3041-keV transition is real, the ratio of transition intensity between the two geometries should be between 1.40(4) and 1.96(9), depending on the relative proportion of real and sum-coincidence events. Given that the triple-sum component to this peak will be approximately two orders of magnitude smaller than the double-sum component, it is not expected to contribute significantly to this ratio.

At a late date it was discovered that the absolute detection efficiencies for the detectors in CAESAR were incorrectly determined and the values reported in

Figure 2.3 and used in later analysis are all too high. Correspondingly the results of the TM presented in Section 3.2.2 are all incorrect by a factor related to this error in the absolute efficiency. Hence, they are in disagreement with the results obtained using the other methods presented below. Note, however that the other methods have produced results that are correct and are in agreement with each other, since they rely solely on the (properly determined) relative efficiencies for the detectors.

### 2.2.2 Measuring sum-coincidence intensity from the 2029-keV transition – Sum-coincidence method (SM)

Considering Equation 2.2 presented above, the number of sum-coincidence events depends on three quantities: the intensities of the transitions which produce the sum peak, the efficiency of the detector at the energies of the transitions producing the sum peak and the angular correlation at  $0^\circ$  of the cascade producing the sum peak. Each of these properties is known, and, with the number of counts in the 2029-keV ( $701 + 1328$ ) sum-coincidence peak (that can only occur by summing), these properties can be scaled to estimate the sum-coincidence components of the other possible  $^{53m}\text{Fe}$  sum-peaks, using

$$A_{E_i+E_j} = A_{2029} \frac{I_{E_i} I_{E_j}}{I_{701} I_{1328}} \frac{\epsilon_{E_i} \epsilon_{E_j}}{\epsilon_{701} \epsilon_{1328}} \frac{\overline{W_{E_i, E_j}(\theta)}}{\overline{W_{701, 1328}(\theta)}}, \quad (2.7)$$

for double sum-coincidences and,

$$A_{E_i+E_j+E_k} = A_{2029} \frac{I_{E_i} I_{E_j} I_{E_k}}{I_{701} I_{1328}} \frac{\epsilon_{E_i} \epsilon_{E_j} \epsilon_{E_k}}{\epsilon_{701} \epsilon_{1328}} \frac{\overline{W_{E_i, E_j, E_k}(\theta)}}{\overline{W_{701, 1328}(\theta)}}, \quad (2.8)$$

for triple sum-coincidence events. For example, the number of sum-coincidence events due to the 701-2340-keV cascade would be

$$A_{701+2340} = A_{2029} \frac{I_{2340}}{I_{1328}} \frac{\epsilon_{2340}}{\epsilon_{1328}} \frac{\overline{W_{701, 2340}(\theta)}}{\overline{W_{701, 1328}(\theta)}}. \quad (2.9)$$

In this equation, the intensity and efficiency terms for the 701-keV transition have

canceled out. Note also that the other efficiencies appear as a relative efficiency ratio, so any overall error in the absolute efficiency normalisation has no effect on the method.

### 2.2.3 Measuring sum-coincidence intensity from the change in detector geometry – Geometric method (GM)

The number of sum-coincidence events can be measured directly using the change in sum-coincidence intensity between measurement geometries. As discussed earlier, when the detectors are moved backwards, the sum-coincidence intensity will decrease by a much larger factor than the real peak intensity. Using this fact, a method for obtaining the respective real and sum peak intensities of each  $^{53m}\text{Fe}$  transition has been developed. If the number of counts observed in each peak in each geometry is normalised using the ratio of the 701-keV transition intensities<sup>2</sup>, it can be assumed that the real component of the intensity for each transition is now a factor of  $\Delta\epsilon$  different. It follows from this that the sum-component, neglecting the small contribution from triple sums, is now a factor of  $\Delta\epsilon^2$ . The following equations:

$$R_c + S_c = I_c, \quad (2.10)$$

and,

$$R_f + S_f = I_f, \quad (2.11)$$

represent the total peak area in a spectrum, with  $R_{c,f}$  denoting the real peak components in the close (c) and far (f) geometries and  $S_{c,f}$  denoting the sum-component of the peak in the close and far geometries, while  $I_{c,f}$  denotes the total measured peak area. These equations can be reduced to:

---

<sup>2</sup>The 701-keV peak in each geometry will have lost some events to sum-coincidences, however the effect of this on the normalisation factor is negligible due to the high intensity of the 701-keV transition.

$$R_c - \Delta\epsilon^2 R_f = I_c - \Delta\epsilon^2 I_f, \quad (2.12)$$

by multiplying Equation 2.11 by  $\Delta\epsilon^2$  and subtracting it from Equation 2.10, since multiplying Equation 2.11 by  $\Delta\epsilon^2$  allows cancellation of the sum contribution as  $S_c = \Delta\epsilon^2 S_f$ . The substitution  $R_c = \Delta\epsilon R_f$  allows the equation to be expressed purely in terms of the known experimental quantities  $I_c$  and  $I_f$ , as well as the real peak area in the far geometry,  $R_f$ , reducing Equation 2.12 to

$$\Delta\epsilon R_f - \Delta\epsilon^2 R_f = I_c - \Delta\epsilon^2 I_f. \quad (2.13)$$

After solving this for  $R_f$ ,

$$R_f = \frac{I_c - \Delta\epsilon^2 I_f}{\Delta\epsilon - \Delta\epsilon^2}, \quad (2.14)$$

the values  $R_c$ ,  $S_c$  and  $S_f$  can also be deduced.

For the methods discussed in Sections 2.2.2 and 2.2.3, uncertainties have been evaluated using a Monte Carlo methodology. Input parameters were shifted by randomly sampling Gaussian distributions centered on the measured values with widths defined by their uncertainties. This resulted in distributions of real and sum-coincidence intensities from which the mean and standard deviation were taken as the final results.

## 2.3 Monte Carlo simulations of $^{53m}\text{Fe}$ decay

Monte Carlo simulations have been employed to replicate the decay of  $^{53m}\text{Fe}$  and evaluate the expected contribution from summing that would arise using the CAESAR array. These simulations were written in Mathematica 11.0 and have since been extended to be compatible with any nucleus and any detector system for both singles and coincidence data. The simulation takes as input (in a .csv format): the level scheme of the nucleus with the columns being the state energy

$E_i$ , branching ratios out of the state  $E_i$ , the final states  $E_f$ , the transition energies  $E_\gamma$  and the lifetime of the state  $E_i$ ,  $\tau$  (meanlife in seconds)<sup>3</sup>. The additional pieces of information included are the detector positions in spherical polar coordinates, the fitted parameters for each detector to generate an efficiency curve<sup>4</sup> and the angular correlation as a function of the angular separation between each detector pair for the detected  $\gamma$ -ray cascade. Discussion of the simulation here will be restricted to CAESAR and  $^{53m}\text{Fe}$ .

The simulation initialises with one nucleus in the  $J\pi = 19/2^-$  state. Through a random choice weighted by the state branching ratios, a decay path is selected. The simulation then moves to the new state based on the selection of the branch and repeats until reaching the ground state, where it proceeds to check if any of the  $\gamma$  rays were detected. To determine  $\gamma$ -ray detection, the simulation models the CAESAR array as a system of nine individual detectors represented by their individual absolute efficiencies. To detect a  $\gamma$ -ray transition, the simulation evaluates the efficiency at the given  $\gamma$ -ray energy and, through a random choice weighted by the efficiency of each detector, a detector to record the event is selected. A dummy detector with efficiency of one minus the total efficiency is included to reflect the non-detection probability. At this stage, the detection probabilities (i.e., the efficiencies) are scaled by the angular correlation between the two  $\gamma$  rays evaluated as a function of the angular separation between the detector which observed the first event and the other detectors. A sum-event is recorded when two or more decays in cascade are recorded in the same detector. Modeling of lifetimes for the purpose of sum-events is not required for  $^{53m}\text{Fe}$ , however, in level schemes where long intermediate lifetimes between transitions are present, sum events involving  $\gamma$ -cascades with long lifetimes ( $\geq 10$  ns for HPGe detectors) are vetoed and two distinct  $\gamma$ -ray detections are recorded. The simulation sequentially decays through states in one nucleus at a time, therefore sum events that might occur from  $\gamma$  rays emitted by two different nuclei at the same time are not modeled. This is not likely to occur at any meaningful level as count rates in the experiment were not high

<sup>3</sup>For instance, the  $J\pi = 19/2^-$  state in  $^{53m}\text{Fe}$  would be entered as (3041, {0.006, 0.013, 0.0981}, {0, 1328, 2340}, {3041, 1713, 701}, 220).

<sup>4</sup>Using the RADWARE method mentioned earlier in section 2.1.3

enough. Sum-coincidence events and real events are stored separately and on a detector-by-detector basis, making them easy to distinguish when analysing the Monte Carlo data. The results of these simulations are presented in Chapter 4.

# 3

## Chapter 3

## Analysis and results

---

This chapter will present the results of the experiments performed and confirmation of the 3041-keV E6 branch from the  $J^\pi = 19/2^-$  state in  $^{53m}\text{Fe}$ . The level scheme of  $^{53m}\text{Fe}$  from the present work is shown in Figure 3.1.

Exact replication of the work of Black et al [Bla75] in 1975 is impossible at the Heavy Ion Accelerator Facility due to several aspects of their experimental method. They produced clean samples of  $^{53m}\text{Fe}$  in their work via the  $^{55}\text{Mn}(\text{p},3\text{n})^{53m}\text{Fe}$  reaction with subsequent chemical separation to remove unwanted contaminants. Pneumatic rabbit systems moved the relatively short-lived targets to a counting area, enabling targets to be produced with a high activity that would be reduced by the time the source reached the counting area without risking harm to detectors or people. The result of this effort was a relatively clean  $\gamma$ -ray spectrum with a high number of counts in the 3041-keV peak. A spectrum obtained in their work is shown in Figure 3.2 [Bla75]. The ANU 14UD facility no longer features a pneumatic rabbit system, therefore all measurements took place on the beam-line under vacuum, which also rendered chemical separation impossible<sup>1</sup>. In our work, DC beams and

---

<sup>1</sup>In any case, the HIAF facility is not equipped to perform chemistry using hot radioactive materials.

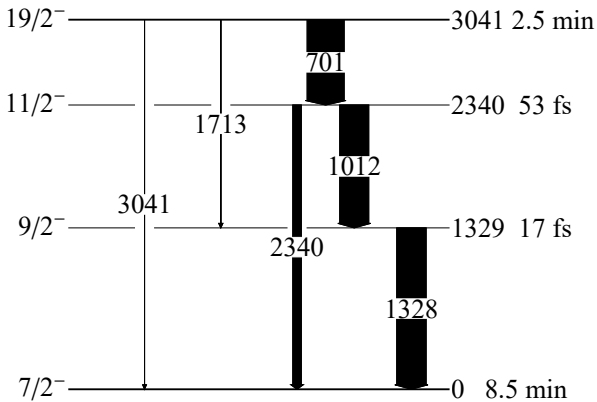


**Figure 3.1:** Level scheme for  $^{53m}\text{Fe}$  as obtained in this work. Transition widths are reflective of the real transition intensities obtained in Section 3.2.3. State half-lives are as given in ref. [Jun09].

subtraction of long-lived activity reaction products over long collection cycles were used to produce high count rates in a clean spectrum, however, the cost of this was a high degree of neutron damage to the HPGe detectors, many of which required subsequent annealing to repair the damage.

### 3.1 Experiment summaries

Four experiments took place during 2016 to measure the intensity of the 3041-keV E6 branch in  $^{53m}\text{Fe}$ . Two experiments used the  $^{51}\text{Va}(^6\text{Li}, 4n)^{53}\text{Fe}$  reaction; the first tested the viability of this reaction for  $^{53m}\text{Fe}$  production, while the second attempted to measure the E6 branching ratio. Following the collection of sufficient statistics for measuring the E6 branching ratio, the  $^{24}\text{Mg}(^{32}\text{S}, 2pn)^{53}\text{Fe}$  reaction was used for the third experiment. The data obtained in this experiment contained significant issues which the following section will describe. A fourth experiment was later carried out using the same sulfur-magnesium reaction to investigate the issues found in the analysis of the prior experiment's data. Initial discussion and analysis will be limited to the first two experiments with the lithium-vanadium

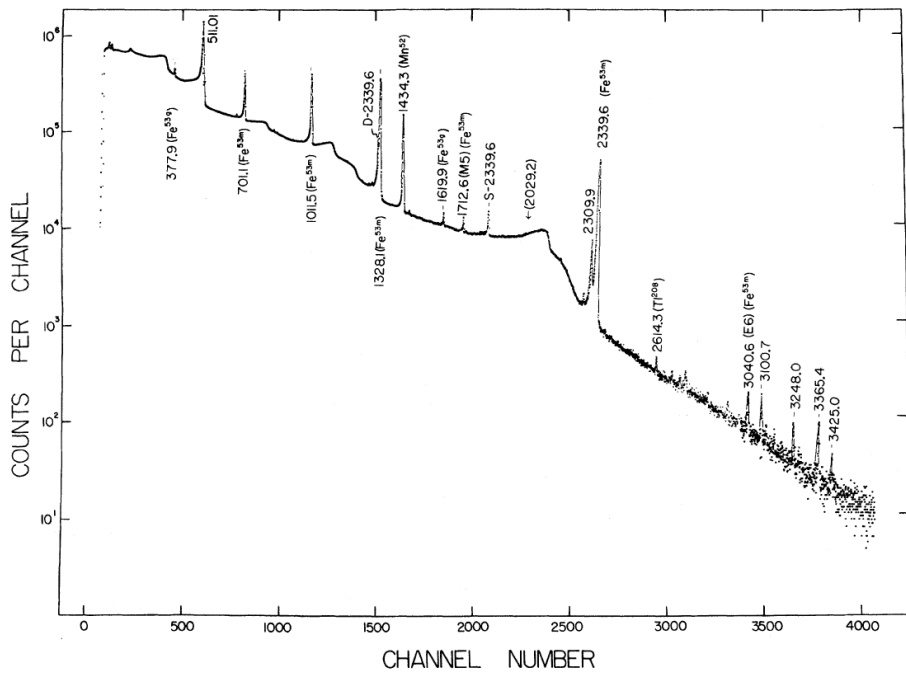


**Figure 3.2:**  $\gamma$ -ray spectrum of  $^{53}\text{m}\text{Fe}$  decay obtained by Black et al [Bla75].

reaction, with a subsequent discussion of the intensity balance issues present in the third experiment. A method was derived for correcting the data from this third experiment to arrive at a consistent set of results, but nevertheless this third data set is not used in the final evaluation. For this reason, the sulfur-magnesium results should be considered secondary to the values obtained using the lithium-vanadium data which, it will be shown, are capable, without correction, of verifying the existence of the E6 transition.

### 3.1.1 March experiment

The March experiment was a proof-of-concept undertaking to test the viability of the  $^{51}\text{Va}(^6\text{Li}, 4\text{n})^{53}\text{Fe}$  reaction to cleanly populate the  $J^\pi = 19/2^-$  isomer in  $^{53}\text{Fe}$ . Vanadium is to first order mono-isotopic, with 99.750% of all natural vanadium consisting of  $^{51}\text{V}$ , meaning an enriched foil was not required and multiple targets could be easily prepared. Statistical model calculations [Gav80] shown in Figure 3.3 predicted a moderate yield of  $^{53}\text{Fe}$  relative to other reaction products, however only a small number of these products have lifetimes similar to that of  $^{53}\text{m}\text{Fe}$ . The

majority of the fusion evaporation and  $\beta$ -decay products were either stable or had lifetimes on the order of years (see Table 3.1). This meant that the time stamps from the J624 could be used to subtract the long-lived activity from a significant percentage of the fusion evaporation products and, hence, isolate predominantly the  $^{53m}\text{Fe}$  decay. Thus, it was hoped that with high beam currents and suitable background subtraction, the low yield of  $^{53m}\text{Fe}$  relative to the neighboring reaction products could be mitigated and a clean, out-of-beam measurement of the E6 branch could be achieved. Results from this first experiment showed a high yield of the strong  $\gamma$  rays in  $^{53}\text{Fe}$  and a clean subtraction was possible, however, no counts in the 3041-keV E6 peak were detected due to the short, hour long, duration of the experiment.

### 3.1.2 May experiments

The May experiments began with two measurements using the  $^{51}\text{Va}(^6\text{Li}, 4n)^{53}\text{Fe}$  reaction at a beam energy of 50 MeV. After a sufficient number of 3041-keV events were detected, three of the HPGe detectors were moved back by several centimeters (see Table 2.1) to produce an approximately  $\sqrt{2}$  decrease in the efficiency (estimated using the expected change in solid angle covered and subsequently confirmed to be a decrease of 1.40(4) in the measured efficiency for the three moveable detectors). Four  $^{51}\text{V}$  foil targets, 9.6-mg/cm<sup>2</sup> thick, were used in each of the lithium-vanadium experiments with targets being cycled periodically to mitigate activity buildup. The reaction was changed to  $^{24}\text{Mg}(^{32}\text{S}, 2pn)^{53}\text{Fe}$  at 90 MeV, using a natural (79%)  $^{24}\text{Mg}$  3.3 mg/cm<sup>2</sup> target, towards the end of the experiment after sufficient statistics had been gathered and it was clear that it would be impossible to dramatically improve the uncertainty without investing considerable extra beam time. The sulfur-magnesium reaction had a significantly higher yield of  $^{53}\text{Fe}$  and as a result, more than double the number of counts were detected in the 3041-keV peak after approximately 18 hours counting in each geometry, compared to the two days used for each geometry with the lithium-vanadium reaction. Towards the end of the experiment, however, a large hole was melted through the target causing radioactive nuclei to be deposited downstream of CAESAR.

**Table 3.1:** Products of the  ${}^6\text{Li}({}^{51}\text{Va}, 4\text{n}){}^{53}\text{Fe}$  and  ${}^{32}\text{S}({}^{24}\text{Mg}, 2\text{pn}){}^{53}\text{Fe}$  reactions sorted by shortest lifetime to longest. The majority of the reaction products have ground state lifetimes longer than the duration of this experiment and will thus be subtracted using the time subtraction method discussed in Section 2.1.1. Due to the 2 second delay between taking the beam off target and starting data acquisition, reaction products with half-lives less than one second will have largely decayed away before data acquisition begins. Half-lives taken from Nuclear Data Sheets A = 44 - 55 [Bur06, Xia06, Bur07, Bur08, Jun08, Jun09, Che11, Ele11, Don15].

${}^6\text{Li} + {}^{51}\text{Va}$		${}^{32}\text{S} + {}^{24}\text{Mg}$	
Product	Lifetime	Product	Lifetime
${}^{53}\text{Fe}$	<b>8.5 m</b>	${}^{53}\text{Fe}$	<b>8.5 m</b>
${}^{51}\text{Ti}$	5.1 m	${}^{54}\text{Co}$	193.3 ms
${}^{49}\text{Cr}$	42.3 m	${}^{50}\text{Mn}$	283.2 ms
${}^{48}\text{Sc}$	43.7 h	${}^{47}\text{V}$	32.6 m
${}^{47}\text{Sc}$	3.3 d	${}^{51}\text{Mn}$	46.2 m
${}^{52}\text{Mn}$	5.6 d	${}^{48}\text{Cr}$	21.56 h
${}^{51}\text{Cr}$	27.7 d	${}^{52}\text{Mn}$	5.6 d
${}^{54}\text{Mn}$	312 d	${}^{44}\text{Ti}$	59.1 y
${}^{49}\text{V}$	330 d	${}^{53}\text{Mn}$	$3.7 \times 10^6$ y
${}^{53}\text{Mn}$	$3.7 \times 10^6$ y	${}^{50}\text{Cr}$	$1.3 \times 10^{18}$ y
${}^{50}\text{V}$	$1.4 \times 10^{17}$ y	${}^{52}\text{Cr}$	Stable
${}^{50}\text{Cr}$	$1.3 \times 10^{18}$ y	${}^{54}\text{Fe}$	Stable
${}^{47}\text{Ti}$	Stable		
${}^{48}\text{Ti}$	Stable		
${}^{49}\text{Ti}$	Stable		
${}^{50}\text{Ti}$	Stable		
${}^{51}\text{V}$	Stable		
${}^{52}\text{Cr}$	Stable		
${}^{53}\text{Cr}$	Stable		
${}^{54}\text{Fe}$	Stable		
${}^{55}\text{Mn}$	Stable		

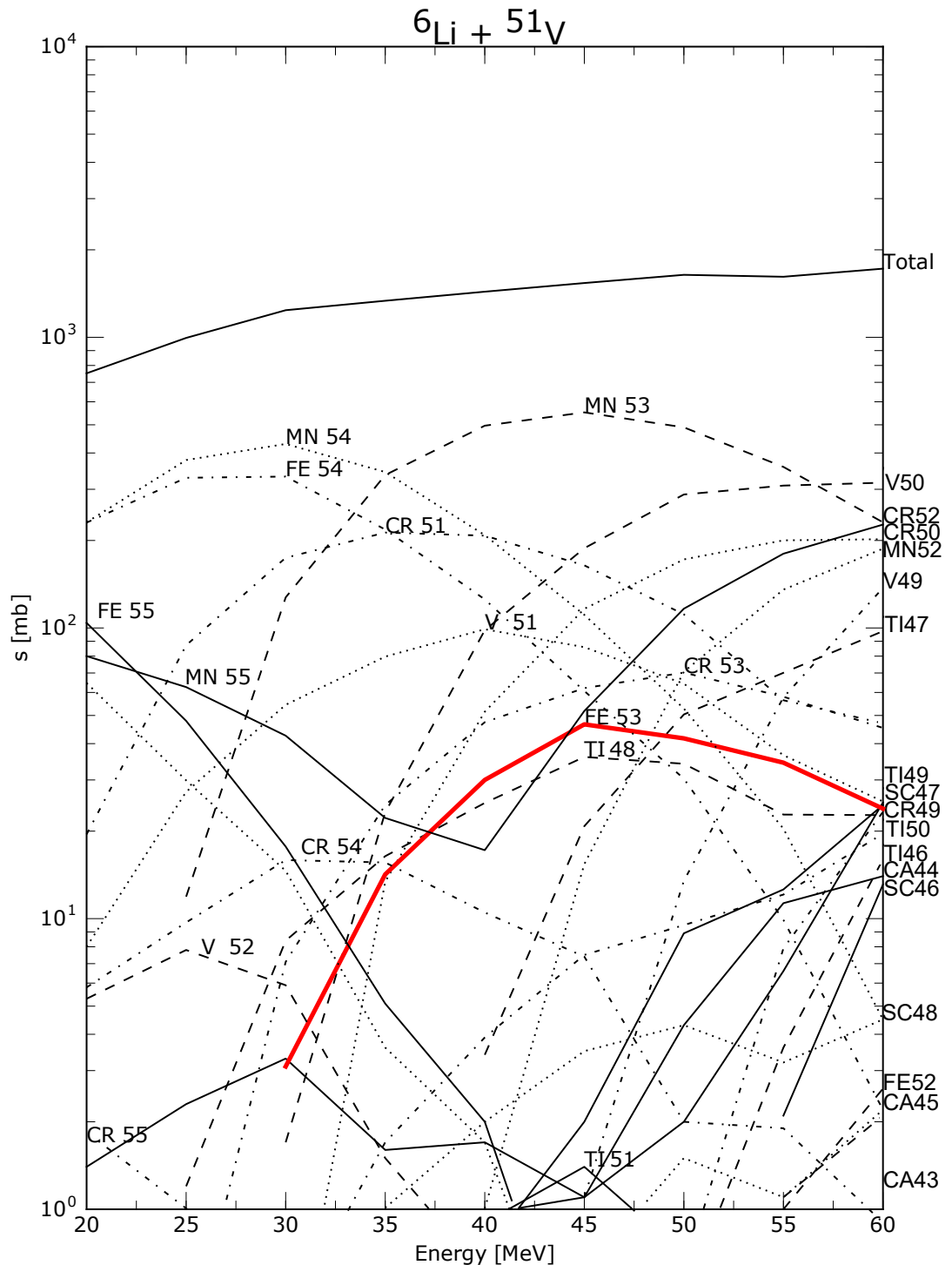


**Figure 3.3:** ZPACE statistical model calculations of the products of the  ${}^6\text{Li} + {}^{51}\text{V}$  reaction. Half-lives of reaction products are shown in Table 3.1. With the majority of the reaction products having long half-lives it was hoped that the low yield of  ${}^{53}\text{Fe}$  relative to the other decay products could be overcome through subtraction of long-lived activity.

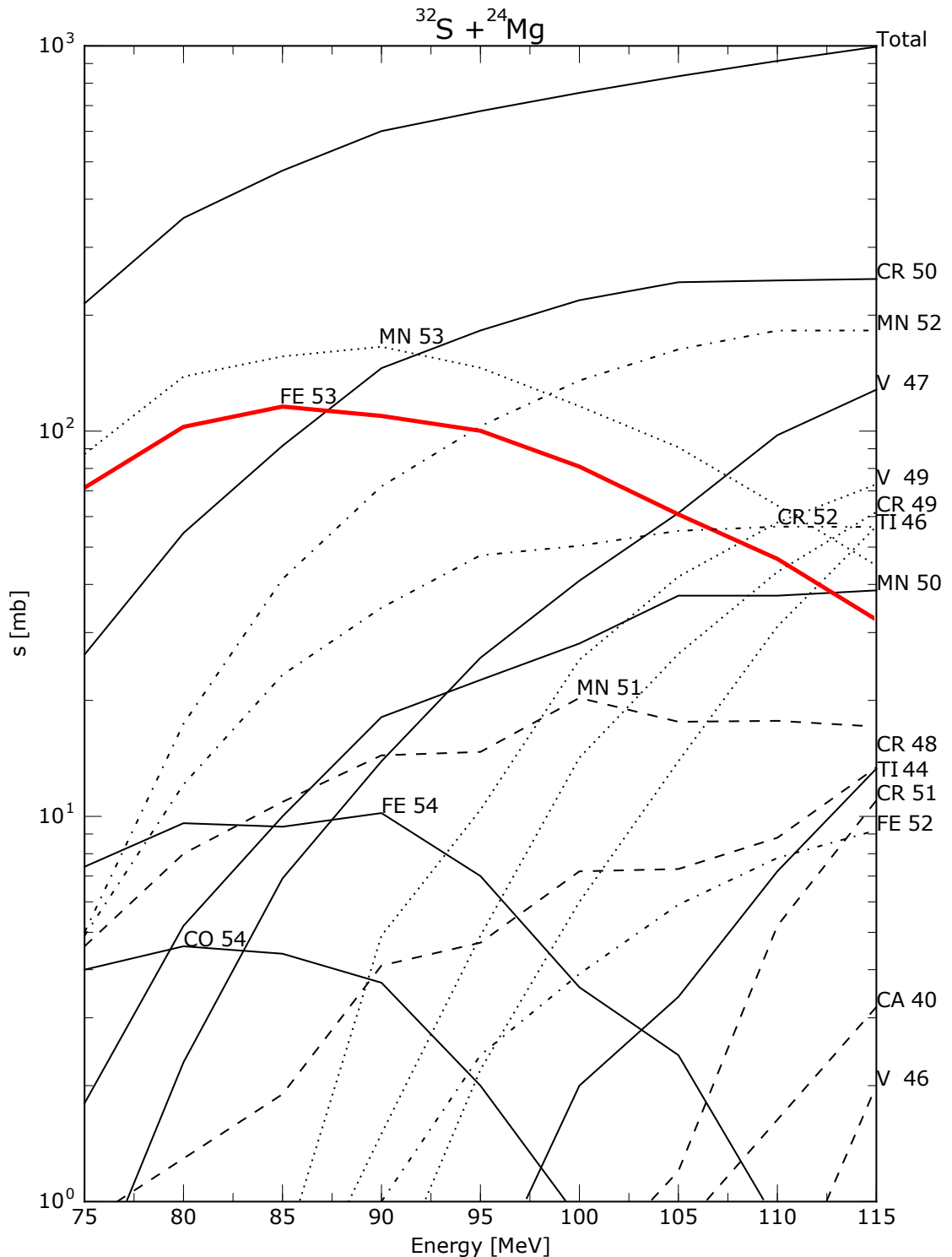


**Figure 3.4:** ZPACE statistical model calculations of the products of the  $^{32}\text{S} + ^{24}\text{Mg}$  reaction. Half-lives of reaction products are shown in Table 3.1. Similar to the  $^{51}\text{V} + ^6\text{Li}$  reaction, the majority of the reaction products are long lived, however, this reaction is predicted to produce a significantly higher yield of  $^{53m}\text{Fe}$ .

### 3.1.3 December experiment

A final experiment performed using the sulfur-magnesium reaction, and involving the collection of  $\gamma$ - $\gamma$  coincidences as well as a further singles data set, was carried out over three days in December of 2016. In this experiment, coincidence data were collected to investigate potential side-feeding of the states below the  $J^\pi = 19/2^-$  isomer. An additional singles data set was collected to investigate the substantially different transition intensities measured between the sulfur-magnesium and lithium-vanadium data sets in the May 2016 experiment. The three movable HPGe detectors had been replaced with six LaBr detectors due to the requirements of the CAESAR experiment that ran immediately prior; hence, changes in peak intensities due to different detector geometries were not a part of this experiment.

The coincidence experiment used TDCs for the measurement of relative  $\gamma$ -ray times between HPGe detectors and used different beam/J624 reset cycles (2.5 minutes beam-on with 2.5 minutes beam-off); long time subtraction was unnecessary as the coincidence requirement sufficiently cleaned up the spectra. In the singles experiment, the same beam/J624 reset cycle (7.5 minutes on with 20 minutes off) were used as in the May experiment, however, count rates were kept significantly lower to reduce neutron damage to the detectors. Magnesium targets of  $3.3 \text{ mg/cm}^2$ , similar to the previous experiment, were used, making beam-current readings through the target comparable between the two sulfur-magnesium experiments.

## 3.2 Experimental results

### 3.2.1 Initial results

Gamma-ray spectra obtained for the lithium-vanadium and sulfur-magnesium reactions in the May experiments are shown in Figure 3.5. Photopeak yields were determined using Gaussian functions with tail components when appropriate,

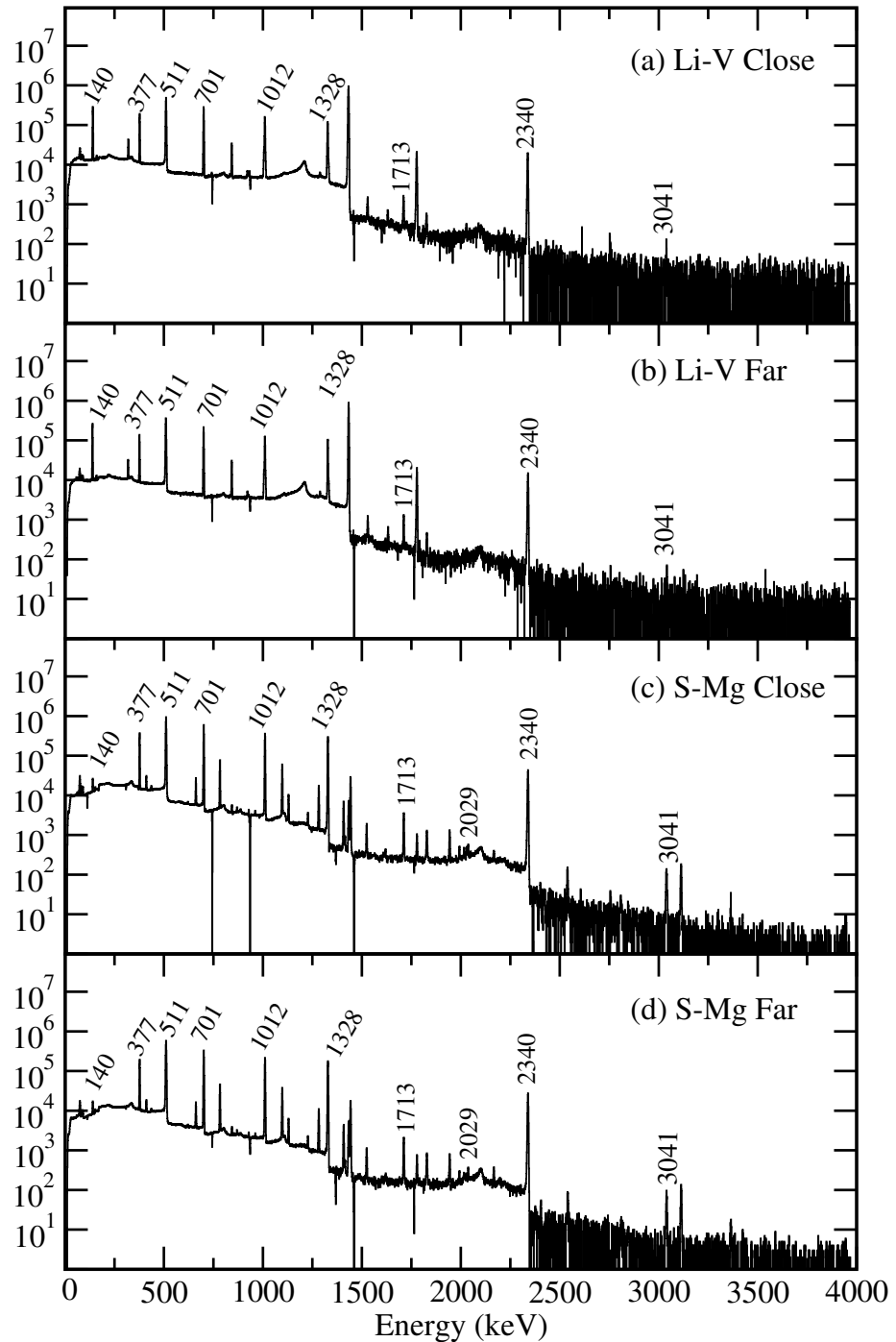


**Figure 3.5:** Activity subtracted  $\gamma$ -ray spectra obtained for the lithium-vanadium and sulfur-magnesium experiments. Large negative spikes are due in part to the the logarithmic scale and also because of increased acquisition dead time in the initial period of data collection when the count rates were high. Count rates were higher in the close geometry measurements and the sulfur-magnesium experiments.

Peak	Relative Intensity					
	Vanadium (May)		Sulfur (May)		Sulfur (Dec)	Literature
	Close	Far	Close	Far	Dets. 1-6	
701	1000(68)	1000(37)	1000(68)	1000(46)	1000(50)	1000
1012	790(55)	802(35)	871(73)	866(44)	789(40)	860(90)
1328	817(57)	836(36)	934(88)	931(52)	813(42)	870(80)
1713	12.0(9)	11.9(5)	14.2(14)	13.8(9)	11.5(11)	13.2(10)
2340	222(16)	233(12)	265(28)	275(22)	212(12)	129.8(20)
3041	1.21(11)	1.03(8)	1.26(10)	1.18(9)	1.04(19)	0.6(1)

**Table 3.2:** Intensity of  $\gamma$  rays emitted in the decay of the  $J^\pi = 19/2^-$  isomer in  $^{53}\text{Fe}$  normalised to an intensity of 1000 for the 701-keV peak. These intensities incorporate the sum-components of the 1713-, 2340- and 3041-keV peaks and are reported as measured in the three moveable detectors (7, 8 and 9) for the May experiments. The December experiment only used the stationary detectors 1 - 6, hence no measure of sum-coincidence intensity could be obtained. Literature values [Bla75] converted to the same intensity scale have been included for reference. The 2029-keV peak intensity is excluded from this table as these values are efficiency adjusted.

with the exception of the low-intensity 2029-keV pure sum-coincidence peak. This line has a low number of counts and can only occur as a sum-coincidence peak; hence it was fitted using a Gaussian function of fixed width defined by the widths of the 701- and 1328-keV transitions added in quadrature. The intensities of transitions for both reactions and both geometries are shown in Table 3.2. It should be noted that the intensities of the 1713-keV, 2340-keV and 3041-keV transitions include contributions from the sum-components. In order to discuss and compare experimental results and literature values, intensities are shown with respect to the intensity of the 701-keV peak normalised to 1000 intensity units. Final branching ratios and transition intensities relative to the total decay through the  $J^\pi = 19/2^-$  isomer will be later presented following the subtraction of the sum components from the  $^{53m}\text{Fe}$  decay peaks. Discussion here will be limited to the lithium-vanadium experiments as the transition intensities measured for the sulfur-magnesium experiments have potential problems that will be discussed in Section 3.3.

The transition intensities obtained in this experiment differ significantly from those reported by Black et al. The 2340-keV transition is almost double the intensity in the data set for the lithium-vanadium experiments while the 1012- and 1328-

**Table 3.3:** Gamma ray branching ratios for the 2340-keV state from each of the measurements in this work and values from the literature [Bla75, Saw73, Rie05]. The  $\gamma$ - $\gamma$  coincidence measurement obtained these branching ratios by gating on the 701-keV transition.

Peak	Singles			$\gamma - \gamma$	Literature		
	Li-V		S-Mg	S-Mg	[Bla75]	[Rie05]	[Saw73]
	Close	Li-V	Dec.	Dec.			
1012	0.78(4)	0.77(4)	0.788(18)	0.757(21)	0.87(12)	0.83(4)	0.76
2340	0.219(14)	0.23(3)	0.212(17)	0.243(10)	13(2)	0.17(2)	0.24

keV transitions have decreased in intensity relative to the literature values. If the intensity of the 2340-keV branch was misreported by Black et al, a corresponding decrease in the intensity of the 1012- and 1328-keV transitions would occur, similar to the present observations. A summary of the 2340-keV state branching ratios obtained in the present experiments along with literature values from several publications are presented in Table 3.3. Each of the 2340-keV state branching ratios measured in the present work by and large agree with each other, and all show a large departure from Black et al's values. The large uncertainties of  $\pm 14\%$  on Black et al's numbers mean that within one sigma the branching ratios obtained in their work could agree with any of the measurements in Table 3.3. This suggests that our results constitute a refinement in the measurement of the 2340-keV state branching ratio. The values reported by Rietz et al [Rie05] fall in between the values obtained in our work and those reported by Black et al [Bla75], while Sawa's [Saw73] results also show a large difference to Black et al, however, no uncertainty was reported. A weighted average of the present and literature results, other than those of Sawa, give values of 0.79(3) and 0.21(1) for the branching ratios of the 1012- and 2340-keV transitions, respectively. The results of Sawa were not included in the weighted average as no uncertainty was reported. Figure 3.6 shows a compilation of these results with the weighted average drawn through the graph.

### 3.2.2 Measuring sum-coincidence intensities

As discussed in Section 2.2, the expected change in the number of counts due to the movement of a HPGe detector, will depend on the change in efficiency  $\Delta\epsilon$  ( $\Delta\epsilon$  is the change in efficiency, defined as a ratio, in Section 2.2), and will be  $\Delta\epsilon$  for a

**Figure 3.6:** Summary of literature values from Refs. [Bla75, Rie05] and experimental measurements obtained in this work for the 2340-keV state branching ratio. The blue shaded region indicates the weighted average of all of the measurements with reported uncertainties (Ref. [Saw73] gave no uncertainty and hence has been excluded from this plot).

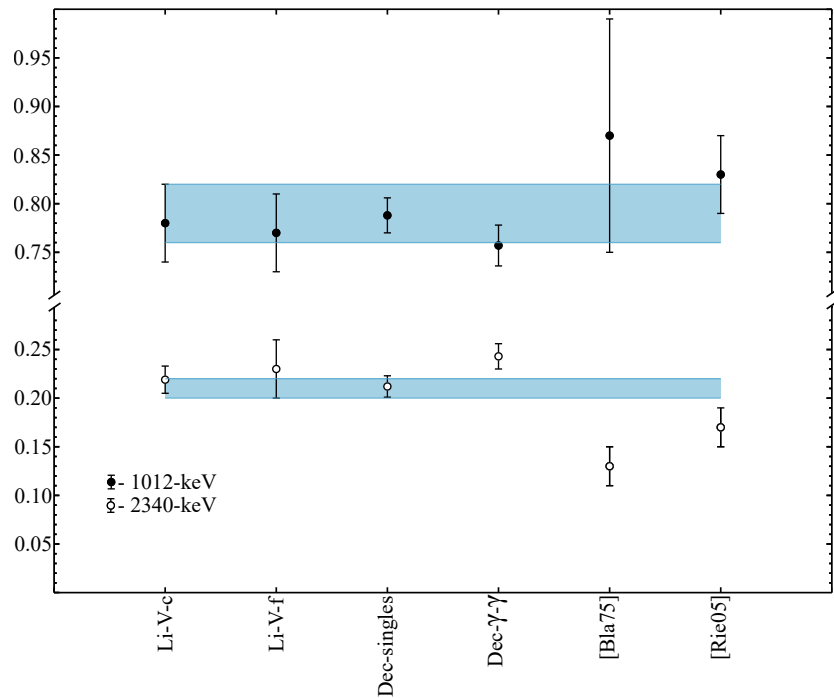


**Table 3.4:** Ratios of transition intensity between detector geometry. Ratios of 1.40(4), 1.96(9) and 2.74(17) correspond to real, double-sum, and triple sum-transitions, respectively.

Peak	Experimental Ratio	Expected Ratio	Character
701	1.37(8)	1.40(4)	Real
1328	1.37(8)	1.40(4)	Real
1713	1.35(17)	> 1.40(4)	Real+Possible sum
2029	1.9(4)	1.96(9)	Sum
2340	1.33(9)	> 1.40(4)	Real+Possible sum
3041	1.65(18)	> 1.40(4)	Real+sum

real peak,  $\Delta\epsilon^2$  for a sum-coincidence peak and  $\Delta\epsilon^3$  for a triple-sum-coincidence peak. This provides a means of assessing the character of a peak in the  $\gamma$ -ray spectrum as its change in intensity between close and far geometries will indicate whether it is real, real with a sum component, or purely a sum peak. In the present experiment the efficiency change for the sum of the moveable Detectors 7, 8 and 9 is  $\Delta\epsilon = 1.40(4)$ . Therefore, a change of 1.40(4), 1.96(9) and 2.74(17) is expected for real, double-sum and triple-sum events. Table 3.4 shows the observed change in transition intensities for each transition in  $^{53m}\text{Fe}$ .

The ratios in Table 3.4 for the lithium-vanadium data are in line with the expected change for the 701-, 1012- and 1328-keV real transitions. The 2029-keV sum peak of the 701- and 1328-keV transitions exhibits a change of 1.9(4) which is in agreement with the 1.96(9) change expected for a pure double-sum transition. Given the high intensity of the 701-, 1012- and 1328-keV transitions, it is expected that sum contributions similar in size to the 2029-keV peak will be present in the 1713-keV peak ( $1012 + 701$ ) and the 2340-keV peak ( $1012 + 1328$ ) as these can also be produced by the summation of high-intensity lines. Using the Sum-coincidence Method (SM) shown in Section 2.2, the number of sum-coincidence counts in the 1713-keV, 2340-keV and 3041-keV transitions can be calculated by scaling the number of counts in the 2029-keV sum-peak. These results are shown in Table 3.5 along with the number of sum-coincidence counts expected using the Geometric Method (GM) for evaluating the sum-coincidence intensities; the results obtained using the Theoretical Method are shown in Table 3.6. The number of sum-coincidence counts in the 1713-keV and 2340-keV peaks relative to the 2029-keV sum-coincidence counts are as expected owing to the relative efficiencies of the constituent transitions.

**Table 3.5:** Experimentally measured peak area for each of the peaks with a sum-coincidence component as well as the number of sum-coincidence events evaluated according to the SM and GM (see Section 2.2).

Peak	Close			Far		
	Expt.	SM	GM	Expt.	SM	GM
1713	6059(140)	708(91)	396(1118)	4243(89)	372(59)	233(595)
2029	589(65)	589(65)	589(65)	310(49)	310(49)	310(49)
2340	87489(329)	729(94)	-18136(12505)	66080(228)	382(61)	-8859(5972)
3041	387(22)	201(26)	209(128)	234(16)	95(16)	109(70)

**Table 3.6:** Number of counts predicted using the TM and scaled TM (see text for description) in each peak with a sum-coincidence component as well as the sum-coincidence counts determined using the SM method (see Section 2.2).

Peak	Close			Far		
	SM	TM	TM (scaled)	SM	TM	TM (scaled)
1713	708(91)	1421(38)	714(41)	372(59)	723(14)	363(20)
2029	589(65)	1226(32)	616(35)	310(49)	634(13)	319(17)
2340	729(94)	1515(40)	761(43)	382(61)	783(16)	393(21)
3041	201(26)	365(9)	184(10)	95(19)	192(4)	97(5)

For example, detector efficiency is higher for the 701-keV and 1012-keV transitions and therefore it is expected that the number of 1713-keV sum-coincidence events would be higher than those for the number of events in the 2029-keV peak.

The sum-coincidence intensities estimated using the number of counts in the 2029-keV pure sum peak indicate that the experimental setup would not have been sensitive to the change in 2340-keV peak intensity resulting from moving the detectors backwards. The peak areas measured were  $87489 \pm 329$  for the close geometry and  $66080 \pm 228$  for the far geometry, with the sum-coincidence intensity being estimated as 729(94) and 382(61) for the close and far geometries, respectively. The resulting difference of 347(112) would have been unresolvable in this experiment. Similarly, the 1713-keV transition has  $6059 \pm 140$  counts in the close geometry and  $4243 \pm 89$  counts in the far geometry, while the expected difference in sum-coincidence counts according to the SM would be 336(108). In principle, this difference should be resolvable, however, the difference is still small compared to the combined uncertainty of 166 counts in the difference between the two experimental peak areas. The changes predicted by the SM correspond to

---

a decrease of 0.5% and 2.5% in the total peak area of the 2340-keV and 1713-keV transitions, respectively. Consequently, the Geometric-Method for estimating sum-coincidences (Section 2.2) will have difficulty measuring an accurate difference in the intensity, since these changes are small compared to the statistical uncertainty. For the 3041-keV peak the expected change in peak intensity according to SM is 106(32) counts, corresponding to a percentage change in total peak area of 9%, this should be resolvable given the 3041-keV peak areas and uncertainties for each geometry.

The results of using the Geometric-Method (GM) are also shown in Table 3.5. For the 3041-keV and 1713-keV transitions, good agreement with the SM occurs (within  $0.3\sigma$ ) while for the 2340-keV transition the agreement is within  $0.8\sigma$ . The negative sum-peak counts that occur for the 2340-keV peak are due to the slight increase in the intensity measured in the far geometry compared to the close geometry, although within errors these two intensities are the same. It was expected that the small sum-component relative to the large real, intensity for the 2340-keV peak would mean that the sum-component for this peak would not be easily measurable; these results confirm this. Of the 234(16), counts in the 3041-keV peak in the far geometry, 109(70) counts are sum-coincidence events. This corresponds to 47(25)% of the peak area being due to sum-coincidences. Similarly, for the close geometry, 209(128) of the counts in the 3041-keV peak are sum-coincidence events giving rise to a peak which is 54(33)% sum-coincidence events.

The large uncertainties present in the GM results are a consequence of the volatility of this method. Shifting the experimental values of either  $I_c$  or  $I_f$  (see Equation 2.14) by one sigma produced drastically different real and sum peak components. When Monte Carlo methodology is used to evaluate the sum-peak component uncertainties, the resultant Gaussian distributions for  $R_{c,f}$  and  $S_{c,f}$  have a very large width. The total uncertainty is compounded by the large number of terms in this method with uncertainties that must be varied. In particular,  $\Delta\epsilon$  and the normalisation parameter used to account for the relative collection times of each data set, all have a normally distributed uncertainty that must be incorporated into the Monte Carlo algorithm.

The Theoretical Method (results shown in Table 3.6) suggests large sum-coincidence components to each of the potential real/sum-peaks, in particular the 3041-keV peak is predicted to owe 94(6)% and 82(6)% of its total peak area to sum-coincidences for the close and far geometries, respectively. That this percentage changes does suggest the peak has a real component, though significantly weaker than proposed by Black et al [Bla75], who cited the absence of a 2029-keV sum-peak as evidence that sum-coincidences were not a large component of the observed peak. Black et al's assertion is correct, as the number of sum coincidence events decreases with the efficiency squared, so a sufficiently low efficiency detector will have little to no sum-coincidences. This is true for the stationary detectors in the CAESAR array, where no 2029-keV peak could be found in any of their individual spectra, while a 3041-keV peak was still clearly visible.

More noteworthy than the predicted 3041-keV sum-coincidence intensity is the predicted numbers of 2029-keV sum-coincidence events, that fail to be reproduced for either geometry. This calls into question whether the sum-coincidence components predicted for any of the other peaks using the TM are valid, as this method should be able to be easily tested using the 2029-keV sum peaks visible in the  $\gamma$ -ray spectra. The predicted 2029-keV intensities using the TM are 1.97(14) and 2.02(15) times the intensity of the measured 2029-keV sum-peak area. If the intensity predicted by the TM is decreased by a factor<sup>2</sup> of 1.99(10) (columns labeled "scaled" in Table 3.6), the results all agree with the SM. The results of applying the scaling factors to the theoretically predicted sum-coincidence events are also shown in Table 3.6. Performing this scaling lowers the 3041-keV predicted sum-coincidence components to 48(4)% and 41(4)% of the total peak area for the close and far geometries, respectively.

The fact that this scaling is necessary to reproduce the experimental 2029-keV peak area is a consequence of the incorrectly determined absolute efficiencies that were briefly mentioned in Section 2.2. This error will need to be further evaluated prior to publication in a refereed journal but does not affect the rest of the analysis with

---

<sup>2</sup>1.99(10) is the weighted average of the ratio between the 2029-keV counts predicted by the TM compared to the experimentally measured area for the two geometries.

the SM and GM methods.

### 3.2.3 Measuring $^{53m}\text{Fe}$ state branching ratios

Using the number of counts obtained through the SM and GM analyses discussed above, sum-coincidence components can be subtracted from the 1713-keV, 2340-keV and 3041-keV peak areas and the true  $^{53m}\text{Fe}$  state branching ratios and transition intensities can be deduced (see Table 3.7). The E6 branching ratio obtained for both geometries, with either method, agrees with the result obtained by Black et al [Bla75], albeit with much larger uncertainties for the geometric method results. The branching ratio for the 1713-keV transition has decreased for each method relative to Black et al with only the GM measurements agreeing at the one sigma limit. Unsurprisingly, the 2340-keV branching ratios continue to disagree with literature values (see Section 3.2.1 for an earlier discussion on this point). The values obtained using the GM have been skewed somewhat due to the negative sum-coincidence component suggested by this method, however, it also results in larger uncertainties, so that all four measurements and analysis methods produce a consistent set of branching ratios.

The weighted average of each measurement is included in Table 3.7. For the 2340-keV state, the average is in agreement with the previous average of each of the measurements from our work, and, the literature values (see Table 3.3 and Figure 3.6). The sum-coincidence component of the 2340-keV peak is small relative to the total areas of the 1012-keV and 2340-keV peaks; the small difference between the subtracted and un-subtracted 2340-keV state branching ratios obtained in the present work comes as little surprise.

## 3.3 Investigation of inconsistent transition intensities

An inconsistency in measured intensities between the lithium-vanadium and sulfur-magnesium experiments (shown in Table 3.2) has yielded two conflicting data sets. The large differences in transition intensity relative to the 701-keV transition for

**Table 3.7:** Measured  $\gamma$ -ray branching ratios for the 3041-keV and 2340-keV states in  $^{53m}\text{Fe}$  accounting for the subtraction of sum-coincidence events. These values have been obtained using the SM and GM (see Section 2.2). The GM results for the close and far geometry have been combined as both methods solve for the same real peak areas (when adjusting for efficiency), and thus, the same branching ratios when subtracting the sum-coincidence events. The weighted average is also shown.

		Branching Ratio			
State (keV)	Peak	SM Close	SM Far	GM	Average
3041	701	0.99(7)	0.99(5)	0.99(4)	0.99(3)
	1713	0.011(1)	0.0116(13)	0.0117(16)	0.0112(7)
	3041	0.00057(11)	0.00060(11)	0.0006(2)	0.00059(7)
2340	1012	0.78(5)	0.78(4)	0.75(6)	0.77(4)
	2340	0.219(14)	0.225(11)	0.25(3)	0.23(1)

the 1012-keV, 1328-keV and 2340-keV transitions, point towards severe problems with the first sulfur-magnesium data in may which the following sections will explore. Ultimately, the May lithium-vanadium experiments and the December sulfur-magnesium experiment present a consistent data set which has formed the basis for all of the results presented in the present work. If the intensity feeding and depopulating a state is examined, it is clear that the 1328-keV and 2340-keV states have greater  $\gamma$  intensity depopulating the states than intensity that feeds them, in the sulfur-magnesium data. Defining:

$$\Gamma_E = \frac{\sum_{d=1}^n I_d}{\sum_{f=1}^n I_f}, \quad (3.1)$$

where  $I_d$  is the total intensity ( $\gamma$  rays and internal conversion) of the transitions depopulating a state and  $I_f$  is the total intensity of the transitions feeding it, then  $\Gamma_E$  is the intensity balance at the state with energy  $E$ . This value should equal one, as the intensity feeding must equal the intensity depopulating. When applying this test to the 1328-keV and 2340-keV states, the resulting balances are  $\Gamma_{1328} = 1.06(2)$  and  $\Gamma_{2340} = 1.14(3)$  for the far geometry and  $\Gamma_{1328} = 1.04(2)$  and  $\Gamma_{2340} = 1.14(2)$  for the close geometry in the sulfur experiments. Table 3.8 shows these balances for each experiment. Note that the values balance ( $\Gamma_E=1$ ) in the lithium-vanadium experiments and in the December sulfur-magnesium experiment.

Side feeding into these states from prompt decay presents an unlikely possibility

to explain these results. Between the irradiation and measurement cycles a two-second delay is implemented to ensure the high in-beam count rate reduces to a rate countable out-of-beam. This two-second delay erases the possibility of any prompt side feeding from short-lived states. The timescale of any potential side feeding would have to be on the same order as the 2.5-minute metastable isomer in  $^{53}\text{Fe}$  to cause the observed problem. Beta-decay branches from  $^{53}\text{Co}$  are also impossible due to the 0.25-second half-life of this nucleus.

Lifetime curves produced by gating on the 701-, 1012-, 1328- and 2340-keV transitions in the energy spectrum and projecting the J624 time spectrum are shown in Figure 3.7. These curves all exhibit the same lifetimes, meaning the only possible side feeding would have to have the exact same lifetime as the  $J^\pi = 19/2^-$  state. Also,  $\gamma$ - $\gamma$ -coincidences were collected in the December experiment to further investigate the possibility of side-feeding into the unbalanced states. Coincidence spectra with gates on the 701-, 1012-, and 1328-keV transitions are shown in Figure 3.8. These spectra do not contain any unidentified contaminants, definitively ruling out side feeding as a potential cause of the imbalances observed in Table 3.8.

Table 3.2 showed the intensities obtained for the singles component of the sulfur-magnesium data in the December experiment. What is immediately clear is that the  $\gamma$ -decay imbalances observed in the prior sulfur experiments (May) have not been reproduced, and, that the transition intensities agree with the lithium-vanadium (May) results. The main difference between the two sulfur-magnesium experiments is that the May experiment operated at a significantly higher count rate; the December experiment used an order of magnitude less beam current. Note

Experiment	1328 keV state	2340 keV state
Vanadium Close	1.009(16)	1.001(13)
Vanadium Far	1.013(21)	1.045(50)
Sulfur Close	1.044(22)	1.140(22)
Sulfur Far	1.058(18)	1.141(29)
Sulfur December	1.016(15)	1.001(10)

**Table 3.8:** Intensity balances for the 1328- and 2340-keV states in the three moveable detectors for each experiment. Values greater than one indicate that there is more decay depopulating the state than there is feeding it.

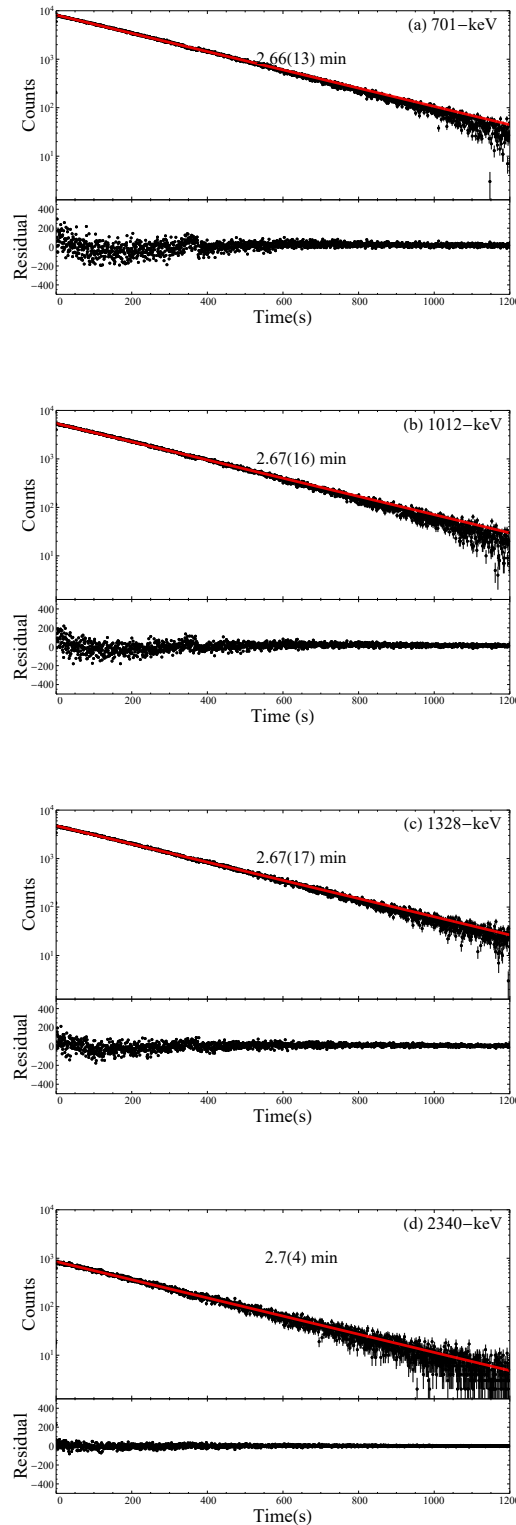


**Figure 3.7:** Lifetime curves for strong transitions in the decay of  $^{53}\text{m}\text{Fe}$ . (a) 701-keV transition, (b) 1012-keV transition, (c) 1328-keV transition and (b) 2340-keV transition. Each curve shows the same half-life, all of which agree with literature values, ruling out the possibility of side feeding into states that might explain the intensity imbalances at the 1328- and 2340-keV states. The deviations present in each of the measurements at the beginning of the decay curve are a likely effect of dead times in the detectors due to the high count rates at the start of each measurement cycle.

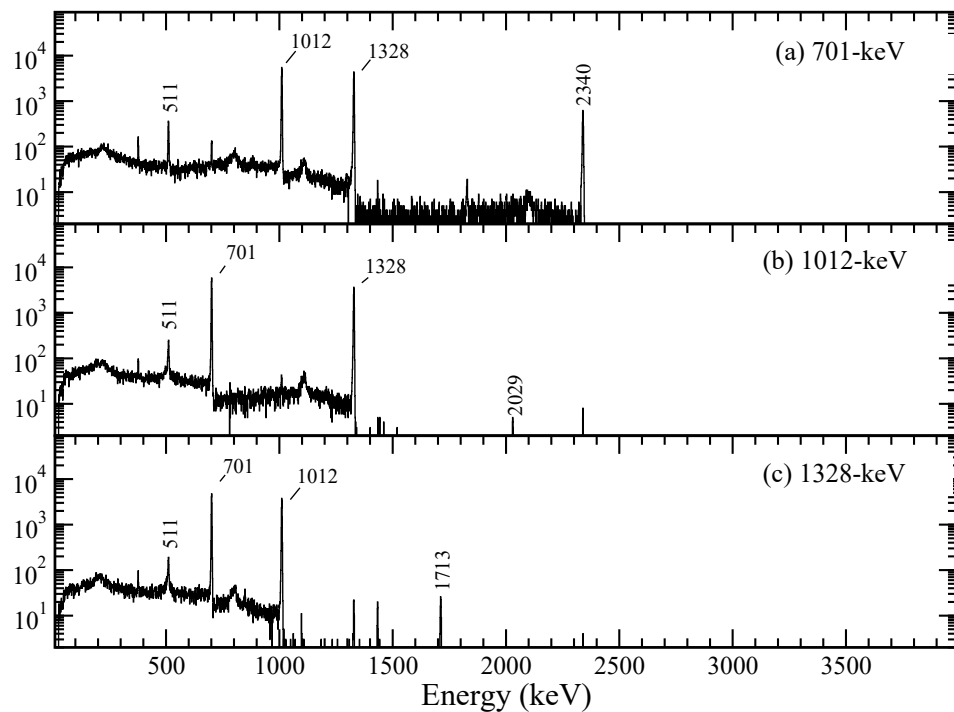


**Figure 3.8:**  $\gamma$ - $\gamma$  coincidence spectra for transitions in  $^{53m}\text{Fe}$ . These gates show that there is no evidence of significant side-feeding into any of the states below the  $J^\pi = 19/2^-$  isomer.

that both experiments used a  $3.3 \text{ mg/cm}^2$  thick magnesium target thus, the two beam-current readings were performed under similar conditions. Stemming from this, the May experiment, by operating at high count rates, exposed the detectors to a significantly higher level of neutron damage. Indeed, between the May and December experiments, four of the detectors were annealed to repair the damage caused by the high neutron flux. This presents the following hypothesis: that using a high beam current to maximise the count rate led to large levels of neutron damage to the detectors and this resulted in events not being recorded properly.

### 3.3.1 Investigating the effects of count rate, detector position and efficiency

In order to test this hypothesis and to quantify its effects, transition intensities were measured in each detector, for each run file, for both reactions in the May experiments. If neutron damage is responsible, the intensity imbalances observed will be correlated with time, and will affect detectors at forward angles more due to neutrons being kinematically focused and preferentially emitted in the direction of the beam. Table 3.9 shows the transition intensities observed in each detector during the first run file (run 12) of the sulfur-magnesium experiments, which had the moveable detectors pulled back. What is clear from this table is that only certain detectors are exhibiting imbalances outside the limits of uncertainty. Detectors 3 and 6 are measuring intensities of 1118(5) and 1057(6) for the 1328-keV transition relative to the 701-keV transition. For comparison, a relative intensity of 801(6) is measured in Detector 5. Detectors 7, 8 and 9 are unbalanced, similar to Detectors 3 and 6, although to a lesser extent, with an average  $\Gamma_{2340}$  value of 1.15 and no transition carrying an intensity higher than the 701-keV transition.

Note that Detectors 3, 6, 7, and 9 all sit at forward angles relative to the path of the beam. Plotting the  $\Gamma_{2340}$  balances as a function of the detector angle relative to the beam axis (Figure 3.9) confirms that the detectors at forward angles exhibit the greatest  $\Gamma_{2340}$  values. This, however, doesn't explain the imbalances present in the backward angle detectors, in particular, Detector 8 which has a large  $\Gamma_{2340}$  value of

1.116(4).

If the imbalances are symptomatic of neutron damage, then detectors subtending a large portion of solid angle, or, somewhat equivalently, detectors with a high efficiency, will have a greater rate of neutron absorption and therefore larger  $\Gamma_E$  values. Detector 8 is a large volume detector and has the highest efficiency in the array. Figure 3.10 shows the  $\Gamma_{2340}$  value for each detector as a function of its efficiency. Detectors at forward angles are indicated by the filled circles and they sit drastically above the rest of the detectors. For the detectors at non-forward angles, a trend of increasing  $\Gamma_{2340}$  value as a function of efficiency is present, indicated by the red line fit to the data for this subset of detectors (open circles). The same dependence also appears to be present for detectors at forward angles, with the more efficient Detectors, 3 and 7, sitting above Detectors 6 and 9 in their respective angle pairs<sup>3</sup>. However, with few data points for forward angles it is difficult to confidently ascribe the greater  $\Gamma_{2340}$  values in each detector to its larger efficiency, but there is some evidence of a trend of this nature.

---

<sup>3</sup>Detectors 7 and 9 are not at the exact same angle, but have a  $\Delta\theta$  of only 4°.

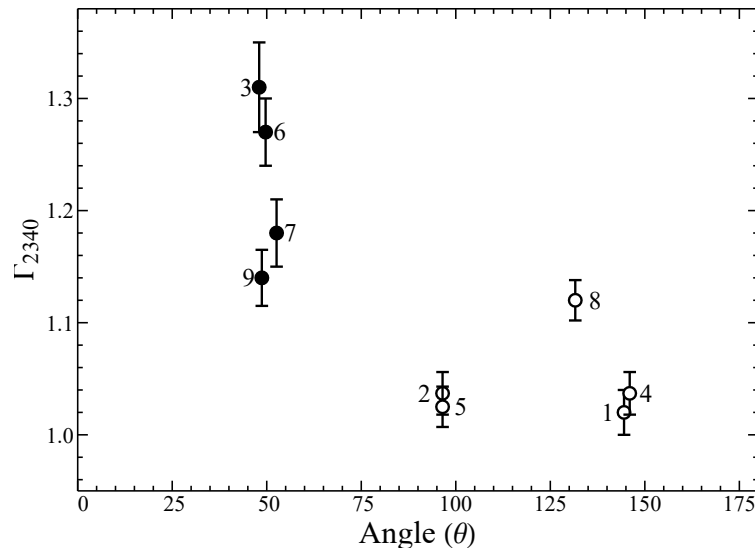


**Figure 3.9:**  $\Gamma_{2340}$  plotted against detector angle where the beam direction is  $0^\circ$ .

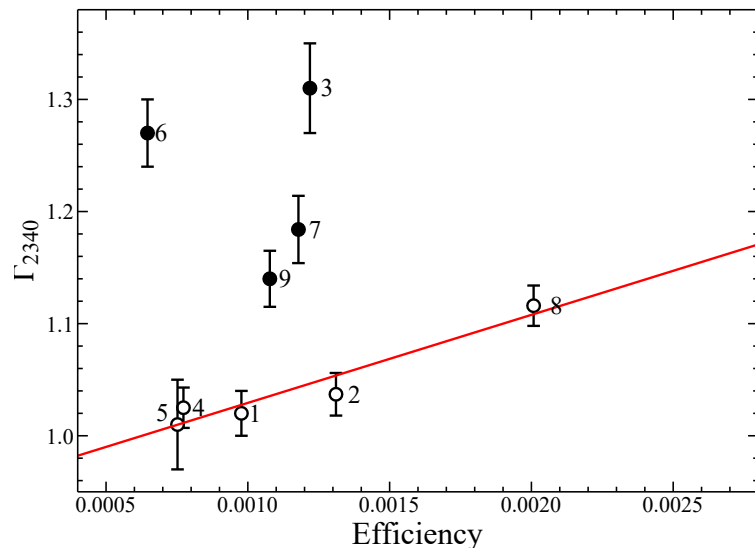


**Figure 3.10:**  $\Gamma_{2340}$  plotted against detector efficiency. Points in black indicate detectors at forward angles while the red line indicates a linear fit to the open data points.

Peak	Li-V (close)	Det.1	Det. 2	Det. 4	Det. 5	Det. 3	Det. 6	Det. 7	Det. 8	Det. 9
701	1000(68)	1000(23)	1000(20)	1000(20)	1000(39)	1000(31)	1000(23)	1000(27)	1000(18)	1000(24)
1012	790(55)	792(19)	806(16)	796(15)	788(31)	963(30)	935(22)	897(25)	858(15)	869(21)
1328	817(57)	836(20)	837(17)	822(16)	801(32)	1118(35)	1057(25)	987(27)	919(17)	941(23)
1713	12.5(1)	12.5(7)	11.9(5)	12.9(7)	13.4(9)	19.4(8)	18.4(8)	14.5(8)	13.5(5)	14.3(6)
2340	222(16)	229(6)	231(5)	228(5)	219(9)	342(11)	336(8)	287(8)	258(5)	275(7)
$\Gamma_{1328}$	1.009(16)	1.04(3)	1.024(21)	1.016(19)	1.00(4)	1.14(4)	1.10(3)	1.08(3)	1.055(19)	1.07(3)
$\Gamma_{2340}$	1.013(21)	1.02(2)	1.037(19)	1.025(18)	1.01(4)	1.31(4)	1.27(3)	1.18(3)	1.116(18)	1.14(3)

**Table 3.9:**  $\gamma$ -ray intensities measured in run file 12 for each of the detectors. Detectors 7, 8 and 9 are pulled back from the target at this point in the experiment. Detectors 3, 6, 7, 8, and 9 exhibit the worst  $\Gamma_E$  balances with typical values for  $\Gamma_{2340}$  being greater than 1.1. In contrast, Detector 5 has values consistent with the lithium-vanadium experiments. The 3041 keV peak has been omitted from this table due to the poor statistics for this branch that can be measured in a single detector.

Figure 3.11 shows the  $\Gamma_{2340}$  value for Detectors 3, 5 and 6 throughout the run. The  $\Gamma_{2340}$  values are relatively constant for the early portions of the experiment, however, once the sulfur-magnesium experiment starts, Detectors 3 and 6 begin showing increased  $\Gamma$  values. For Detector 5, during the sulfur-magnesium experiments,  $\Gamma_{1328}$  and  $\Gamma_{2340}$  remain near  $\Gamma_E=1$ , while data from Detectors 1, 2 and 4 are associated with  $\Gamma_E = 1.02$ . This is significantly less than the changes observed in the forward Detectors 3 and 6, the worst affected by neutron damage, that exhibit imbalances between  $\Gamma_{2340}=1.2\text{--}1.3$ . That the  $\Gamma_E$  values remain relatively constant, and close to one, for all detectors in the lithium-vanadium experiments, indicates that this data can be trusted, while the surge in  $\Gamma_E$  that occurs during the sulfur-magnesium experiments is strong evidence for dismissing that data. The fluctuations in  $\Gamma_{2340}$  in the lithium-vanadium run files appear to be due to normal statistical variances, with no correlation observed for the magnitude and direction of the changes relative to changing count rates or time.

The inconsistency of  $\Gamma_E$  values between run-files for a given detector is an indication that the imbalances observed are not due to an incorrectly determined efficiency curves for that detector. With small tweaks to the efficiency curve parameters, different curves may be fit to the data with small residuals and changes to the intensity balances on the order of a few percent can be produced. However, nothing close to the 20% required to balance the intensity in Detector 6, for instance, could be achieved by tweaking the efficiency curves. Figure 3.12 shows  $^{53m}\text{Fe}$  spectra for Detectors 4, 5 and 6 for the May sulfur-magnesium experiment. In the spectra, the areas of the 377-keV  $^{53}\text{Mn}$  decay line<sup>4</sup> in Detectors 4 and 5 have been normalised to the 377-keV peak area in Detector 6 (factors of 1.23 and 1.56, respectively) such that the areas of each peak in the spectrum should in principle be the same. For Detectors 4 and 5 there is little difference in the scaled spectra with both peaks having approximately the similar heights and areas. For Detector 6, the areas of each of the  $^{53m}\text{Fe}$  decay peaks, following the normalisation, are all greater than they are in Detector 4, these values are shown in Table 3.10. Though not shown in Table 3.10, the fitted area of every peak (not just the  $^{53m}\text{Fe}$  decay) in the scaled

<sup>4</sup>Populated in the beta decay of the  $^{53}\text{Fe}$  ground state.

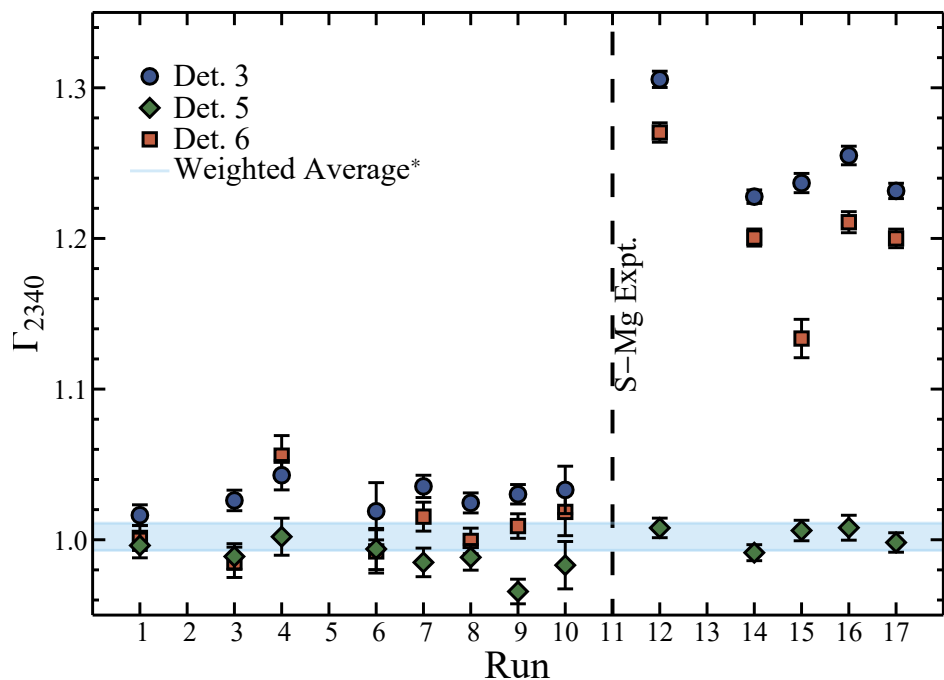


**Figure 3.11:**  $\Gamma_{2340}$  for selected detectors in each run file in the May experiments. The filled horizontal section through the graph indicates the value of  $\Gamma_{2340}$  as measured in the December singles experiments using the summed spectra of all the detectors with one standard deviation either side of this value. Runs 2, 5, 11 and 13 had little to no data in them and have thus been excluded from the plot.

**Table 3.10:** Peak areas obtained for Detectors 4, 5 (following the normalisation discussed in text) and 6. The ratios shown correspond to the ratios of the peak area for the indicated detectors following the normalisation (discussed in text).

$E_\gamma$ (keV)	Det.4	Det. 5	Det. 6	$\frac{\text{Det.5}}{\text{Det.4}}$	$\frac{\text{Det.6}}{\text{Det.4}}$
701	90729(310)	100723(327)	117536(370)	1.110(5)	1.295(6)
1012	52990(237)	62180(257)	82509(320)	1.173(7)	1.557(9)
1328	43308(213)	52274(234)	75376(317)	1.207(8)	1.74(1)
1713	522(25)	723(33)	1056(46)	1.38(9)	2.02(13)
2340	7191(89)	9159(119)	15018(135)	1.27(2)	2.09(3)

Detector 4 spectrum is less than in Detector 6, with a increasing trend as a function of energy. A scatter plot showing the ratios of the areas measured in Detectors 6 and 4 is shown in Figure 3.13.

Of the three detectors tested in this analysis, Detector 4 is the most efficient and Detector 6 is the least efficient. That the forward angle Detector 6 counts more events than backward angle Detector 4, following a normalisation of the  $\gamma$ -ray spectra using the 377-keV  $^{53}\text{Mn}$  peak area, is indication that there is an unexplained surplus of events in Detector 6 relative to Detector 4. This relative surplus of events appears to be correlated with the large  $\Gamma_E$  values in forward angle detectors and is a good indication that the sulfur-magnesium data should be discarded.

### Conclusions of this investigation

Considering the evidence described above, it appears that imbalances present in the sulfur-magnesium data have some dependance on the neutron flux into a detector. Detectors at forward angles or with high efficiencies (volumes) experience the greatest neutron fluxes and appear to correlate with the largest pathological  $\Gamma_E$  values. Figures 3.9 and 3.10 have illustrated this. While correlations may be present, they do not explain the physical reason why extra events, that is, detectors counting at a rate greater than their measured efficiency relative to the other detectors in CAESAR would imply, increasing proportionally as a function of energy, appear to be present in the detectors that show the greatest  $\Gamma_E$  values. An initial hypothesis was that dead times would cause missing events and the decay

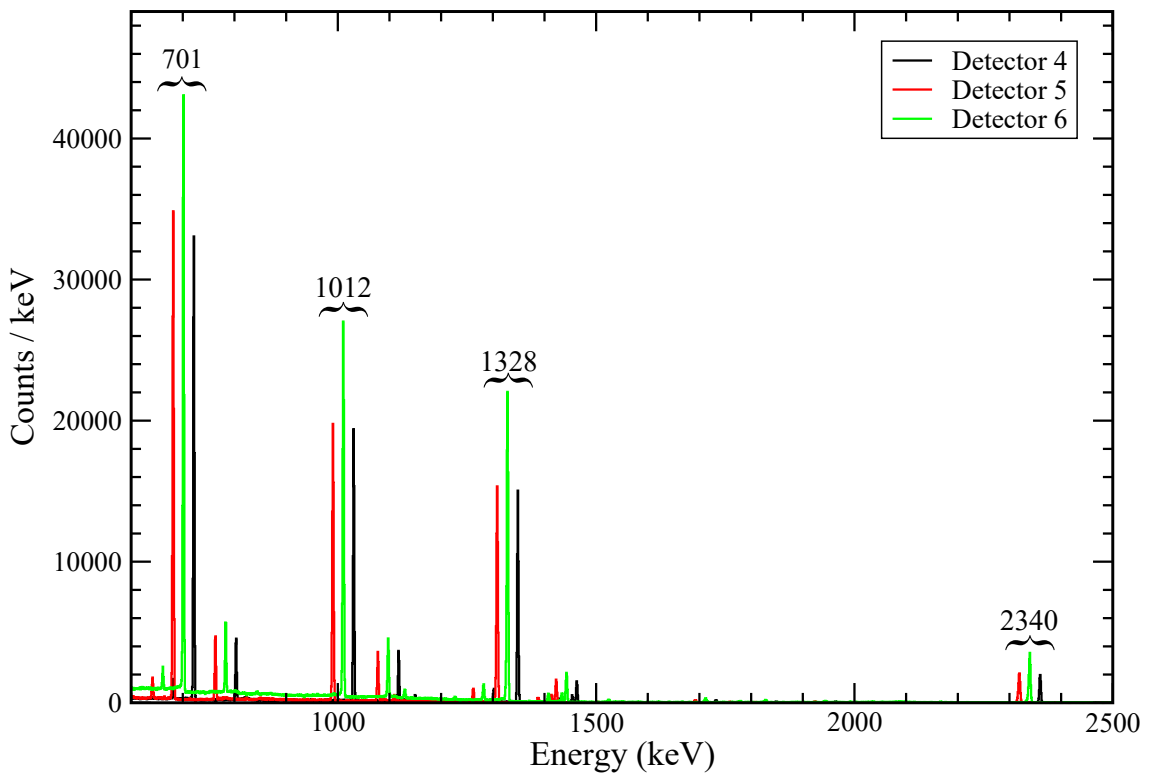


**Figure 3.12:** Overlayed spectrum of Detectors 4 (black), 5 (red) and 6 (green) with each detector scaled to have the same number of counts in the 377-keV peak, the black and red spectra have been shifted by 10-keV either side of the green spectrum. The heights of the 1012 and 1328-keV peaks differ significantly between Detectors 4 and 5, and Detector 6.

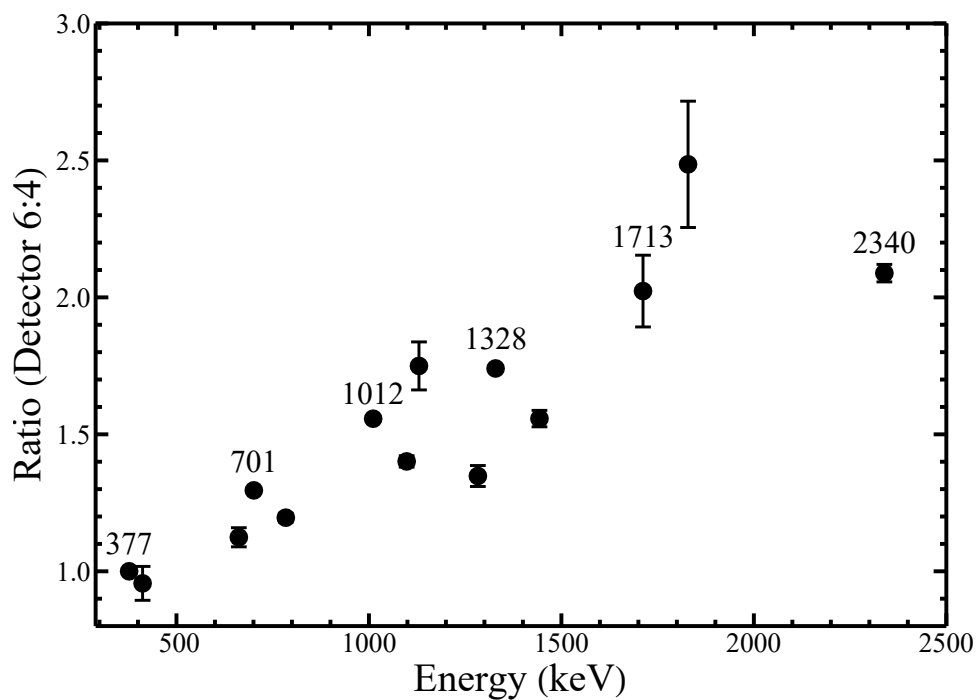


**Figure 3.13:** Ratio of the peak areas measured in Detector 6 to the areas measured in Detector 4. The labeled points correspond to the  $^{53m}\text{Fe}$  decay peaks while the unlabeled points are other decay lines in the  $\gamma$ -ray spectrum. Prior to the ratio being taken, the Detector 4 peak areas were scaled by the ratio of the 377-keV  $^{53}\text{Mn}$  line in Detectors 6 and 4 such that both spectra should, in principle, have a similar number of counts in each peak.

through the level scheme would become consequently imbalanced; this proved not to be the case. Appendix 2 further details the symptoms of neutron damage and describes potential methods of correcting the data to bring it in line with the lithium-vanadium results. These corrections were performed as an academic exercise to help build confidence in the data analysis procedures and develop a sense of potential problems that could occur. The results should be considered secondary to the branching ratios already obtained in Section 3.2.3.

# 4

## Chapter 4

# Monte Carlo simulation of $^{53m}\text{Fe}$ decay

---

The Monte Carlo simulation discussed in Section 2.3 has been used to examine the outcome of a series of branching ratio conditions applied to the  $^{53m}\text{Fe}$  decay. The experimentally obtained branching ratios have not been used as the simulation is generally incapable of perfectly replicating these results. Hence, using the exactly obtained experimental branching ratios is an unnecessary exercise. Instead, the simulation has been used to investigate what happens when different branching ratios are used, for example, changing the strength or even existence of the E6 branch. The following sections will examine the simulation results for a number of input branching ratios and explore sum-coincidence events (particularly those predicted by the TM) in more detail.

## 4.1 Simulation conditions

Each simulation performed 100,000,000 decays through the  $^{53m}\text{Fe}$  level scheme starting at the  $J^\pi = 19/2^-$  isomer; this number was chosen to insulate against statistical fluctuations in the number of low-probability events occurring. This number of decay events also generates statistical levels similar to those obtained in the lithium-vanadium experiment, with a small normalisation<sup>1</sup> between the simulation and experiment results applied to make the results directly comparable. Furthermore, each simulation was performed five times to gauge the variance in the results between each simulation. This has been incorporated into the results as the uncertainty in the simulated measurement by taking the mean and standard deviation of the simulation output. The simulations were carried out using six different sets of initial conditions for the  $J^\pi = 19/2^-$  state branching ratios; these are shown in Table 4.1.

The first set of simulations with the E6 branching ratio set to 0 were performed twice: once without the effects of angular correlations incorporated into the detection logic; and once with the effects incorporated. The theoretical angular correlations at  $0^\circ$  used in the simulation are shown in Table 4.2 while the angular correlations plotted over the full angular range are shown in Figure 4.1. Transitions were assumed to be pure, with only the 1012- and 1328-keV transitions having a mixing ratio included. The value of  $\delta(E2/M1) = -0.11$  for both transitions<sup>2</sup> was taken from experimental results in Ref. [Saw73]. The results of the simulation in the form of counts due to sum coincidences with and without angular correlations are shown in Table 4.3 along with the experimentally determined sum-coincidence components of the four possible sum peaks and their theoretically estimated yields (obtained using the methods in Section 2.2).

The results in Table 4.3 show that including the effect of the angular correlations can more correctly replicate the number of sum-coincidence events predicted by

<sup>1</sup>The data sets were normalised using the ratio of the experimental 701-keV decays to the simulated 701-keV decays

<sup>2</sup>The sign convention used by Sawa [Saw73] has a positive sign for these mixing ratios, the code used in this work for calculation of angular correlations uses the opposite sign convention so they will be referred to here as negative.

**Figure 4.1:** Angular correlations for the 701–2340-keV and 701–1012-keV cascades in  $^{53m}\text{Fe}$ , plotted as a function of the separation angle with respect to the angle of emission of the 701-keV transition between the detectors that observe the two transitions.

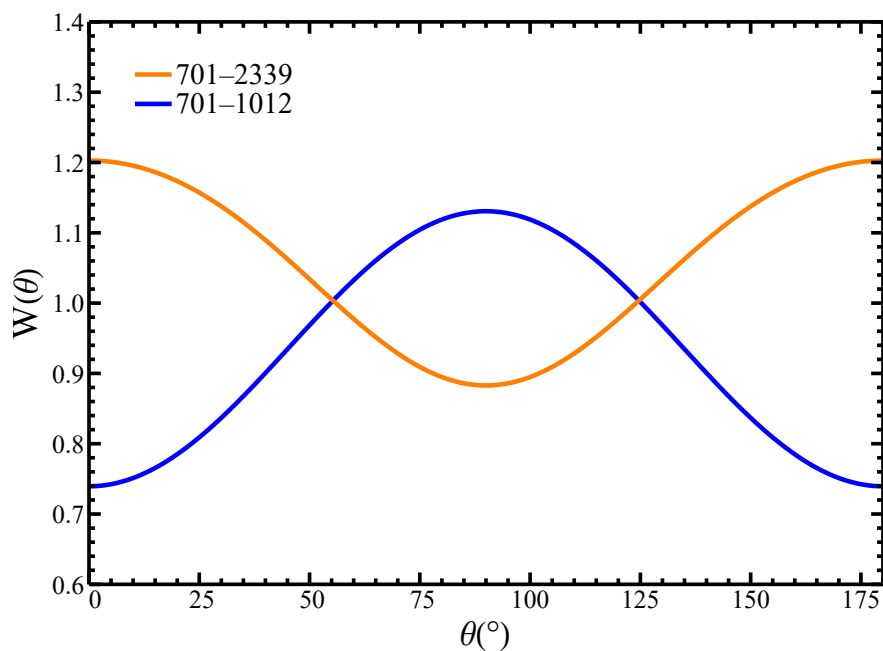


**Table 4.1:** Input branching ratios for the  $J^\pi = 19/2^-$  state used in each simulation. Branching ratios for the  $J^\pi = 11/2^-$  state were held constant at 0.79 and 0.21 for the 1012-keV and 2340-keV transitions, respectively. The simulation does not consider internal conversion as this process is essentially negligible given the high energies of the transitions involved.

Model No.	Input Branching Ratio ( $\times 10000$ )		
	3041-keV	1713-keV	701-keV
1	0	80	9920
2	2	80	9918
3	4	80	9916
4	6	80	9914
5	6	100	9894
6	6	120	9874

**Table 4.2:** Angular correlation for each of the possible  $\gamma$ -ray cascades in  $^{53m}\text{Fe}$  at  $0^\circ$ .

Cascade	$J_i^\pi \rightarrow J_j^\pi \rightarrow J_k^\pi$	Correlation at $0^\circ$
701-2340	$19/2^- \rightarrow 11/2^- \rightarrow 7/2^-$	1.2028
701-1012	$19/2^- \rightarrow 11/2^- \rightarrow 9/2^-$	0.7935
701-1328	$19/2^- \rightarrow 11/2^- \rightarrow 9/2^- \rightarrow 7/2^-$	0.7447
1012-1328	$11/2^- \rightarrow 9/2^- \rightarrow 7/2^-$	1.1675
1713-1328	$19/2^- \rightarrow 9/2^- \rightarrow 7/2^-$	0.7137
701-1012-1328	$19/2^- \rightarrow 11/2^- \rightarrow 9/2^- \rightarrow 7/2^-$	0.602

the TM. In both cases, the agreement between simulation and the TM has improved compared with not omitting the angular correlations, but not to a degree that would necessitate its inclusion. The sum coincidence components measured, in reproducing the TM, do not replicate those deduced from the experimental data (SM and GM). In each case there is a large difference between the simulated number of sum-events and those obtained from experiment. A different mixing ratio for the 1012- and 1328-keV transitions could be invoked to explain the discrepancy between the experimental and simulation results for the 2029-keV sum-coincidence counts. An admixture of  $|\delta| = 0.75$  for the 1328-keV transition, with no change to the 1012-keV transition's mixing ratio, is required to have the simulation match the experimentally measured intensity of the 2029-keV sum-coincidence peak. A mixing ratio of this magnitude is not feasible considering the measured values of  $\delta = -0.11(2)$  for the 1328- and 1012-keV transitions obtained by Sawa [Saw73] or the similar value of  $-0.15(3)$  for the 1328-keV transition obtained by Nelson et al [Nel73].

**Table 4.3:** Number of sum-coincidence events obtained in the simulation for each potential sum-coincidence peak with and without the effects of angular correlations (Ang.).

Peak	Counts				
	No Ang.	Ang.	TM	SM	GM)
1713	1963(51)	1372(31)	1421(38)	708(91)	396(1118)
2029	1655(24)	1154(59)	1226(32)	589(65)	589(65)
2340	1309(16)	1403(45)	1515(40)	729(94)	-18136(12505)
3041	291(21)	344(14)	365(9)	201(26)	209(128)

**Table 4.4:** Ratio of simulated to experimental counts measured for each real and sum-coincidence peak in  $^{53m}\text{Fe}$ , for the close geometry, as a function of the input branching ratios (B.R) shown in Table 4.1. The ratios include both the real and sum-coincidence component of the peak. The simulation and experiment data sets have been normalised using the ratio of the number of 701-keV decays.

Peak	simulation counts/experimental counts						
	B.R. for 3041-keV $\gamma$ -ray ( $\times 10000$ )				B.R. for 1713-keV $\gamma$ -ray ( $\times 10000$ )		
	$0^1$	$2^1$	$4^1$	$6^1$	$100^2$	$120^2$	
701	1.00(5)	1.00(5)	1.00(5)	1.00(5)	1.00(5)	1.00(5)	1.00(5)
1012	1.00(5)	1.00(5)	1.00(5)	1.00(5)	1.00(5)	1.00(5)	1.00(5)
1328	0.96(5)	0.96(5)	0.97(5)	0.97(5)	0.97(5)	0.97(5)	0.97(5)
1713	0.91(5)	0.91(5)	0.91(5)	0.91(5)	1.08(6)	1.25(7)	
2029	2.0(3)	2.1(3)	2.0(3)	2.0(3)	2.1(3)	2.0(3)	
2340	0.97(5)	0.97(5)	0.97(5)	0.97(5)	0.97(5)	0.97(5)	
3041	0.91(7)	1.07(9)	1.26(11)	1.40(13)	1.38(10)	1.42(12)	

<sup>1</sup> 1713-keV transition branching ratio held constant at 80 ( $\times 10000$ ) as per the simulation conditions in Table 4.1.

<sup>2</sup> 3041-keV transition branching ratio held constant at 6 ( $\times 10000$ ) as per the simulation conditions in Table 4.1.

## 4.2 Simulation results and comparison to experiment

The ratios of the simulated counts to the experimentally obtained counts as a function of the input branching ratio are shown in Table 4.4 for the close geometry and Table 4.5 for the far geometry.

For the 1328-keV and 2340-keV transitions, the simulation consistently under estimates the intensity of these transitions. This suggests that the efficiency used to determine the detection probability may have been slightly too low. For the 2340-keV transition in particular, the deficit is quite large in the far geometry simulations indicating that the branching ratio of 0.21 used may have also been too

**Table 4.5:** Ratio of simulated to experimental counts measured for each real and sum-coincidence peak in  $^{53m}\text{Fe}$ , for the far geometry, as a function of the input branching ratios (B.R) shown in Table 4.1. The ratios include both the real and sum-coincidence component of the peak. The simulation and experiment data sets have been normalised using the ratio of the number of 701-keV decays.

Peak	simulation counts/experimental counts					
	B.R. for 3041-keV $\gamma$ -ray ( $\times 10000$ )				B.R. for 1713-keV $\gamma$ -ray ( $\times 10000$ )	
	$0^1$	$2^1$	$4^1$	$6^1$	$100^2$	$120^2$
701	1.00(3)	1.00(3)	1.00(3)	1.00(3)	1.00(3)	1.00(3)
1012	0.98(3)	0.98(3)	0.98(3)	0.98(3)	0.98(3)	0.98(3)
1328	0.94(3)	0.94(3)	0.94(3)	0.94(3)	0.94(3)	0.95(3)
1713	0.84(4)	0.84(4)	0.84(4)	0.84(3)	1.01(4)	1.19(5)
2029	1.9(3)	1.9(3)	1.9(3)	1.9(3)	1.8(3)	1.9(3)
2340	0.91(3)	0.91(3)	0.91(3)	0.91(3)	0.91(3)	0.91(3)
3041	0.79(7)	0.96(11)	1.13(11)	1.29(13)	1.24(12)	1.32(14)

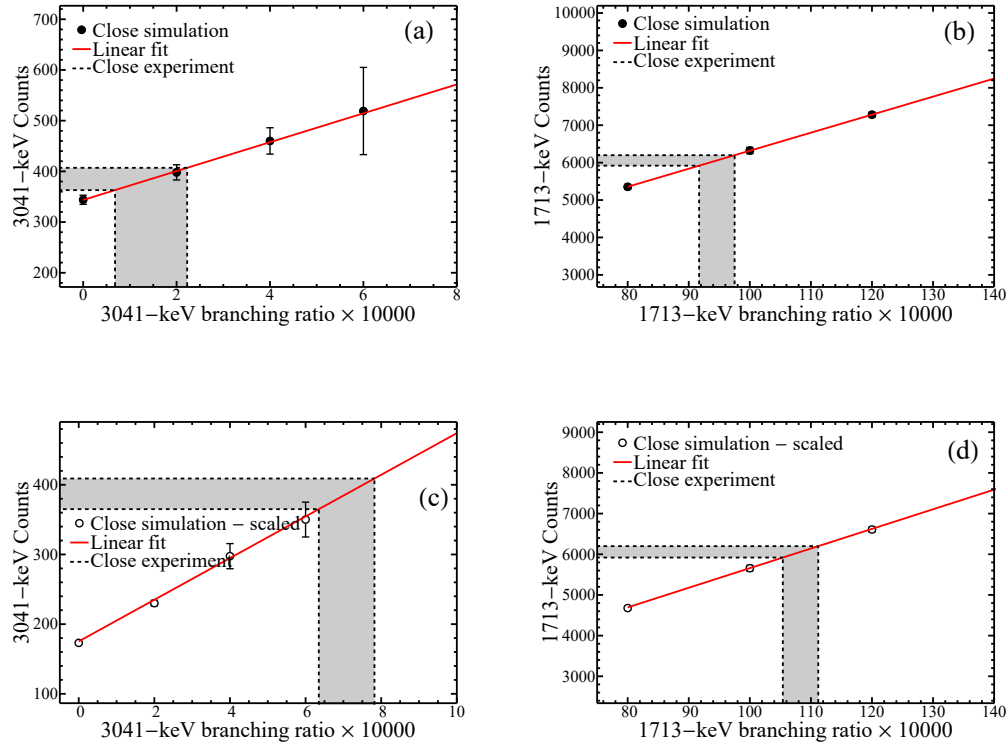
<sup>1</sup> 1713-keV transition branching ratio held constant at 80 ( $\times 10000$ ) as per the simulation conditions in Table 4.1.

<sup>2</sup> 3041-keV transition branching ratio held constant at 6 ( $\times 10000$ ) as per the simulation conditions in Table 4.1.

small. Repeat simulations using the experimentally measured value of 0.23 have been performed, and the deficit for this transition has decreased, correspondingly the deficit for the 1012-keV and 1328-keV transitions has increased.

The 1713-keV transition is not as well reproduced by the default input branching ratio of 0.008, underestimating the experimental number of counts by about 9%. The subsequent trials using branching ratios of 0.01 and 0.012 for this transition greatly over estimate its intensity with deviations of 8% and 15%, respectively. Given the dominant, real component will vary linearly with the input branching ratios, the intersection of the simulated peak intensity and experimental peak intensity can be found using linear regression. As the 1713-keV sum-coincidence component is due to the summation of the 701-keV and 1012-keV transitions, it can be assumed that the sum-coincidence component of the peak will remain constant when making the small decreases to the intensity of the 701-keV transition required to accommodate an increase in the 1713-keV transition. The regression analysis is illustrated in panel (b) of Figure 4.2. In this plot, the grey region indicates the input branching ratio required to reproduce the experimentally observed peak area plus or minus one sigma. The intersection of simulation and experiment occurs at an

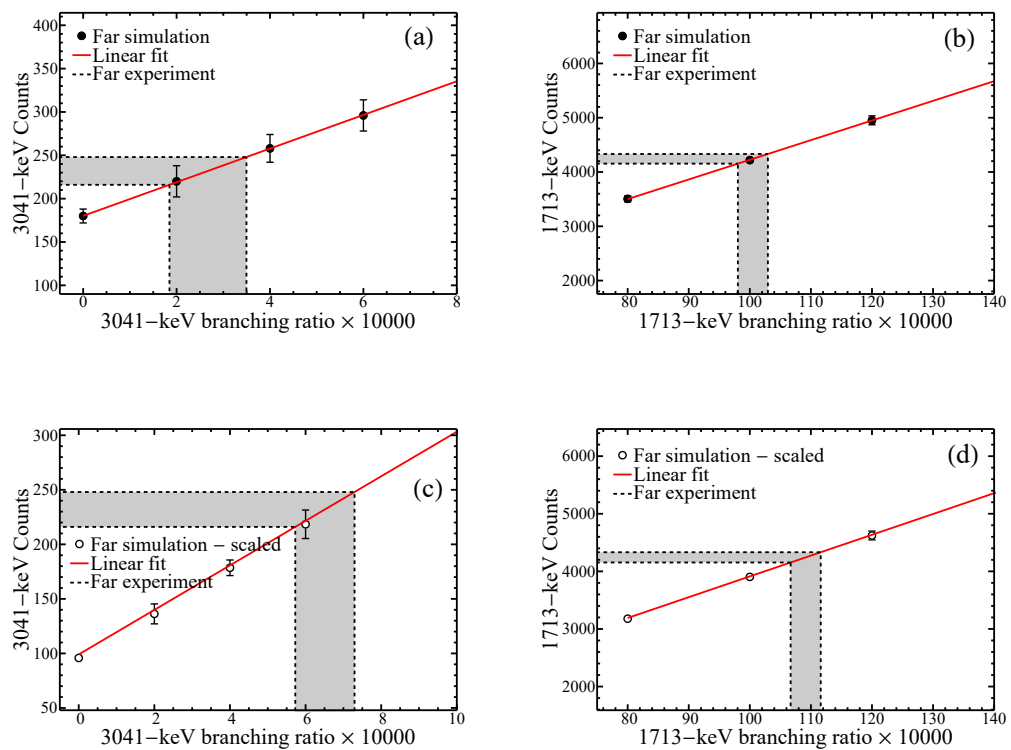
**Figure 4.2:** 3041-keV and 1713-keV transition total intensities plotted as a function of branching ratio for the close geometry. The grey region indicates the input branching ratio required for the simulation to match the experimental intensity. Panels (a) and (b) show this analysis for the unscaled simulation output while panels (c) and (d) use the scaling method discussed in the text to reduce the sum-coincidence component of the peaks.



input branching ratio of 0.0095(3).

In the far geometry simulations, the 1713-keV peak deficit using the initial branching ratio of 0.008 has increased to 16%. This initially wider deficit has decreased the deficits from the 0.01 and 0.012 branching ratios to 1% and 19%. Consequently, the input branching ratio required to reproduce the experimental intensity is higher for the far geometry simulation than it is for the close geometry simulation with the intersection occurring at an input branching ratio of 0.100(2). The widening deficit for this transition is consistent with the increased deficits for the 1012-keV, 1328-keV and 2340-keV transitions when moving to the far geometry, though the proportional difference is different for each transition making no real trend identifiable.

**Figure 4.3:** 3041-keV and 1713-keV transition total intensities plotted as a function of branching ratio for the far geometry. The grey region indicates the input branching ratio required for the simulation to match the experimental intensity. Panels (a) and (b) show this analysis for the unscaled simulation output while panels (c) and (d) use the scaling method discussed in the text to reduce the sum-coincidence component of the peaks.



The 3041-keV transition intensity, with an input branching ratio of 0, does not match the experimental intensity providing further evidence of a real component to the peak. Agreement with the experimental intensity occurs within one sigma using input branching ratios of either 0.0002 or 0.0004 (within one  $\sigma$ ) for the far geometry simulations and slightly below 0.0002 for the close geometry. Performing the same regression analysis on the 3041-keV branch (illustrated in panel (a) of Figures 4.2 and 4.3), the input branching ratio required to reproduce the experimental results occurs at 0.00015(8) for the close geometry and 0.00027(8) for the far geometry. This is still consistent with a real E6 transition albeit with a large drop in intensity relative to the experimental and literature values. As the simulation does not correctly reproduce the sum-coincidence intensity of the 2029-keV peak and, therefore, can be assumed to overestimate the other sum-coincidence components in the other peaks<sup>3</sup>, the decrease in the E6 branching ratio compared to the experimental methods is unsurprising as a greater portion of the peak area is suggested to be due to sum-coincidences. The overabundance of 2029-keV sum-coincidence events was reproduced in two other Monte Carlo simulations independently written in two different languages. In Section 3.2.2, the sum-coincidence intensity from the TM analysis was scaled by the ratio of the predicted 2029-keV peak area and experimental 2029-keV peak area. As the simulation similarly overestimates the sum-coincidence intensity of the 2029-keV peak the same scaling method has been employed here; in each case, the scaling factor required for the sum-coincidence proportion of the peak was around 2. Table 4.6 shows the scaled sum-coincidence events for each of the simulations, alongside the experimentally obtained sum-coincidence numbers.

For both geometries, the scaled sum-coincidence intensities better match the experimentally obtained numbers. Scaling the sum-coincidence intensities in this way increases the input branching ratio required for the simulation to reproduce the experimentally observed peak area, the scaled regression plots are shown in panels (c) and (d) of Figures 4.2 and 4.3 for the 3041-keV and 1713-keV transitions,

---

<sup>3</sup>Both the simulation and TM, model each of the possible sum-coincidences with the same physics logic and same absolute efficiency, meaning that if one is being over estimated then both of them are likely being over estimated.

respectively. For the 3041-keV transition, input branching ratios of 0.00065(8) (far) and 0.00071(7) (close) are required to reproduce the experimental results; these numbers are now in-line with those obtained from experiment (0.00059(7)), with the close geometry input branching ratio agreeing within  $2\sigma$ .

For the 1713-keV transition, agreement between both simulation geometries has also improved with the required branching ratios increasing to 0.0109(2) (far) and 0.0108(3) (close), both of these branching ratios agreeing with the experimental value of 0.0112(7). The branching ratios from the scaled and unscaled simulation results suggest bounds on the E6 and M5 branching ratios and demonstrate the input conditions required to reproduce the experimental transition intensity. The minimum branching ratio value for the E6 transition is  $2\sigma$  above zero (0.00015(8)), suggesting a real E6 transition is required to reproduce the experimental 3041-keV intensity. This being said, because the simulation requires a scaling correction to reproduce the real transition intensities, these simulation results are somewhat schematic in nature, serving to show that the E6 has a real component. The experimental branching ratios obtained in Chapter 3 will be used to deduce the transition strengths in the next chapter.

The need for the scaling factor to reproduce the results of the SM and GM methods is almost certainly due to the error in the absolute efficiency that was identified and discussed in Section 2.2. The simulations will be redone prior to future publication of the results. Unfortunately, there was insufficient time to do this prior to submission of the thesis.

**Table 4.6:** Sum-coincidence component of  $^{53m}\text{Fe}$  decay peaks averaged over all of the simulations. ‘Pre’ indicates the intensity prior to being scaled and ‘post’ indicates the intensity after being scaled. The experimentally obtained sum-coincidence yields are shown at right for the SM and GM analyses (see section 3.2.1).

Peak	Close Geometry			
	Counts		SM	GM
	Pre	Post		
1713	1378(8)	694(80)	708(91)	396(1118)
2029	1154(12)	581(67)	589(65)	589(65)
2340	1416(10)	713(82)	729(94)	-18136(12505)
3041	341(3)	172(20)	201(26)	209(128)

Peak	Far Geometry			
	Counts		SM	GM
	Pre	Post		
1713	689(11)	367(63)	372(59)	233(595)
2029	579(8)	309(53)	310(49)	310(49)
2340	723(7)	385(66)	382(61)	-8859(5972)
3041	168(5)	90(16)	95(16)	109(70)

# 5

## Chapter 5

## Discussion

---

The experimentally determined transition strengths for the  $J^\pi = 19/2^-$  state decay are calculated in the first section of this chapter. The subsequent sections discuss the interpretation of high angular-momentum transitions in the fp shell with reference to a number of published shell model calculations in this region. Discussion will largely be limited to the theoretical predictions of the transition strength compared to the experimentally determined values.

### 5.1 Experimental transition strengths

Transition strengths for the E4, M5 and E6 decays, calculated from the branching ratios obtained in Section 3.2.3, are shown in Table 5.1 in both  $W.u$  and  $e^2 \text{ fm}^{2\lambda}$  for electric transitions and  $\mu_N^2 \text{ fm}^{2\lambda-2}$  for magnetic transitions. These have been determined using the  $19/2^-$  state lifetime of  $t_{1/2}=2.54 \text{ min}$  published in Ref. [Jun09] and theoretical internal conversion coefficients calculated using BRICC [Kib08]. Included in this table for comparison are the transition strengths obtained using the values reported in the later work of Black et al [Bla75]. The strengths obtained

**Table 5.1:** Experimental strengths of the E4, M5 and E6 transitions obtained by Black et al [Bla75] and from the present work (P.W). A half-life of 2.54 minutes [Jun09] was used for the  $J^\pi = 19/2^-$  state. The values of internal conversion are all negligible [Kib08].

$E_\gamma$ (keV)	$I_\gamma$	$X\lambda$	B( $X\lambda$ ) W.u		B(E,M $\lambda$ ) ( $e^2$ fm $^{2\lambda}$ , $\mu_N^2$ fm $^{2\lambda-2}$ )	
			[Bla75]	P.W	[Bla75]	P.W
701	0.99(3)	E4	0.2600(3)	0.2600(2)	$6.453(6) \times 10^2$	$6.465(5) \times 10^2$
1712	0.0112(7)	M5	4.13(3)	3.6(2)	$4.2(3) \times 10^5$	$3.6(2) \times 10^5$
3040	0.00059(7)	E6	0.45(8)	0.45(5)	$2.8(5) \times 10^5$	$2.8(3) \times 10^5$

in the present measurement are largely the same.

## 5.2 Shell-model calculations

Calculation of the properties of high-multipole transitions is a sparsely studied subject, due to the rarity of experimental information available to interpret the theoretical predictions. Hexadecapole (E4), triacontaduopole (M5) and hexacontatetrapole (E6) transitions are particularly rare, with only a handful of firm assignments spanning the entirety of the nuclear chart. The following sections will discuss the high-multipole transitions observed in  $^{53m}\text{Fe}$  within the framework of several published shell-model calculations. The details of these calculations, the model spaces and interactions used, as well as a brief primer on deducing the calculated transition strengths, will be presented first.

### 5.2.1 Model spaces and interactions

The choice of interaction can greatly affect the energy spectrum and transition strengths resulting from calculation. Unlike the lower p and sd shells, the pf-shell model space has no interaction capable of effectively describing nuclei over the full valence space [Hon02]. The interactions discussed in this work are shown in Table 5.2 along with the publications in which they were developed. The choice of model determines the single-particle excitation energies (taken relative to the core) and the interactions used to determine the two-body matrix elements. Once the Hamiltonian is specified, energy levels and wavefunctions can be deduced. To

**Table 5.2:** Shell model interactions used in the sampled literature for calculation of high multipolarity transition properties in the region of  $^{40}\text{Ca}$  and  $^{56}\text{Ni}$ .

Interaction	Publication
KB	[Kuo68]
KB-3	[Pov81]
SDI	[Gla67]
SII	[Vau72]
GXFP1	[Hon02]
FPD6	[Ric91]

evaluate transition strengths from the wavefunction requires, in addition, the specification of effective nucleonic charges and  $g$  factors. For some models, the matrix elements are theoretically determined (SDI or KB) but, generally, a semiempirical approach is taken whereby the matrix elements are deduced from experimental data or from least-squared fits to experimental data [Kut78].

With the matrix elements known, excited state energies and transition strengths can be determined. Writing the transition matrix element  $M$  in terms of the proton and neutron matrix elements,  $A_p$  and  $A_n$ , respectively, gives

$$M = A_p e_p + A_n e_n, \quad (5.1)$$

where  $e_p$  and  $e_n$  denote the effective nucleon charges for protons and neutrons [Bro11, Met81]. The transition strength for an electric transition can then be calculated as:

$$B(E\lambda) = \frac{M^2}{2J_i + 1}, \quad (5.2)$$

where  $J_i$  is the angular momentum of the excited state the transition decays from. In many cases it is sufficient to use the bare-nucleon charges of  $e_p = 1e$  and  $e_n = 0e$  [Met81], however, it is generally accepted that  $e_p = 1.5e$  and  $e_n = 0.5e$  can be used to accurately describe E2 transitions across the full pf shell [Bro77, Yok97, Ur98, Gad05]. For higher multipole transitions, it has been found that large core polarisations are required to reproduce the experimentally obtained transition strength; the effective nucleon charges are then expressed in terms of the core

polarisation for a given multipolarity:  $e_p = (1 + \delta_p(E\lambda))e$  and  $e_n = \delta_n(E\lambda)e$ . For instance,  $^{44}\text{Sc}$  requires  $\delta_p(E4) = 1.1$  to reproduce the observed E4 strength, while explaining the retardation of high-multipolarity transitions in  $^{52}\text{Mn}$  and  $^{53}\text{Fe}$  requires large, negative  $\delta_p$  core polarisations [Yok97]. Little discussion concerning  $\delta_n(E\lambda)$  polarizations was given in the literature, however, the contribution of neutrons to the total M is generally small compared to protons.

## 5.3 Shell-model interpretation of high-multipolarity transitions

The origin of the high-multipolarity transitions depopulating the  $J^\pi = 19/2^-$  isomer in  $^{53}\text{Fe}$  can be understood by calculating the excited state energy spectrum for  $^{53}\text{Fe}$  within the  $f_{7/2}$  model space, these were performed using nuShellX [Bro14] using the f754 interaction. The experimental and calculated excited state energies are shown in Figure 5.1. Both the calculation and experimental results show that the  $J^\pi = 13/2^-$ ,  $15/2^-$  and  $17/2^-$  states exist above the  $J^\pi = 19/2^-$  state in excitation energy. This means the only available decay paths from the  $J^\pi = 19/2^-$  state are to the  $J^\pi = 11/2^-$ ,  $9/2^-$  and  $7/2^-$  states giving rise to the E4, M5 and E6 transitions, respectively. This occurs because the residual  $\pi$ - $\nu$  interactions strongly favour the maximal angular momentum coupling i.e. the  $J^\pi = 19/2^- ((\pi f_{7/2})^2_{6+} \otimes \nu f_{7/2})$  state over the  $J^\pi = 17/2^- ((\pi f_{7/2})^2_{6+} \otimes \nu f_{7/2})$ ,  $J^\pi = 15/2^- ((\pi f_{7/2})^2_{4+} \otimes \nu f_{7/2})$  and  $J^\pi = 13/2^- ((\pi f_{7/2})^2_{4+} \otimes \nu f_{7/2})$  states.

Compared with E2 transitions, E4 multipolarity transitions are poorly understood, despite being a vital source of information in nuclear structure studies [Wil85]. The E2 strengths for even-even nuclei in the sd shell from  $A = 20 - 36$  show little sensitivity to the individual nucleus [Wil85]. E4 strengths, however, present a different case where the nature of these transitions can change dramatically from nucleus to nucleus [Wil85]. Shown in Table 5.3 are theoretical  $2^+ \rightarrow 0^+$  and  $4^+ \rightarrow 0^+$  transition strengths calculated by Jaqaman and Zamick for a number of nuclei in the sd and pf shells, along with the experimental  $\sqrt{B(E2)}$  values [Jaq84].

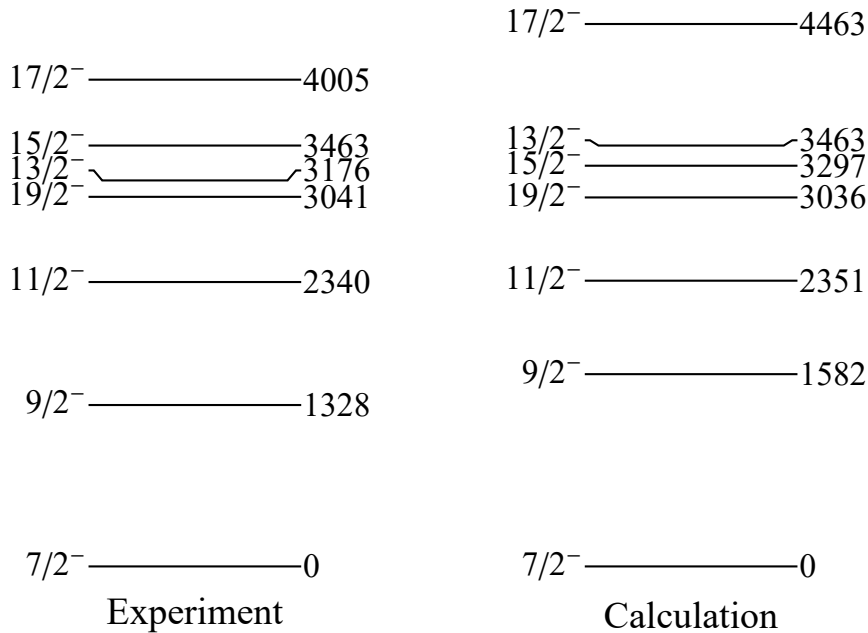


**Figure 5.1:** Comparison of experimental and calculated excited state energies in  $^{53}\text{Fe}$  within the  $f_{7/2}$  model space using the f754 interaction. The high angular momentum transitions in  $^{53}\text{Fe}$  arise from the  $J^\pi = 13/2^-$ ,  $15/2^-$  and  $17/2^-$  states existing above the  $J^\pi = 19/2^-$  state in excitation energy. Experimental states from Ref. [Jun09].

**Table 5.3:** The results of  $2^+ \rightarrow 0^+$  and  $4^+ \rightarrow 0^+$  calculations performed by Jaqaman and Zamick [Jaq84] using the SII interaction. Included for comparison are the experimental strengths they obtained from Refs. [End79, Bro80, DL81, Lig83, Bro80].

Nucleus	$\sqrt{B(E2)}$ (e fm $^2$ )	$\sqrt{B(E4)}$ (e fm $^4$ )		
	Theory	Expt.	Theory	Expt.
$^{20}\text{Ne}$	14.5	17.1(11)	150	195(21)
$^{24}\text{Mg}$	19.2	20.7(2)	68	45(3)
$^{28}\text{Si}$	18.9	18.1(3)	130	164(15)
$^{32}\text{S}$	17.0	17.3(3)	28	145
$^{36}\text{Ar}$	15.5	17.3(8)	31	
$^{48}\text{Cr}$	37.2		470	
$^{50}\text{Cr}$	34.4	34.6(12)	320	235(24)
$^{52}\text{Cr}$	24.6	25.9(14)	250	269(24)
$^{52}\text{Fe}$	33.7		70	

**Table 5.4:** Table of experimental E4 transition strengths compared to theoretical calculations performed by Gadea et al [Gad05] for a number of interactions using the fp model space.

Nucleus	$J_i \rightarrow J_f$	B(E4) (W.u)			
		Exp	FPD6	KB3G	GXPF1
$^{44}\text{Sc}$	$6^+ \rightarrow 2^+$	1.42	1.96	1.79	1.65
$^{46}\text{Ti}$	$4^+ \rightarrow 0^+$	1.60	10.7	7.9	7.39
$^{52}\text{Mn}$	$2^+ \rightarrow 6^+$	0.138	0.272	0.422	0.728
$^{52}\text{Fe}$	$12^+ \rightarrow 8_1^+$	$4.6(17) \times 10^{-4}$	$2.4 \times 10^{-3}$	$3.3 \times 10^{-1}$	$6.5 \times 10^{-2}$
$^{52}\text{Fe}$	$12^+ \rightarrow 8_2^+$	$3.5(13) \times 10^{-3}$	$4.7 \times 10^{-3}$	$2.6 \times 10^{-2}$	$2.3 \times 10^{-2}$
$^{53}\text{Fe}$	$19/2^- \rightarrow 11/2^-$	0.260	0.151	1.23	0.84
$^{54}\text{Fe}$	$10^+ \rightarrow 6^+$	0.79	1.80	0.98	1.25

The calculated  $\sqrt{B(E2)}$  values generally agree with the experimental results and vary little in magnitude for each of the nuclei. The calculated E4 strengths vary dramatically, with order of magnitude shifts occurring over only a few mass units. Within the sd shell there are no experimentally confirmed E4 transitions; however, moving to the pf shell, this number increases to 7. In  $^{31}\text{P}$ , there are several additional proposed E4  $\gamma$  rays, however, none of these assignments are certain.

Gadea et al [Gad05] performed comprehensive shell-model calculations using three different interactions for all of the known E4 transitions in the fp shell; the results of these calculations are shown in Table 5.4. The FPD6 interaction generally performs better than the KB3G and GXPF1 interactions; however, agreement is poor throughout, in many cases failing to reach even an order of magnitude agreement.

This is particularly the case for the  $12^+ \rightarrow 8_1^+$  transition in  $^{52}\text{Fe}$  where the KB3G and GXPF1 interactions are up to several orders of magnitude larger than the experimental value. It should then come as no surprise that for  $^{53}\text{Fe}$ , the theoretical predictions of the E4 strength are inconsistent with experiment.

Several calculations that considered a number of interactions and valence spaces, have been attempted for the E6 strength in  $^{53m}\text{Fe}$ , see Refs. [Bro17, Bro11, Glo75, Met81, Yok97]. Brown and Gloeckner et al [Bro11, Glo75] considered the interaction of valence particles outside the  $^{40}\text{Ca}$  core, while Metsch et al [Met81] consider the interaction of holes and particle-hole couplings outside of a  $^{56}\text{Ni}$  core. Table 5.5 summarises these results, with the experimental value obtained in the present work also included for comparison. The model spaces considered in these calculations (shown in Table 5.5) dictate the valence orbitals available to the particles and holes; these can be as simple as just allowing valence nucleons in the  $f_{7/2}$  orbitals or can be more complicated pictures where admixtures from other orbitals or even shells may be present.

In most cases the calculated strengths disagree in detail with the experimental result but there is generally an order of magnitude agreement. The conditions upon which agreement could be met have been presented in Refs. [Bro11, Glo75] and are discussed below. The experimental strength is in general retarded with respect to theory, with only the  $(pf)^{13}$  model space using the FDP6 and GPFX1A interactions agreeing. Calculations considering only the  $f_{7/2}$  valence space do a poor job of replicating the E6 transition strength (see, for example, the first two rows of Table 5.5). Incorporating the  $f_{5/2}$  orbital into the model space improves the agreement with experiment, although for the SDI interaction the effect is minor (see the last four rows of Table 5.5). Figure 5.2 obtained from Ref. [Met81] shows the ratio of the theoretical M value to the experimental value from Ref. [Bla75], plotted as a function of the  $f_{5/2}$  admixture. It is immediately obvious that the introduction of a small  $f_{5/2}$  admixture can improve the agreement between theory and experiment. For the KB interaction, the  $(f_{7/2})^{-4}(f_{5/2})^1$  admixture greatly influences the calculated E6 transition strength, while for the SDI interaction there is little difference. Metsch et al explain the different behavior as being due to

**Table 5.5:** Summary of matrix elements given in [Glo75, Bro17, Met81] for a number of different interactions and model spaces. Core polarisations of  $\delta_p(E6) = -0.06$  and  $\delta_n(E6) = 0.52$  were used for all of the calculations. The two calculations using the pf model space use different radii (indicated in the table) for the length parameter (b) in the harmonic oscillator potential.

Model Space	Interaction	$A_p(1 + \delta_p)$ ( $\times 10^3 e \text{ fm}^6$ )	$A_n \delta_n$ ( $\times 10^3 e \text{ fm}^6$ )	M ( $\times 10^3 e^2 \text{ fm}^6$ )	B(E6) ( $\times 10^6 e^2 \text{ fm}^{12}$ )
$(f_{7/2})^{13}$	F754 <sup>1</sup>	6.06	0.10	6.16	1.90
	SDI <sup>2</sup>	6.03	0.21	6.24	1.95
$(f_{7/2})^{13} + (f_{7/2})^{12}, (f_{5/2})$	SDI <sup>2</sup>	5.51	0.35	5.86	1.72
	$(\text{pf})^{13}$ ( $b = 1.977 \text{ fm}$ )	KB3G <sup>1</sup>	3.84	0.17	4.01
		GPFX1A <sup>1</sup>	3.63	0.10	3.73
		FPD6 <sup>1</sup>	3.09	0.12	3.21
$(\text{pf})^{13}$ ( $b = 1.90(10) \text{ fm}$ )	KB3G <sup>1</sup>	3.0(9)	0.13	3.1(9)	0.48(14)
	GPFX1A <sup>1</sup>	2.8(8)	0.08	2.9(9)	
	FPD6 <sup>1</sup>	2.35(8)	0.10	2.4(8)	
$(f_{7/2})^{-3}$	SDI <sup>3</sup>	4.55	0.00	4.55	1.03
	KB <sup>3</sup>	4.71	0.00	4.71	1.11
$(f_{7/2})^{-4}(f_{5/2})^1$	SDI <sup>3</sup>	4.45	0.00	4.45	1.01
	KB <sup>3</sup>	3.67	0.00	3.67	0.67
Experiment			2.3(10)	0.28(3)	

<sup>1</sup>See Ref. [Bro11].

<sup>2</sup>See Ref. [Glo75].

<sup>3</sup>See Ref. [Met81].

the smaller destructive contribution from the  $(f_{7/2})^{-4}(f_{5/2})^1$  component in SDI compared to KB, arising from the difference in seniority of the  $(f_{7/2})^3, J^\pi=7/2^-$  state for each interaction [Met81].

In Table 5.5, values of  $\delta_p(E6) = -0.06$  and  $\delta_n(E6) = 0.52$  were used in the calculation of  $A_p(1 + \delta_p)$  and  $A_n\delta_n$ . These values were selected based on calculations performed by H. Sagawa [Sag79] for the core-polarization charge of E2, E4 and E6 transitions in the vicinity of  $^{40}\text{Ca}$ . Recent experiments [Rie05] yielded E2 core polarisation charges consistent with Sagawa; hence the use of a negative value of  $\delta_p$  for the calculation of the E6 strength is not without justification. Gloeckner and Lawson conclude that, for the  $(pf)^{13}$  model space, a core polarisation charge of  $\delta_p(E6) \approx -0.5$  [Glo75] would be required to reproduce the experimental strength. Brown goes further to suggest that, based on the successful E4 strength calculations using the FDP6 interaction in Ref. [Gad05], one can take the range of  $A_p$  in the  $(pf)^{13}$  ( $b = 1.90(10)$  fm) model space to arrive at an average of  $A_p = 3.7(4) \times 10^3 e \text{ fm}^6$ , with the uncertainty taken as the standard deviation of the  $A_p$  values. In turn, this implies  $\delta_p(E6) = -0.35(10)$  to successfully reproduce the experimental E6 transition strength [Bro11]. These results are consistent with the conclusions of Yokoyama [Yok97] who argues that large, negative core-polarizations are necessary to reproduce the severely retarded strength of the high-multipolarity transitions depopulating the  $J^\pi = 19/2^-$  isomer.

That the theoretical interpretation should fail to accurately reproduce the experimental transition strength is perhaps unsurprising, since across the nuclear chart, the study of higher multipolarity transitions is scant with no model or interaction capable of correctly describing their behavior. As is the case for E4 transitions, where there are many more experimental observations to discuss, a good reproduction is not achieved. It should come as no surprise that the same theory struggles to account for the only known E6 transition. This being said, the studies and publications attempted above have all arrived at similar conclusions as to the physics of the situation. Cross shell effects and mixing have a noticeable effect on the calculated transition strengths for these high-multipolarity transitions, indicating the necessity of their inclusion in any shell model calculation of this kind (see

Gloeckner and Lawson [Glo75] and Metsch and Glaudemans [Met81]). The E6 transition itself is only allowed (from the available valence spaces) to proceed via a  $f_{7/2} \rightarrow f_{7/2}$  or  $f_{7/2} \rightarrow f_{5/2}$  particle transition. Gloeckner computed the E6 strength as a function of the  $f_{7/2} - f_{5/2}$  energy gap; the theoretical strength agreed with the experimental strength when the energy splitting was lower and hence, excitation more readily across the orbitals was possible [Glo75].

The 1713-keV, M5 transition behaves similarly to known M4 transitions [Gol51, Kra87], that is, the experimental transition rate is well reproduced by Weisskopf estimates with a measured strength of 3.6(2) W.u. Calculations of the M5 transition strength were attempted in Refs. [Met81, Yok97] with mixed results. Yokoyama's calculations produce a range of values, some of which agree with the experimental result, although considering there is only one data point, this could simply be coincidence. For the most part, an order of magnitude agreement is achieved by Yokoyama, however the calculation considering only the (pf)<sup>13</sup> model space fails completely in this respect [Yok97]. No calculations of the potential M5 transitions in <sup>31</sup>P were attempted. Metsch's work [Met81] offers the same conclusion for the M5 transition as for the E4 and E6 transitions: admixtures with the  $f_{5/2}$  orbital are required to bring the theoretical strength in line with experiment. This is also illustrated in Figure 5.2 [Met81].

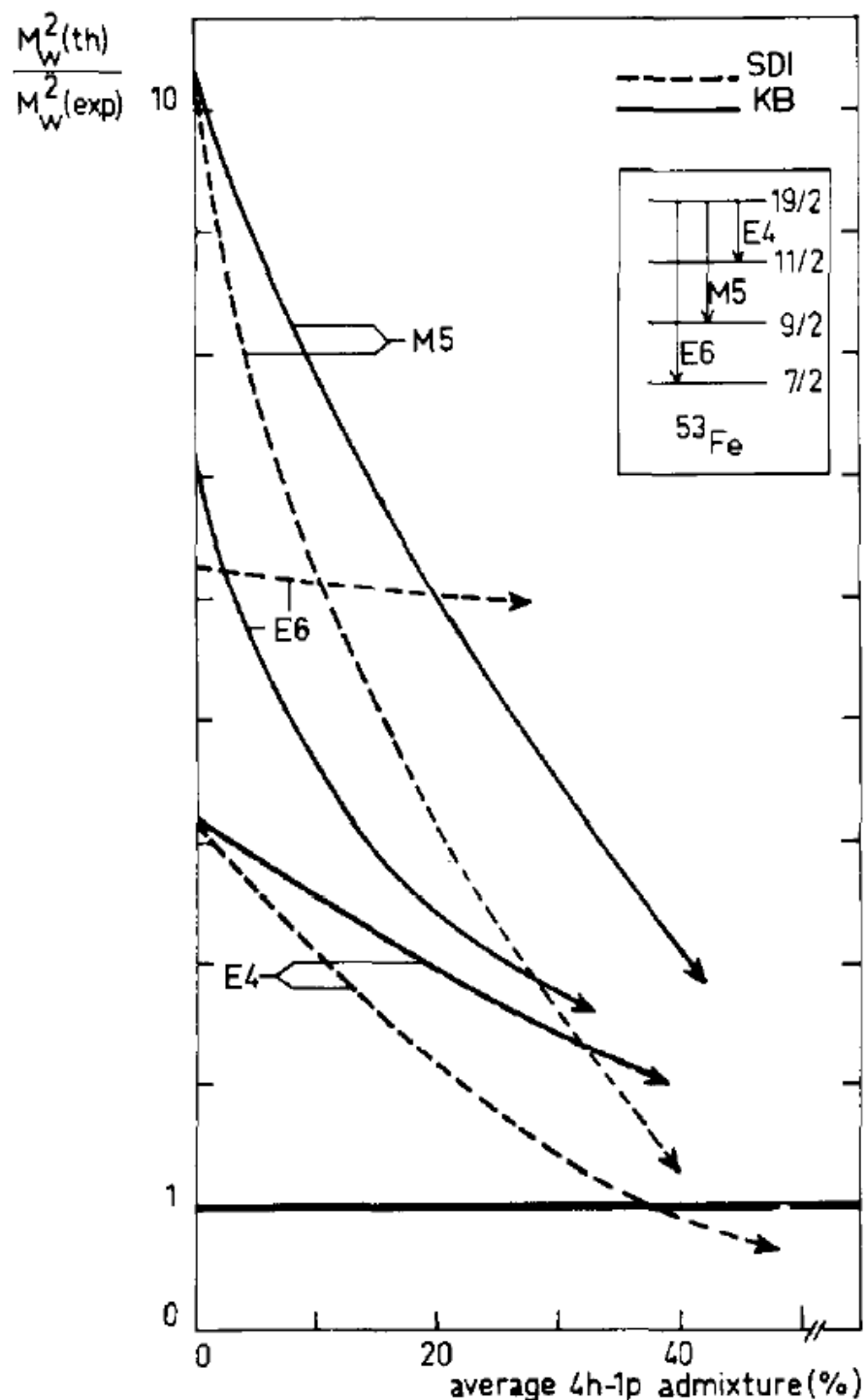


**Figure 5.2:** The effect of increasing the  $(f_{7/2})^{-4}(f_{5/2})^1$  admixture on the ratio of the theoretical and experimental transition strengths for transitions depopulating the  $19/2^-$  state in  $^{53\text{m}}\text{Fe}$ . Figure taken from Ref. [Met81].

# 6

## Chapter 6

## Conclusions and future

## outlook

---

This thesis has presented a comprehensive investigation of the E6 transition in  $^{53m}\text{Fe}$ , and the results of this work serve as compelling evidence for confirmation of its existence. Experimental results, through the development of multiple methods for assessing the sum-coincidence proportion of the peak, all suggest a real E6 component. Monte Carlo simulations reproduce this conclusion, with the intensity of the transition being inexplicable with sum-coincidence events alone. The transition strengths of the  $J^\pi = 19/2^-$  state have been calculated from the newly measured branching ratios and have been interpreted in the context of numerous theoretical calculations performed in the literature. Highlighted in these calculations is the need for cross-shell mixing between the  $f_{7/2}$  and  $f_{5/2}$  orbitals to explain the experimentally observed strength. Additionally, multiple works regard the retarded transition rates of the E4, M5 and E6 transitions as strong evidence for negative core polarisation charges for these high-angular momentum transitions. High-multipolarity transitions appear to be an important tool in understanding

nuclear structure as they are more sensitive to higher-order changes in nucleus than the common  $B(E2; 2^+ \rightarrow 0^+)$  metric which is strongly affected by quadrupole collectivity. A detailed experimental study of sd and fp nuclei could give great insight into E4 decays and thus, nuclei in these regions, where theoretical works are extensive but experimental insight is lacking.

# Appendices

---

# A

## J624 operation

---

The J624 can be used to time-stamp ADC data over a large number of time periods using the settings included on the module by default. The full range of time spectrum widths is shown in Table A.1. These represent the theoretical best performance of the module, however electronic jitter will, in principle, reduce this precision. The module may instead be driven by an external clock which allows the use of time windows of arbitrary size. The full time spectrum width (SW) is then given by

$$SW = \frac{CS \times 8192}{2\nu}, \quad (\text{A.1})$$

where CS is the clock setting in seconds and  $\nu$  is the frequency setting in kHz on the module.

In this work, the reset pulse was delivered by the computer control system on the 14UD accelerator control panel through the use of a script (shown below as pseudo code) that also controlled the Faraday cups to stop and start the beam. A jitter on the order of 100s of milliseconds was expected using this method, however the minute time scales in this work make this a negligible uncertainty.

Control Script:

- 
- Take Faraday cup out at the beam-line;
  - Sleep 7.5 minutes (while the target is irradiated);
  - Put Faraday cup in at the beam-line;
  - Sleep 2 seconds;
  - Start data acquisition;
  - Sleep 20 minutes (while decay of  $^{53m}\text{Fe}$  is measured);
  - Stop data acquisition;
  - Sleep 2 seconds;
  - Send reset pulse to J624;
  - Repeat until stop command is given.

Small sleeps of 2 seconds are used to allow the short-lived activity to decay away and to accommodate delays with the data acquisition starting and stopping; this allows only the out-of-beam decay to be present in the data.

**Table A.1:** Possible time windows produced using the default J624 clock settings and clock frequencies.

Clock Frequency (kHz)	Full spectrum time width (8192 ch)				
	Clock Setting				
	2 ms	20 ms	200 ms	2 s	20 s
8000	0.00102	0.010239	0.102388	1.024	10.239
4000	0.00205	0.020478	0.204775	2.048	20.478
2000	0.0041	0.040955	0.40955	4.096	40.955
1000	0.00819	0.08191	0.8191	8.191	81.91
500	0.01638	0.16382	1.6382	16.38	163.82
250	0.03276	0.32764	3.2764	32.76	327.64
125	0.06553	0.65528	6.5528	65.53	655.28
62.5	0.13106	1.31056	13.1056	131.1	1310.6
31.25	0.26211	2.62112	26.2112	262.1	2621.1
15.625	0.52422	5.24224	52.4224	524.2	5242.2
7.8125	1.04845	10.48448	104.8448	1048	10484
3.90625	2.0969	20.96896	209.6896	2097	20969

# B

## Raw experimental values

---

**Table B.1:** Raw experimental peak areas for the far geometry as measured in the three moveable detectors. The total detection efficiency at that energy is also included for reference.

$E_\gamma$	Peak Area (counts)	Efficiency (%)
701	663904±845	0.65±0.02
1012	420409±754	0.51±0.02
1328	365511±737	0.43±0.01
1713	6059±140	0.35±0.01
2029	589±65	N/A
2340	87489±329	0.277±0.009
3041	387±22	0.225±0.007

---

**Table B.2:** Raw experimental peak areas for the close geometry as measured in the three moveable detectors. The total detection efficiency at that energy is also included for reference.

$E_\gamma$	Peak Area (counts)	Efficiency (%)
701	931961±1002	0.91±0.04
1012	578904±761	0.72±0.04
1328	502143±720	0.60±0.03
1713	4243±89	0.49±0.02
2029	310±49	N/A
2340	66080±228	0.39±0.02
3041	234±16	0.31±0.02

# C

## A method for correcting the sulfur-magnesium transition intensities

---

This appendix will further illustrate some of the problems with the sulfur-magnesium data and derive a method for correcting the large  $\Gamma_E$  values (see Section 3.3) and transition intensities measured in this data set. As an exercise, the same correction method will be employed on the May lithium-vanadium data and the December sulfur-magnesium data. The values presented here do not have any bearing on the branching ratios and intensities obtained in the preceding chapters; this is purely an academic exercise.

As alluded to in prior chapters, detectors at forward angles appear to be counting at rates greater than their efficiency would imply. In Figure C.1, the peak areas of the 701-, 1012-, 1328, and 2340-keV peaks are plotted for each detector as a function of efficiency for the sulfur-magnesium (far) measurement. The red line through the center of the plot shows the expected number of counts for a given detector efficiency based on the total number of decay events in the data set. Unsurprisingly, given the discussion in Section 3.3, the detectors at forward

Peak	1	2	3	4	5	6	7	8	9
701	1.124	1.221	0.943	1.207	1.174	0.673	0.858	1.150	0.819
1012	1.195	1.299	0.860	1.293	1.279	0.629	0.831	1.169	0.808
1328	1.268	1.342	0.809	1.347	1.350	0.604	0.820	1.178	0.804
1713	1.281	1.384	0.754	1.342	1.361	0.575	0.854	1.199	0.817
2340	1.318	1.423	0.764	1.437	1.430	0.563	0.806	1.203	0.793
3041	1.407	1.147	0.709	1.310	1.570	0.500	0.845	1.219	1.091

**Table C.1:** Redistribution coefficients for the sulfur-magnesium experiment in the far geometry. Detectors are numbered one through nine.

Peak	1	2	3	4	5	6	7	8	9
701	1.049	1.016	1.019	0.971	1.007	0.884	1.015	1.017	0.974
1012	1.089	1.041	1.041	1.023	1.062	0.919	1.047	1.051	1.023
1328	1.077	1.005	0.981	0.977	1.039	0.887	0.996	1.016	0.990
1713	1.351	1.015	0.877	0.928	1.189	0.829	0.919	1.048	1.015
2340	1.086	0.995	0.983	0.986	1.044	0.845	1.003	1.024	0.963
3041	0.914	0.902	0.932	0.864	0.920	0.756	0.699	0.724	0.885

**Table C.2:** Redistribution coefficients for the lithium-vanadium experiment in the close geometry. Detectors are numbered one through nine. The coefficients in this data set are all close to one (c.f Table C.1) indicating that the decay measured by each detector was in line with its expected proportion.

angles sit well above the expected number of counts. Figure C.2 shows the same analysis for the 1328-keV transition in the lithium-vanadium (close) experiment. The contrast between the lithium-vanadium and sulfur-magnesium plots is striking. In the sulfur-magnesium experiments, where large  $\Gamma_E$  values were measured, significant deviations from the expected count rate are present, while, in the lithium-vanadium plot, each detector is counting close to its expected number of events. By considering the ratio of the expected counts to the measured counts (redistribution coefficient), the decay measured in each detector may be normalised to the expected value, i.e, the points may be shifted onto the red line. However, this scaling will not remove the  $\Gamma_E$  imbalances present in the data as it is simply redistributing the decay among the detectors, the surplus of events in each decay peak will still be present. Tables C.1 and C.2 show the redistribution coefficients for the sulfur-magnesium (far) experiment and the lithium-vanadium (close) experiment; note that a much lower level of redistribution is required for the lithium vanadium experiments.

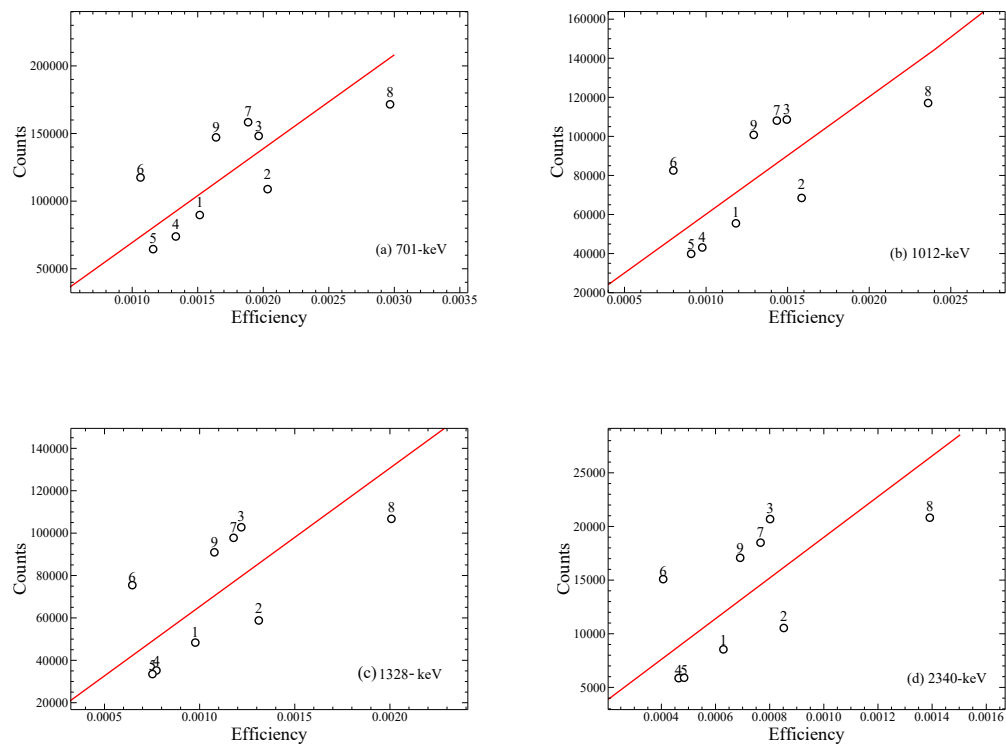


**Figure C.1:** Number of counts recorded in each peak labeled (a) to (d) for the (far geometry) sulfur-magnesium experiment. The red line indicates the expected number of counts based on each detectors efficiency. The redistribution coefficients discussed in the text are used to scale each detector to this red line.

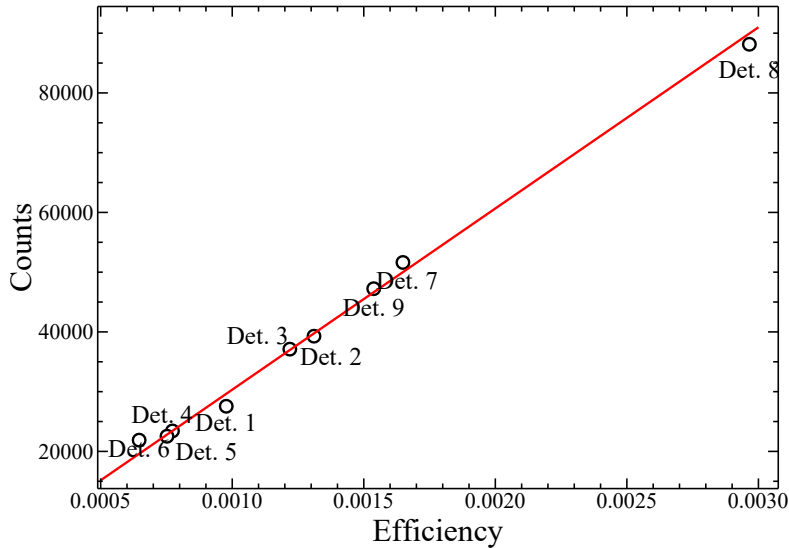


**Figure C.2:** Number of counts in each peak plotted against the efficiency of each detector for the lithium-vanadium (close) data. The red line through the plot indicates the expected number of counts for each detector.

In order to remove the surplus events from the total data set, an additional scaling factor must be used to filter out the unbalanced events. Such a scaling factor needs to be different for each transition as the degree of over-intensity differs for each transition. Numerous attempts were made at finding a scaling factor capable of producing this effect. The most successful attempt involved a subsequent scaling of each redistribution coefficient, relative to the redistribution coefficients for detectors with balanced  $\Gamma_E$  values. Define:

$$\delta_{E,d} = \frac{\mu_{E,d}}{\langle \mu_{E,d'} \rangle} \quad (C.1)$$

with  $\mu_{E,d'}$  denoting the redistribution coefficient of a detector ( $d$ ) at a peak energy ( $E$ ). The term in the denominator denotes a weighted average over the redistribution coefficients of the detectors being used to scale the decay. This factor is able to remove surplus decay because, as shown in Table C.1, the coefficients for detectors with a deficit of events are similar in value, while those presenting a surplus of

Peak	1	2	3	4	5	6	7	8	9
701	0.978	1.062	0.820	1.050	1.021	0.585	0.747	1.000	0.713
1012	0.965	1.049	0.694	1.044	1.033	0.508	0.671	0.944	0.652
1328	0.968	1.025	0.617	1.028	1.030	0.461	0.626	0.899	0.614
1713	0.969	1.047	0.571	1.015	1.029	0.435	0.646	0.907	0.618
2340	0.958	1.034	0.555	1.044	1.039	0.409	0.586	0.874	0.577
3041	0.942	0.768	0.475	0.878	1.052	0.335	0.566	0.816	0.731

**Table C.3:** Scaled redistribution coefficients for the sulfur-magnesium experiment in the far geometry as described in the text.

events are significantly different. By dividing each redistribution coefficient by say, the weighted average of Detectors 1 and 5, Detectors 1, 2, 4, 5, and 8 will be shifted towards 1 (little to no redistribution), while Detectors 3, 6, 7 and 9 will be shifted much further from 1. This factor will scale out surplus events while still redistributing the decay so that the expected proportion is equal to the measured proportion. The scaled redistribution coefficients for the sulfur-magnesium (far) experiment are shown in table C.3. Applying this scaling still moves every point to the expected count line while also managing to scale out the surplus events (Figure C.3), reducing  $\Gamma_{1328} = 1.058(18)$  to  $\Gamma_{1328'} = 1.002(3)$  for the sulfur-magnesium (far) data. The scaled intensities for each experiment are shown in Table C.4, with the values between each experiment all now agreeing with each other.

While this method appears to work, it relies on the choice of detectors used to scale the redistribution coefficients. In this case, a justification for the choice of detectors can be made: low efficiency, backward angle detectors are the least affected by neutron damage. However, the selection of detectors would be impossible to do without some selective bias the results. After countless hours it was concluded that resolving the differences between the sulfur-magnesium data and the lithium-vanadium data would be impossible and that the former data should be discarded in favour of the balanced lithium-vanadium data. In future, experiments at HIAF should carefully weigh the pursuit of high detector count rates versus the potential for neutron damage to the detectors and the consequent collection of poor-quality data with incorrect statistics.

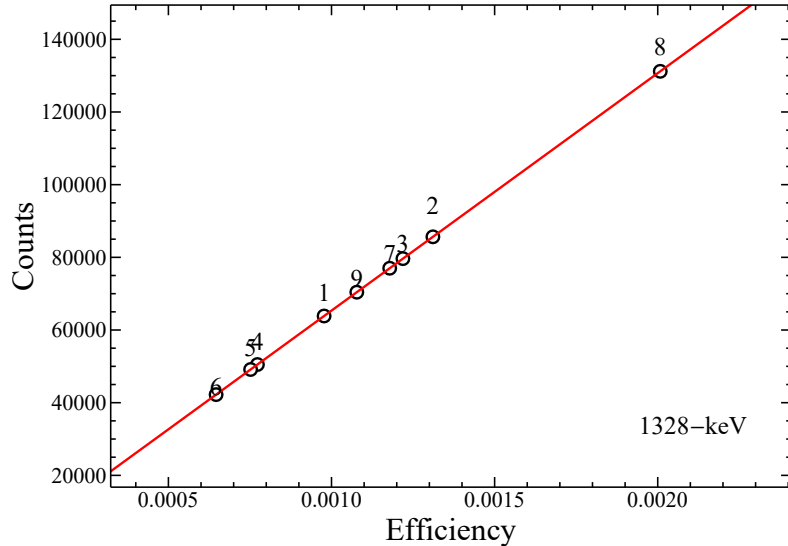


**Figure C.3:** Number of counts in 1328-keV peak following the application of scaled-redistribution coefficients to the sulfur-magnesium (far) data.

Peak	Vanadium (May)		Intensity		Sulfur (Dec)	Literature
	Close	Far	Sulfur (May)	Sulfur (Dec)	Dets. 1-6	
701	1000	1000	1000	1000	1000	1000
1012	786(22)	781(27)	784(14)	788(17)	791(28)	860.0
1328	804(22)	793(28)	804(15)	801(18)	807(29)	870.2
1713	12.1(3)	10.9(3)	11.7(2)	12.2(3)	12.6(4)	13.2
2340	215(13)	213(15)	214(9)	220(10)	205(16)	129.8
3041	1.02(9)	0.88(9)	1.12(7)	0.95(7)	1.03(15)	0.6

**Table C.4:** Intensity of  $\gamma$ -rays emitted in the decay of the  $19/2^-$  isomer in  $^{53}\text{Fe}$  normalised to 1000 counts in the 701-keV peak. These intensities incorporate the sum-component of the 1713-, 2340- and 3041-keV peaks and are reported as measured in the 3 moveable detectors (7, 8 and 9) for the May experiments. This is the same as Table 3.2 in Chapter 3, except the values have been rescaled according to the method described in the text in this appendix.

# Paper: High-spin spectroscopy and shell-model interpretation of the $N < 126$ radium isotopes $^{212}\text{Ra}$ and $^{213}\text{Ra}$

---

Though not related to the present work, the content of the following paper was produced parallel to the present work and constituted a significant effort throughout this degree. It has been submitted for publication in Physical Review C.

# High-spin spectroscopy and shell-model interpretation of the $N < 126$ radium isotopes $^{212}\text{Ra}$ and $^{213}\text{Ra}$

T. Palazzo, G. J. Lane, A. E. Stuchbery, A. J. Mitchell, A. Akber,  
M. S. M. Gerathy, S. S. Hota, T. Kibédi, B. Q. Lee, N. Palalani, and M. W. Reed  
*Department of Nuclear Physics, Research School of Physics and Engineering,  
The Australian National University, Canberra, ACT 2601, Australia*

The level structures of  $^{212}\text{Ra}$  and  $^{213}\text{Ra}$  have been established via time-correlated  $\gamma$ -ray spectroscopy following the  $^{204}\text{Pb}(^{12}\text{C}, 4n)^{212}\text{Ra}$  and  $^{204}\text{Pb}(^{13}\text{C}, 4n)^{213}\text{Ra}$  reactions. In  $^{212}\text{Ra}$ , levels up to  $\sim 6.2$  MeV were identified and firm spin-parity assignments were achieved to a  $J^\pi = 19^+$  isomer with a mean life of  $31(3)$  ns. For  $^{213}\text{Ra}$  the corresponding values were  $\sim 4.5$  MeV in excitation energy and  $J^\pi = 33/2^+$ . Two isomeric states with  $J^\pi = 23/2^+$ ,  $\tau = 27(3)$  ns and  $J^\pi = 33/2^+$ ,  $\tau = 50(3)$  ns were discovered in  $^{213}\text{Ra}$ . The experimental data are compared with semiempirical shell-model calculations, which allowed dominant configurations to be assigned to most of the observed levels.

## I. INTRODUCTION

The nuclear shell model [1] is the foundation on which much of our understanding of atomic nuclei has been built. Nuclei in the vicinity of doubly magic  $^{208}\text{Pb}$  ( $Z = 82$ ,  $N = 126$ ) provide an important testing ground for the validity of the shell model. More recently they have served as a benchmark for studies of the shell structure around neutron-rich  $^{132}\text{Sn}$ , which has become experimentally accessible through advances in experimental capabilities with radioactive ion beams [2, 3]. In this paper we focus on the radium isotopes ( $Z = 88$ ) below  $N = 126$ , namely  $^{213}\text{Ra}$  ( $N = 125$ ) and  $^{212}\text{Ra}$  ( $N = 124$ ). The shell model approach has proved to be applicable to the  $N = 126$  isotones above  $Z = 82$ :  $^{210}\text{Po}$  ( $Z = 84$ ) [4],  $^{211}\text{At}$  ( $Z = 85$ ) [5],  $^{212}\text{Rn}$  ( $Z = 86$ ) [6],  $^{213}\text{Fr}$  ( $Z = 87$ ) [7] and  $^{214}\text{Ra}$  ( $Z = 88$ ) [8], at least to moderate spins. Lifetime measurements and the resulting  $B(E2)$  values obtained for the radium isotopes with  $N > 126$  suggest a smooth increase in collectivity as the number of valence neutrons increases [9–11]. Knowledge of the radium isotopes near but below  $N = 126$ , particularly  $^{213}\text{Ra}$  and  $^{212}\text{Ra}$ , is more limited. Technical challenges associated with measuring time correlated  $\gamma$ -ray coincidences across long-lived isomeric states, along with low production cross sections and strong fission competition, have hindered spectroscopic studies of these nuclei to higher spins. Prior knowledge of the decay scheme of  $^{213}\text{Ra}$  has been limited to a single cascade of three  $\gamma$ -ray transitions below a  $J^\pi = 17/2^-$ ,  $\tau = 3\text{-ms}$  isomer [12]. Spectroscopic data on the neighbouring isotope,  $^{212}\text{Ra}$ , is more extensive, but achieves firm spin assignments only to  $J^\pi = 13^-$  [13].

Here we report on the experimental extension of the level schemes of  $^{213}\text{Ra}$  and  $^{212}\text{Ra}$  up to  $J^\pi = 33/2^+$  and  $J^\pi = 19^+$ , respectively. The new level schemes are considered within a semiempirical shell-model framework, which allows the assignment of the dominant configuration to many of the observed states. Limitations of the calculations as additional nucleons are added to the valence space are also discussed.

## II. EXPERIMENTAL DETAILS

Excited states in  $^{213}\text{Ra}$  and  $^{212}\text{Ra}$  were populated via the  $^{204}\text{Pb}(^{13}\text{C}, 4n)^{213}\text{Ra}$  and  $^{204}\text{Pb}(^{12}\text{C}, 4n)^{212}\text{Ra}$  reactions, with beam energies of 80 MeV and 81 MeV, respectively. The  $^{12,13}\text{C}$  beams were delivered by the 14UD accelerator of the Heavy Ion Accelerator Facility at the Australian National University and pulsed to  $\sim 1$  ns in width separated by 1712 ns. The target was isotopically enriched  $^{204}\text{Pb}$  (99.6%), 5.4-mg/cm<sup>2</sup> thick.

Prompt (in-beam) and delayed (out-of-beam) emission of  $\gamma$  rays was measured using the CAESAR array of Compton-suppressed, high-purity germanium (HPGe) detectors. CAESAR consists of nine HPGe detectors in a close-packed geometry, six of which are positioned in pairs perpendicular to the beam axis in the vertical plane at angles of  $\pm 34^\circ$ ,  $\pm 48^\circ$  and  $\pm 82^\circ$ . Three HPGe detectors, in addition to two unsuppressed, low-energy-photon spectrometers (LEPS), were positioned approximately in the horizontal plane. Time-correlated  $\gamma - \gamma$  coincidence data were collected in list mode. The HPGe and LEPS detectors were calibrated to 0.5-keV and 0.2-keV per channel, respectively.

Angular anisotropies were measured via  $\gamma - \gamma$  coincidence data sorted into two-dimensional matrices, with pairs of detectors at equivalent angles of  $\pm 34^\circ$ ,  $\pm 48^\circ$  and  $\pm 82^\circ$  recorded on one axis and any measured, coincident  $\gamma$  ray in the remaining eight HPGe detectors placed on the other axis. Since only three angle pairs were available, the  $A_4$  coefficient was fixed to zero when fitting the measured angular data with the usual expansion in even-order Legendre polynomials. Extracted  $A_2$  values still serve as a guide to determine transition multipolarities; however, the limited angle coverage and need to set  $A_4 = 0$  meant that precise transition mixing ratios could not be determined. For the angular momentum alignment expected in heavy-ion fusion-evaporation reactions, and with coincidence gates placed on known  $E2$  transitions, pure dipole, quadrupole or octupole transitions typically exhibit an  $A_2/A_0$  value of  $-0.2$ ,  $+0.28$  or  $+0.46$ , respectively. In some cases, it was possible to

make definitive transition-multipolarity assignments by determining the internal conversion coefficients from  $\gamma$ -ray intensity balances and comparison with theoretical values [14]. Since the probability for internal conversion decreases significantly with increasing transition energy, this method was only applicable to low-energy transitions.

Isomeric-level lifetime measurements were made by observing the time of arrival of  $\gamma$  rays with respect to the beam pulse, or by evaluation of the time difference between  $\gamma$  rays feeding and depopulating the state of interest. In the former case, all levels populated following the  $\gamma$  decay of an isomeric state exhibit that lifetime, thereby inhibiting the measurement of shorter-lived isomers located below the long-lived states. Through complementary application of the  $\gamma\gamma$  time-difference method, it has been possible to isolate shorter-lived states, albeit with reduced counting statistics.

### III. RESULTS

Evidence and justification for the proposed  $^{213}\text{Ra}$  and  $^{212}\text{Ra}$  level schemes, which extend the previous work [12, 13], are provided below. Inspection of  $\gamma$ -ray spectra recorded both ‘in-beam’ ( $-13$  ns to  $+30$  ns around the beam pulse) and in various ‘out-of-beam’ ( $+30$  ns to  $+1700$  ns after the beam pulse) gates were used to identify previously unknown, high-spin isomers in both isotopes. Characteristics of these new excited states and transitions are provided in Tables I, II and III. The proposed level schemes are presented in Fig. 1 and Fig. 2. All levels located above the  $J^\pi = 17/2^-$  isomer in  $^{213}\text{Ra}$ , and most of the levels above the  $J^\pi = 11^-$  isomer in  $^{212}\text{Ra}$ , have been identified for the first time.

#### A. $^{213}\text{Ra}$ level scheme

Prior knowledge [12] of the  $^{213}\text{Ra}$  level scheme was limited to a cascade of three  $E2$   $\gamma$ -ray transitions connecting the yrast  $J^\pi = 13/2^-$  level to the  $J^\pi = 1/2^-$  ground state, and evidence for an unobserved transition with energy of less than 10 keV [12] between the  $J^\pi = 13/2^-$  state and the  $J^\pi = 17/2^-, \tau = 3\text{-ms}$  isomer. Observation of transitions below the  $J^\pi = 17/2^-$  isomer confirmed the production of  $^{213}\text{Ra}$  in the experiment, however, the 3-ms lifetime of the isomer precluded direct correlation of any observed transitions arising from above this state with the known level structure lying below. Nevertheless,  $\gamma$ -ray coincidences with characteristic radium X rays [15], and prior knowledge of the neighbouring radium isotopes [8, 9], enabled unambiguous assignment of many new transitions to  $^{213}\text{Ra}$  located above the  $J^\pi = 17/2^-$  isomer.

The  $\gamma$  rays observed in the in-beam data, and identified to be in coincidence with the 88.47-keV radium  $K_{\alpha 1}$  X ray [15], yielded a number of strong transitions that

had not previously been assigned to any of the radium isotopes. The most intense of these was the 518-keV transition that, based on its intensity, has been assigned to directly feed the  $J^\pi = 17/2^-$  isomer. Background-subtracted, out-of-beam coincidence spectra, gated on the 566-keV, 322-keV and 518-keV transitions, are provided in Fig. 3. The fact that these  $\gamma$  rays are strongly populated in the out-of-beam data provides compelling evidence for the existence of further high-spin isomers in  $^{213}\text{Ra}$ . The coincidence spectrum generated by gating on the 518-keV  $\gamma$ -ray transition contains almost every new transition that is placed in the extended  $^{213}\text{Ra}$  level scheme.

The out-of-beam coincidence spectra, gated on the 566-keV and 322-keV transitions (Figs. 3a and 3b), illustrate the parallel cascades that occur above the 518-keV transition. The ordering of transitions was established unambiguously from a number of crossover transitions. The exceptions are the ordering of the 994–152-keV, and 1058–88-keV cascades. Each of these could, in principle, be reversed. Their ordering was based on the in-beam intensities measured by gating on the 518-keV transition. Further evidence for their ordering was obtained via comparison with the semiempirical shell-model calculations discussed in Section IV, which predict states lying close in energy to those in the proposed level scheme.

The 88-keV transition was observed directly, and resolved from the radium X-rays, by projecting the  $\gamma$  rays detected in the LEPS detectors that were coincident with the 566-keV and 1058-keV transitions detected in the HPGe detectors; it was not observed in gates on the parallel 297–849-keV cascade. LEPS spectra with gates on the 1058-keV and 849-keV transitions are shown in Fig. 4. The meeting point of the two significant parallel cascades (one passing through exclusively positive parity states, the other through predominantly negative parity states) was established by gating on the 518-keV transition. The 437-keV and 538-keV  $\gamma$  rays present in this gate were not in coincidence with the strong 566-keV transition that feeds the  $J^\pi = 29/2^-$  state. The 437-keV  $\gamma$  ray is coincident with both members of the 305–849-keV cascade that feeds the  $J^\pi = 21/2^-$  level. The 538-keV transition was found to be in coincidence with the 731-keV and 322-keV transitions, which feed and depopulate the  $J^\pi = 23/2^+$  isomer. The energy sum of the 437–305–849-keV cascade is equal to the sum of the 538–731–322-keV cascade within uncertainties, which, when combined with the  $\gamma\gamma$  coincidence relationships, supports the placement of a level at  $3878 + \Delta$  keV. The energy sums of the 566–305–849-keV cascade and the 667–731–322-keV cascade are equal within uncertainties, placing a new level linking the two parallel cascades at  $4007 + \Delta$  keV. The 8.2-keV and 14.4-keV transitions are unobserved gaps inferred from energy sums and comparisons between coincidence spectra.

The energy sum of the 170-keV and 437-keV transitions is equal to the energy of the 606-keV transition within uncertainties, suggesting these are parallel cas-

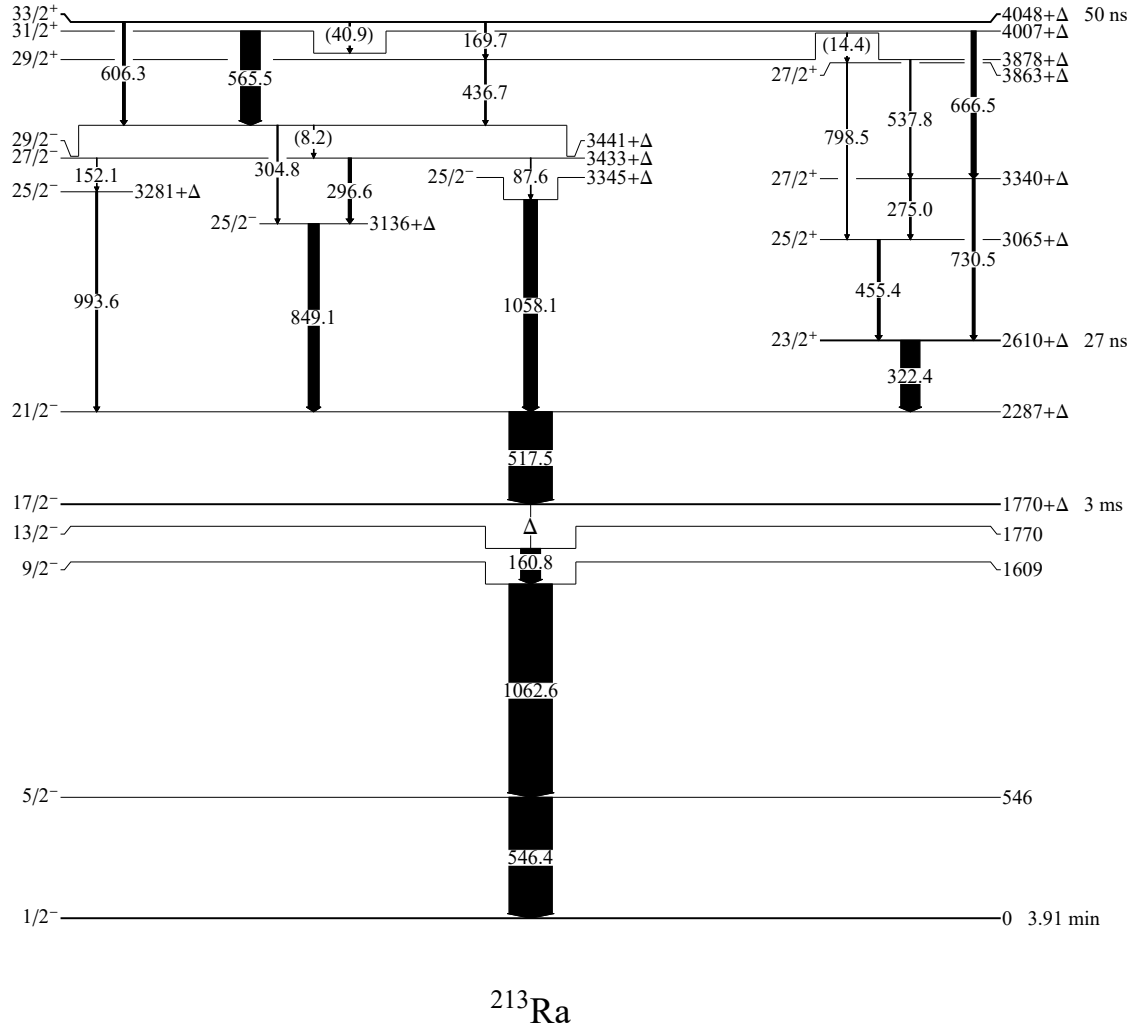


FIG. 1. Level scheme of  $^{213}\text{Ra}$ . All levels located above the  $J^\pi = 17/2^-$  isomer have been identified for the first time. Widths of the arrows indicate  $\gamma$ -ray intensities relative to the 518-keV gating transition feeding the  $J^\pi = 17/2^-$  isomer in the out-of-beam data. Transition widths below the  $J^\pi = 17/2^-$  isomer are based on the measurements in Ref. [12]. The state lifetimes shown are mean lives.

cades de-exciting an additional state located at 4048+ $\Delta$  keV. This state was found to be isomeric and the measurement of its lifetime is discussed below. An unobserved 41-keV transition is placed between the 4048+ $\Delta$ -keV and 4007+ $\Delta$ -keV levels that feeds towards the 566-keV and 667-keV decay sequences that were discussed above. Projecting ‘early’  $\gamma$  rays detected 30 ns to 150 ns prior to the 322-keV, 518-keV and 566-

keV transitions showed an additional, strong 459-keV  $\gamma$  ray that is evidently not emitted following the decay of an isomeric state. This transition is attributed to a level located above the  $J^\pi = 33/2^+$  isomer, possibly at 4507+ $\Delta$  keV. We have not shown the 459-keV line on the level scheme because the semiempirical shell-model calculations strongly suggest that there may be an additional unobserved low-energy transition from a

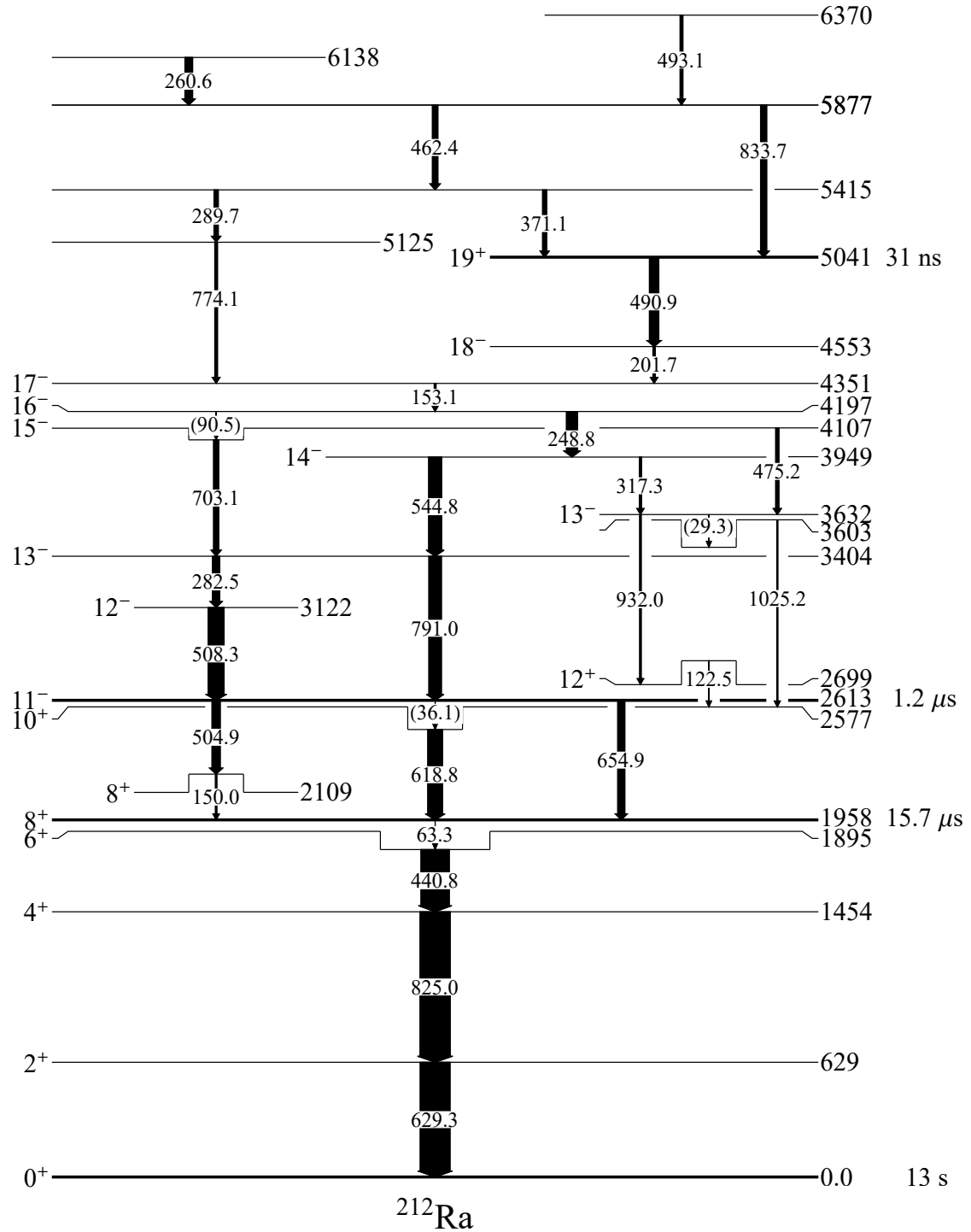


FIG. 2. Level scheme of  $^{212}\text{Ra}$ . Most of the levels above the  $J^\pi = 11^-$  isomer have been identified for the first time. Widths of the arrows indicate relative  $\gamma$ -ray intensities. Transition intensities of the cascade below the  $J^\pi = 8^+$  isomer were determined from a singles spectrum. Relative intensities for transitions occurring between the  $J^\pi = 11^-$  and  $J^\pi = 8^+$  isomers were determined using a sum of gates on the 508-keV and 791-keV transitions. Above the  $J^\pi = 11^-$  isomer, intensities were determined using a sum of gates set on the 505-keV, 619-keV and 655-keV transitions. State lifetimes are given as mean-lives.

$J^\pi = 35/2^+$  state immediately above the  $J^\pi = 33/2^+$  isomer, which could not be either confirmed or excluded. In addition to the 459-keV transition, several transitions (listed in Table II) were observed in-beam in a decay path bypassing the isomer at  $4048+\Delta$  keV. Due to insufficient statistics these transitions could not be confidently placed in the  $^{213}\text{Ra}$  level scheme; however, coincidences with strong  $^{213}\text{Ra}$   $\gamma$  rays confirm their assignment to this nucleus.

## B. $^{212}\text{Ra}$ level scheme

### 1. Transitions below the 4351-keV $J^\pi = 17^-$ state

Background-subtracted, coincidence spectra gated on the 249-keV and 619-keV transitions are provided in Fig. 5. Despite lying below the  $J^\pi = 11^-$  isomer, gating on the 619-keV  $\gamma$  ray isolates transitions that follow the decay of higher-spin isomers populated in the reaction due to the 123-keV decay branch bypassing the isomer. Spectroscopic evidence for new parallel decay cascades located below the state at 4351 keV was obtained by gating on the 317-keV, 545-keV and 703-keV  $\gamma$ -ray transitions in the out-of-beam data, as shown in Fig. 6. The 153-keV  $\gamma$  ray is common to all three spectra, placing a meeting point of these three cascades below this transition. The 249-keV transition is common to the 317-keV and 545-keV gates, identifying a meeting point between these two branches. The placement of a 91-keV gap between the 4198-keV and 4107-keV levels is inferred from the observed coincidence between 703-keV and 153-keV transitions. The energy sums of the 123–932–475–91-keV, 36–791–703–91-keV and 36–791–545–249-keV cascades are equal within the experimental uncertainties, supporting the placement of the unobserved 91-keV gap. The order of transitions can be established unambiguously throughout this section of the level scheme due to the number of intersecting cascades. The only exception is the 283–508-keV cascade, the order of which has been based upon the relative intensities of the two transitions when projecting  $\gamma$ -rays early with respect to the 619-keV  $\gamma$  ray. The gate on the 317-keV transition in Fig. 6a shows a loss of intensity in the 317–932–123-keV and 317–29–1025-keV cascades relative to the 249-keV and 619-keV  $\gamma$ -ray transitions, above and below these sequences. The existence of additional decay paths out of the 3632-keV state is thus implied but, due to poor statistics, no candidate transitions could be identified in the  $\gamma$ -ray spectra.

### 2. Transitions above the 4351-keV $J^\pi = 17^-$ state

An additional ten  $\gamma$ -ray transitions connecting eight excited states above the 4351-keV,  $J^\pi = 17^-$  state have been placed in the  $^{212}\text{Ra}$  level scheme. In-beam coincidence spectra, gated on the 491-keV and 290-keV transitions, are shown in Fig. 7. These serve as evidence of the

parallel cascades located above the 4351-keV level. The 491-keV  $\gamma$  ray is present in both the in-beam and “short” out-of-beam data while the transitions located above it are only identified in the in-beam data, which indicates that the 5041-keV state is isomeric. Measurement of the meanlife of this isomer is discussed below. The placement of excited states located above the 5041-keV isomer is unambiguous; however, the ordering of the 290–774-keV cascade through the proposed 5125-keV state could be reversed.

## C. Conversion Coefficients

Total internal conversion coefficients were deduced from the intensity balance across levels. For instance, in the lower panel of Fig. 3, the measured yield of the 152-keV transition that feeds the  $3281+\Delta$ -keV,  $J^\pi = 25/2^-$  state, would be expected to balance that of the subsequent 994-keV transition that depopulates it. Internal conversion coefficients were extracted for 12 transitions in  $^{212}\text{Ra}$  and  $^{213}\text{Ra}$  from similar considerations. Comparison of the experimental values to theoretical calculations using the BRICC code [14] constrained the multipolarity of the transitions, as illustrated in Fig. 8. In  $^{213}\text{Ra}$ , most conversion coefficients were determined by gating on the 518-keV transition out-of-beam, which gives clean spectra following the decay of the  $4048+\Delta$ -keV,  $J^\pi = 33/2^+$  isomer. In  $^{212}\text{Ra}$ , conversion coefficients were determined by gating on a variety of transitions due to the large number of pathways identified throughout the level scheme.

## D. Angular anisotropies

Measured angular anisotropies provided information on the angular-momentum change due to transitions in  $^{212}\text{Ra}$  and  $^{213}\text{Ra}$ . The  $A_2/A_0$  coefficients extracted from fitting  $W(\theta) = A_0 + A_2 P_2(\cos \theta)$  to the data are listed in Tables I and III. Selected fits to the experimental data are displayed in Fig. 9 and extracted  $A_2/A_0$  coefficients are displayed in Fig. 10. Further physical considerations can facilitate the determination of the electric or magnetic nature of many identified transitions. There is a well-established occurrence of  $E3$  transitions from isomeric states in neighboring nuclides [8, 9, 16]. Consequently, any transitions found to exhibit a large  $A_2/A_0$  coefficient without a discernible state lifetime can be considered to be  $E2$  in nature. As will be discussed in more detail below, low-energy  $E1$  transitions in these nuclei are normally associated with the decay of isomeric levels. Thus, in most cases,  $A_2/A_0$  values indicating a dipole character without a measurable lifetime can be considered to be  $M1$  transitions. Significant deviation of the measured  $A_2/A_0$  coefficients from the expected values can indicate mixed-multipolarity transitions. However, with only three detector angles available and, therefore, no measurement of the corresponding  $A_4$  term, the exact

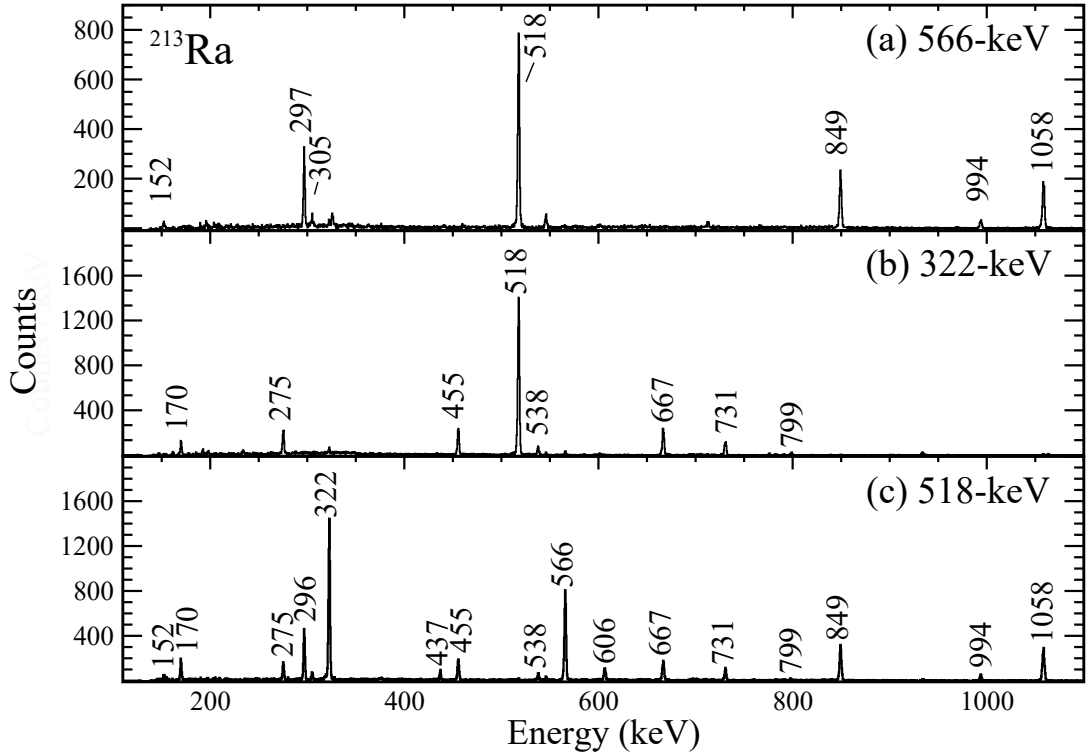


FIG. 3. Background-subtracted, out-of-beam (+30 ns to +140 ns after the beam pulse) coincidence spectra gated on the (a) 566-keV,  $J^\pi = 31/2^+ \rightarrow 29/2^-$ , (b) 322-keV,  $J^\pi = 23/2^+ \rightarrow 21/2^-$  and (c) 518-keV,  $J^\pi = 21/2^- \rightarrow 17/2^-$  transitions in  $^{213}\text{Ra}$ .

mixing ratio cannot be determined. The 297-keV and 455-keV transitions in  $^{213}\text{Ra}$ , and the 508-keV transition in  $^{212}\text{Ra}$  (see Figure 9d) appear to have mixed  $E2/M1$  multipolarity.

#### E. Lifetime measurements

The lifetime of the  $4048 + \Delta$ -keV isomer in  $^{213}\text{Ra}$ , determined from the time difference between the 459-keV transition feeding the isomer and a sum of gates on the 170-keV, 566-keV and 606-keV transitions below the isomer, is  $50(3)$  ns, as shown in Fig. 11. Lifetime measurements with respect to the beam pulse for the 566-keV and 667-keV transitions showed no discernible difference, demonstrating that this choice of gating transitions does not bias the lifetime curve. A similar approach was used to measure the lifetime of the  $2610 + \Delta$ -keV state. The time difference between the 455-keV and 731-keV feeding transitions and the 322-keV decaying transition yields a

lifetime of  $27(3)$  ns.

The  $31(3)$  ns lifetime of the 5041-keV state in  $^{212}\text{Ra}$ , shown in Fig. 12, has been measured with reference to the beam pulse by gating on the 491-keV transition and projecting the resulting time spectrum. An additional time difference measurement was attempted, however, even a sum of many time difference spectra had insufficient statistics. Measurements of the  $J^\pi = 11^-$  state lifetime confirmed the literature value of  $\tau = 1.2(2)$   $\mu\text{s}$  [13], but the maximum beam pulse separation of  $1.7$   $\mu\text{s}$  precluded obtaining an independent result of comparable precision.

#### F. Spin-parity assignments

Spin and parity assignments are known from prior studies up to the  $J^\pi = 17/2^-$  isomer in  $^{213}\text{Ra}$  [18], and to the  $J^\pi = 13^-$  state in  $^{212}\text{Ra}$  [13]. Spins and parities have been assigned to the majority of new states

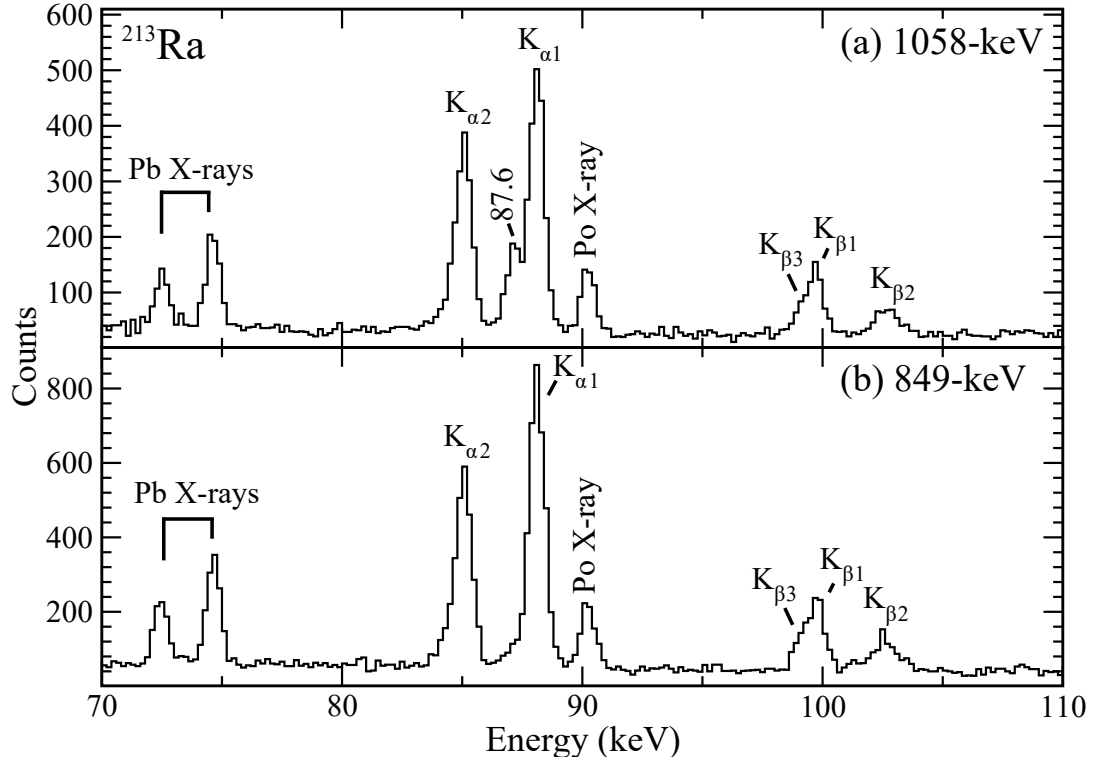


FIG. 4. Background-subtracted, LEPS coincidence spectra for  $^{213}\text{Ra}$ , gated on the (a) 1058-keV,  $J^\pi = 25/2^+ \rightarrow 21/2^-$ , (b) 849-keV,  $J^\pi = 25/2^+ \rightarrow 21/2^-$  transitions in  $^{213}\text{Ra}$  observed in the HPGe detectors. Lines labelled with K designations refer to the radium X-rays, other X-rays from random coincidences are also labeled.

identified in the present work based on a combination of measured internal conversion coefficients, angular anisotropies, and state lifetimes, along with constraints required by crossover transitions.

### 1. Spin-parity assignments in $^{213}\text{Ra}$

The  $2287+\Delta\text{-keV}$  state is assigned as  $J^\pi = 21/2^-$  on the basis that the 518-keV transition connecting this state to the  $J^\pi = 17/2^-$  isomer was determined to be an  $E2$  transition from the measured  $A_2/A_0$  value and lack of a measurable state lifetime. The  $J^\pi = 21/2^-$  state is fed by four  $\gamma$  rays with energies of 322 keV, 849 keV, 994 keV and 1058 keV. The three higher energy transitions are assigned as stretched  $E2$  on the basis of their  $A_2/A_0$  values and the absence of measurable lifetimes for the states that they depopulate. Thus the states at  $3136+\Delta$  keV,  $3281+\Delta$  keV and  $3345+\Delta$  keV are all assigned  $J^\pi = 25/2^-$ . The internal conversion coefficient

of the 152-keV transition supports an  $M1 + E2$  assignment with a mixing ratio of  $|\delta(E2/M1)| = 0.7(3)$ . The 297-keV transition's  $A_2/A_0$  value and its conversion coefficient indicate  $M1$  multipolarity, while the lack of an observable lifetime associated with the 8-keV gap between the  $3433 + \Delta\text{-keV}$  and  $3441 + \Delta\text{-keV}$  states also implies  $M1$  multipolarity. Thus all three  $J^\pi = 25/2^-$  states are fed by a  $J^\pi = 27/2^-$  state at  $3433 + \Delta$  keV, with a  $J^\pi = 29/2^-$  state 8 keV higher at  $3441 + \Delta$  keV. The  $8-152-994\text{-keV}$ ,  $8-297-849\text{-keV}$ , and  $8-88-1058\text{-keV}$  cascades all converge at the  $J^\pi = 29/2^-$ ,  $3441+\Delta\text{-keV}$  state. The 566-keV transition feeding the  $J^\pi = 29/2^-$  state has a negative  $A_2/A_0$  value, suggesting a dipole transition. There is no measurable lifetime associated with the  $4007+\Delta\text{-keV}$  state, which is assigned  $J^\pi = 31/2^+$  from the spin and parity assignments made in the parallel branch depopulating this state. Hence the 566-keV transition must have  $E1$  multipolarity, i.e.  $31/2^+ \rightarrow 29/2^-$ .

The  $27(3)\text{-ns}$  lifetime of the  $2610+\Delta\text{-keV}$  level and the measured negative  $A_2/A_0$  value of the 322-keV transition

TABLE I. New  $\gamma$ -ray transitions placed above the  $J^\pi = 17/2^-$  isomer in  $^{213}\text{Ra}$ . Relative intensities are normalized to that of the 518-keV  $\gamma$ -ray transition. Evidence for their placement in the level scheme, along with  $\sigma L$  and  $J^\pi$  assignments, are discussed in the text. The state energies contain the  $+\Delta$  term due to the unknown energy of the  $J^\pi = 17/2^- \rightarrow 13/2^-$  transition.

$E_\gamma$	$I_\gamma$	$E_i - \Delta$	$J_i^\pi$	$E_f - \Delta$	$J_f^\pi$	$\sigma L$	$\alpha_T(\text{exp.})$	$\alpha_T(\text{calc.})$	$A_2/A_0$
(8.2)		3441	$29/2^-$	3433	$27/2^-$	$M1$			
(14.4)		3878	$29/2^+$	3863	$27/2^+$	$M1$			
(40.9)		4048	$33/2^+$	4007	$31/2^+$	$M1$			
87.6(4)		3433	$27/2^-$	3345	$25/2^-$	$M1$			
152.1(5)	2.3(2)	3433	$27/2^-$	3281	$25/2^-$	$M1+E2^b$	3.7(5)	4.75	
169.7(3)	4.4(2)	4048	$33/2^+$	3878	$29/2^+$	$E2$	1.3(2)	1.1	
275.0(4)	4.2(2)	3340	$27/2^+$	3065	$25/2^+$	$M1$	0.99(8)	0.9	$-0.41(16)$
296.6(2)	12.3(3)	3433	$27/2^-$	3136	$25/2^-$	$M1$	0.96(9)	0.74	$-0.73(4)$
304.8(8)	1.8(2)	3441	$29/2^-$	3136	$25/2^-$	$E2$			
322.4(1)	44.6(6)	2610	$23/2^+$	2287	$21/2^-$	$E1$	0.11(5)	0.03	$-0.31(5)$
436.7(8)	2.4(2)	3878	$29/2^+$	3441	$29/2^-$	$E1$			
455.4(4)	7.1(3)	3065	$25/2^+$	2610	$23/2^+$	$M1$			$-1.06(6)$
458.7(6) <sup>a</sup>		(4507+ $\Delta'$ )	( $37/2^+$ )	(4048+ $\Delta'$ )					
517.5(1)	100	2287	$21/2^-$	1770	$17/2^-$	$E2$			0.26(1)
537.8(11)	2.0(2)	3878	$29/2^+$	3340	$27/2^+$	$M1$			$-0.46(7)$
565.5(2)	41.0(7)	4007	$31/2^+$	3441	$29/2^-$	$E1$			$-0.46(6)$
606.3(5)	5.4(3)	4048	$33/2^+$	3441	$29/2^-$	$M2+E3^c$			
666.5(4)	10.0(4)	4007	$31/2^+$	3340	$27/2^+$	$E2$			0.38(13)
730.5(5)	5.8(3)	3340	$27/2^+$	2610	$23/2^+$	$E2$			0.38(17)
798.5(10)	0.7(2)	3863	$27/2^+$	3065	$25/2^+$	$M1+E2^c$			
849.1(3)	24.4(6)	3136	$25/2^-$	2287	$21/2^-$	$E2$			0.38(4)
993.6(7)	3.7(3)	3281	$25/2^-$	2287	$21/2^-$	$E2$			0.33(14)
1058.1(2)	28.3(7)	3345	$25/2^-$	2287	$21/2^-$	$E2$			0.30(5)

<sup>a</sup> The possible placement of this transition above an unobserved low-energy ( $\Delta'$ -keV),  $J^\pi = 35/3^+ \rightarrow 33/2^+$  transition is discussed in the text.

<sup>b</sup> With a mixing ratio of  $|\delta(E2/M1)| = 0.7(3)$ . The calculated  $\alpha_T$  is for the dominant  $M1$  component.

<sup>c</sup> Transition multipolarity implied by the determined spins and parities of initial and final states.

TABLE II. Transitions coincident with strong transitions in  $^{213}\text{Ra}$  that could not be placed in the level scheme due to insufficient statistics. These transitions do not occur following the decay of an isomeric state and bypass the isomer at  $4048+\Delta$  keV.

Transition energy (keV)	Coincident transitions (keV) <sup>a</sup>
204	314, 377, 397/398, 416, 447
314	204, 377, 397/398, 416, 447
377	204, 314, 397/398, 416, 447
397	204, 314, 377, 398, 416, 447
398	204, 314, 377, 397, 416, 447
416	204, 377, 397/398
447	204, 377, 397/398
459	397/398, 565, 667

<sup>a</sup> The transitions are also coincident with the 297-keV, 518-keV, 849-keV, 994-keV and 1058-keV transitions.

provide compelling evidence that it is an  $E1$  transition, with the measured value of the conversion coefficient,  $\alpha_T = 0.11(5)$ , only  $1.6\sigma$  from the expected  $E1$  value of 0.03 and very far from the expected  $M1$  value of 0.584. Thus,  $J^\pi = 23/2^+$  is assigned to the  $2610+\Delta$ -keV level. The  $3065+\Delta$ -keV level is assigned  $J^\pi = 25/2^+$  on the basis of the  $M1$  character of the 455-keV  $\gamma$  ray. The internal

conversion coefficient for the 275-keV transition supports  $M1$  nature and the angular distribution of the 731-keV transition supports a quadrupole assignment. Therefore, the 3340+ $\Delta$ -keV state is assigned  $J^\pi = 27/2^+$ . The 538-keV and 667-keV transitions have been assigned as  $M1$  and  $E2$  on similar arguments so that the 3878+ $\Delta$ -keV state is assigned as  $J^\pi = 29/2^+$  and the 4007-keV state is assigned as  $J^\pi = 31/2^+$ . The known spins and parities below the  $J^\pi = 29/2^+$  level imply the 437-keV, 799-keV and 14-keV transitions are  $E1$ ,  $M1$  and  $M1$ , respectively.

The 170-keV transition depopulating the isomer at  $4048+\Delta$ -keV has a measured total conversion coefficient consistent with that of an  $E2$  transition, which implies  $J^\pi = 33/2^+$  for this isomer. Hence, the 41-keV transition is  $M1$  and the 606-keV transition is  $M2$ , or more likely mixed  $M2+E3$  (see below). As discussed below, the  $M1$  nature of the 41-keV transition is reinforced by the relative fraction of strength carried by this  $\gamma$  ray compared to the 606-keV  $M2+E3$  or the 170-keV  $E2$  transitions.

## 2. Spin-parity assignments in $^{212}\text{Ra}$

Assigning spins and parities to excited states in  $^{212}\text{Ra}$  was more challenging than in  $^{213}\text{Ra}$  due to fission compe-

TABLE III.  $\gamma$ -ray transitions observed above the  $J^\pi = 8^+$  isomer in  $^{212}\text{Ra}$ . Relative intensities are normalized to the 619-keV  $\gamma$  ray. Evidence for placements in the level scheme, as well as  $\sigma L$  and  $J^\pi$  assignments, are discussed in the text.

$E_\gamma$	$I_\gamma$	$E_i$	$J_i^\pi$	$E_f$	$J_f^\pi$	$\sigma L$	$\alpha_T(\text{exp.})$	$\alpha_T(\text{calc.})$	$A_2/A_0$
(29.3)		3632	$13^-$	3603					
(36.1)		2613	$11^-$	2577	$10^+$	$E1$			
(90.5)		4197	$16^-$	4107	$15^-$	$M1$			
122.5(1)		2700	$12^+$	2577	$10^+$	$E2$	4.7(10)	4.035	
150.0(2)	4.9(6)	2109	$8^+$	1958	$8^+$	$M1$			
153.1(2)	5.9(14)	4351	$17^-$	4197	$16^-$	$M1$	5.0(3)	4.63	1.0(4)
201.7(1)	7.9(16)	4553	$18^-$	4351	$17^-$	$M1+E2^a$	1.89(11)	2.13	0.3(2)
248.8(1)	35.8(40)	4197	$16^-$	3949	$14^-$	$E2$	0.31(4)	0.273	0.24(14)
260.6(1)	24.9(30)	6138		5877					0.45(23)
282.5(1)	23.1(31)	3404	$13^-$	3122	$12^-$	$M1$	0.98(5)	0.835	-0.66(17)
289.7(1)	14.0(23)	5415		5125					-0.6(3)
317.3(1)	7.5(18)	3949	$14^-$	3632	$13^-$	$M1$	0.65(13)	0.608	
371.1(1)	13.2(24)	5415		5041	$19^+$				
462.4(1)	17.6(33)	5877		5415					-0.3(4)
475.2(2)	10.4(24)	4107	$15^-$	3632	$13^-$	$E2$			
490.9(1)	30.3(45)	5041	$19^+$	4553	$18^-$	$E1$			-0.23(18)
493.1(2)	9.1(22)	6370		5877					
504.9(2)	27.4(22)	2613	$11^-$	2109	$8^+$	$E3$			
508.3(1)	51.1(58)	3122	$12^-$	2613	$11^-$	$M1$			-0.85(10)
544.8(1)	41.5(52)	3949	$14^-$	3404	$13^-$	$M1$			-0.07(15)
618.8(1)	48.9(35)	2577	$10^+$	1958	$8^+$	$E2$			
654.9(2)	23.7(23)	2613	$11^-$	1958	$8^+$	$E3$			
703.1(1)	16.5(39)	4107	$15^-$	3404	$13^-$	$E2$			0.7(2)
774.1(1)	8.9(26)	5125		4351	$17^-$				
791.0(1)	40.1(59)	3404	$13^-$	2613	$11^-$	$E2$			0.48(14)
833.7(1)	19.8(44)	5877		5041	$19^+$				
932.0(1)	5.1(23)	3632	$13^-$	2700	$12^+$	$E1$			
1025.2(2)	3.6(30)	3603		2577	$10^+$				

<sup>a</sup> With a mixing ratio of  $|\delta(E2/M1)| = 0.43_{-13}^{+12}$

tition and hence reduced statistics, particularly for levels above 4197 keV. No spin or parity assignments could be made for levels located above the 5041-keV isomer. The present work confirms the spin assignments made to ten excited states in  $^{212}\text{Ra}$  by Kohno *et al.* [13], adding parity assignments to two of these levels, although there are significant differences between their level scheme and the present one for states above the  $J^\pi = 13^-$ , 3404-keV level.

The internal conversion coefficient inferred from intensity balances for the 123-keV transition suggests it is an  $E2$  transition, thus connecting a  $J^\pi = 12^+$  level at 2700 keV to the 2577-keV,  $J^\pi = 10^+$  level. The  $A_2/A_0$  value of the 508-keV transition is consistent with  $M1$  nature and so the previously reported [13] 3122-keV,  $J = 12$  state is confirmed and assigned a negative parity. The spin and parity of  $J^\pi = 13^-$  for the 3404-keV level is confirmed by the measured internal conversion coefficient for the  $M1$  283-keV transition connecting it to the 3122-keV,  $J^\pi = 12^-$  level. The measured  $A_2/A_0$  value for the intense 791-keV transition depopulating this  $J^\pi = 13^-$  state and feeding the 2613-keV,  $J^\pi = 11^-$  isomer is consistent with an  $E2$  multipolarity.

The  $A_2/A_0$  value of the 545-keV transition is consis-

tent with  $M1$  nature and so the 3949-keV state is assigned  $J^\pi = 14^-$ . The internal conversion coefficient of the 249-keV transition feeding this state suggests it is an  $E2$  transition and so the 4197-keV state is assigned  $J^\pi = 16^-$ . From its measured internal conversion coefficient, the 317-keV transition that depopulates the  $14^-$  level was found to be an  $M1$  transition and so a  $J^\pi = 13^-$  assignment is made to the 3632-keV state. The 3632-keV,  $J^\pi = 13^-$  level is connected to the 2700-keV,  $J^\pi = 12^+$  level by a 932-keV  $\gamma$ -ray transition. An  $E1$  assignment is required for this transition to be consistent with the spin-parity assignments discussed above.

Measured internal conversion coefficients for the 153-keV and 202-keV transitions support  $M1$  assignments to both and so the 4351-keV and 4553-keV levels are assigned  $J^\pi = 17^-$  and  $J^\pi = 18^-$ , respectively. Although the  $A_2/A_0$  values measured for the 153-keV and 202-keV transitions are inconsistent with pure  $M1$  assignments, introducing a mixing ratio of  $|\delta(E2/M1)| = 0.43_{-13}^{+12}$  reproduces the angular distribution measured for the 202-keV transition. With this mixing ratio, the theoretical internal conversion coefficient becomes 1.94, bringing it closer to the measured value. The same technique could not be applied to the 153-keV transition, which is ham-

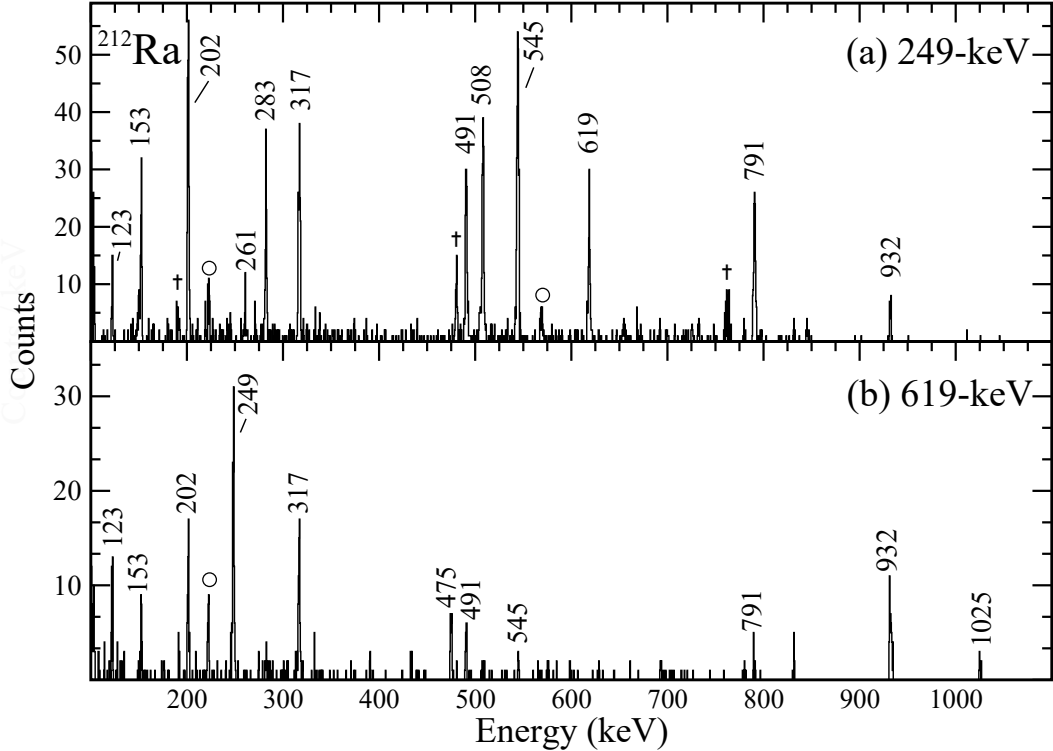


FIG. 5. Background-subtracted, out-of-beam (+30 ns to +140 ns after the beam pulse) coincidence spectra gated on the (a) 249-keV,  $J^\pi = 16^- \rightarrow 14^-$  and (b) 619-keV,  $J^\pi = 10^+ \rightarrow 8^+$  transitions in  $^{212}\text{Ra}$ . Contaminant  $\gamma$ -ray transitions indicated by the symbol † arise due to the reaction product  $^{209}\text{Rn}$ . The transitions labeled with ○ are coincident with a number of  $^{212}\text{Ra}$   $\gamma$  rays and radium x rays but could not be placed in the level scheme.

perered by statistical uncertainties; the unusually large  $A_2/A_0$  value in this case has been disregarded and the spin-parity assignment based upon the internal conversion coefficient alone.

The 491-keV transition that feeds the 4553-keV level has a negative  $A_2/A_0$  value, which, when considered in conjunction with the measured state lifetime of 31(3) ns, implies  $E1$  multipolarity. Therefore, a  $J^\pi = 19^+$  assignment has been made to the isomeric state at 5041 keV.

#### G. Transition strengths

Transition strengths determined from the isomeric-state lifetimes measured for  $^{213}\text{Ra}$  and  $^{212}\text{Ra}$  are shown in Table IV, along with the strengths for some related transitions in neighbouring nuclei [6, 8, 19–21].

As expected, since  $E1$  transitions are not possible between the valence orbitals in the major shells, the  $E1$  transition strengths are all very weak, typically of order  $10^{-7}$  W.u. In  $^{212}\text{Ra}$ , the  $E3$  decays of the 2613-keV  $J^\pi = 11^-$  state to the two lower  $J^\pi = 8^+$  states are observed. In  $^{213}\text{Ra}$ , the  $J^\pi = 33/2^+$  isomer is depopulated by retarded  $M1$  and  $E2$  transitions, as well as a transition that is likely of mixed  $M2 + E3$  multipolarity. These transition strengths will be discussed in further detail below.

#### IV. DISCUSSION

Due to their proximity to the  $N = 126$  neutron shell closure, it is expected that single-particle excitations will be dominant in  $^{213}\text{Ra}$  and  $^{212}\text{Ra}$ . There are limited large basis calculations available for high-spin states in nuclei

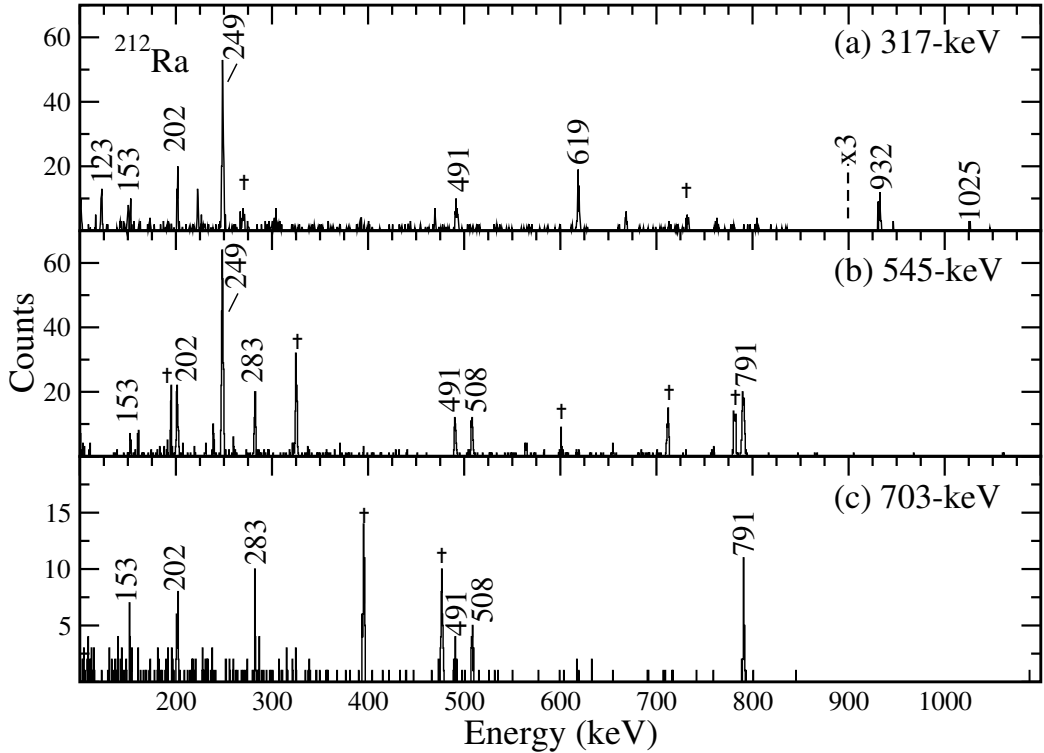


FIG. 6. Background-subtracted, out-of-beam (+30 ns to +140 ns after the beam pulse) coincidence spectra gated on the (a) 317-keV,  $J^\pi = 14^- \rightarrow 13^-$ , (b) 545-keV,  $J^\pi = 14^- \rightarrow 13^-$ , and (c) 703-keV,  $J^\pi = 15^- \rightarrow 13^-$  transitions in  $^{212}\text{Ra}$ . Contaminant  $\gamma$ -ray transitions, indicated by the symbol †, arise primarily due to the reaction products  $^{206}\text{Po}$  and  $^{209}\text{Po}$ .

beyond  $^{208}\text{Pb}$  [22]. However, there has been considerable success with a semiempirical approach to several isotopes of Rn, Fr, and Ra near  $N = 126$  [4, 6–9, 16, 19–21, 23–31]. The experimental level schemes of  $^{212}\text{Ra}$  and  $^{213}\text{Ra}$  were therefore compared with semiempirical shell model calculations. We designate the calculations as “semiempirical” because they are based on empirical single-particle energies and empirical two-body interactions, as far as possible. An additional approximation is also made: configuration mixing is excluded. Thus the calculations include a diagonalization over alternative angular momentum couplings for a given orbital occupation (configuration), but do not allow the nucleons to change their orbits. The Hamiltonian for this model can be written as usual as

$$H = \sum_i H_0(i) + \sum_{i < j} V(ij), \quad (1)$$

where  $H_0$  is the single-particle contribution and  $V$  the two-body residual interaction. Introducing the approximation that the residual interaction does not change or mix configurations, the excitation energy (relative to the ground state of  $^{208}\text{Pb}$ ) can be written as

$$E = \sum_i \langle i | H_0 | i \rangle + \sum_{i < j} \langle ij | V | ij \rangle, \quad (2)$$

where  $\langle H_i \rangle = \langle i | H_0 | i \rangle$  represents the empirical single-particle energies and  $\langle V_{ij} \rangle = \langle ij | V | ij \rangle$  the empirical two-body residual interactions. Experimental values for  $\langle H_i \rangle$  and  $\langle V_{ij} \rangle$  are tabulated in Ref. [26] and references therein. Where empirical interactions are not available they were taken from Ref. [32]. We discuss first the case of  $^{213}\text{Ra}$ , which has a single neutron hole relative to the  $N = 126$  shell closure, and second consider  $^{212}\text{Ra}$ , which has two neutron holes.

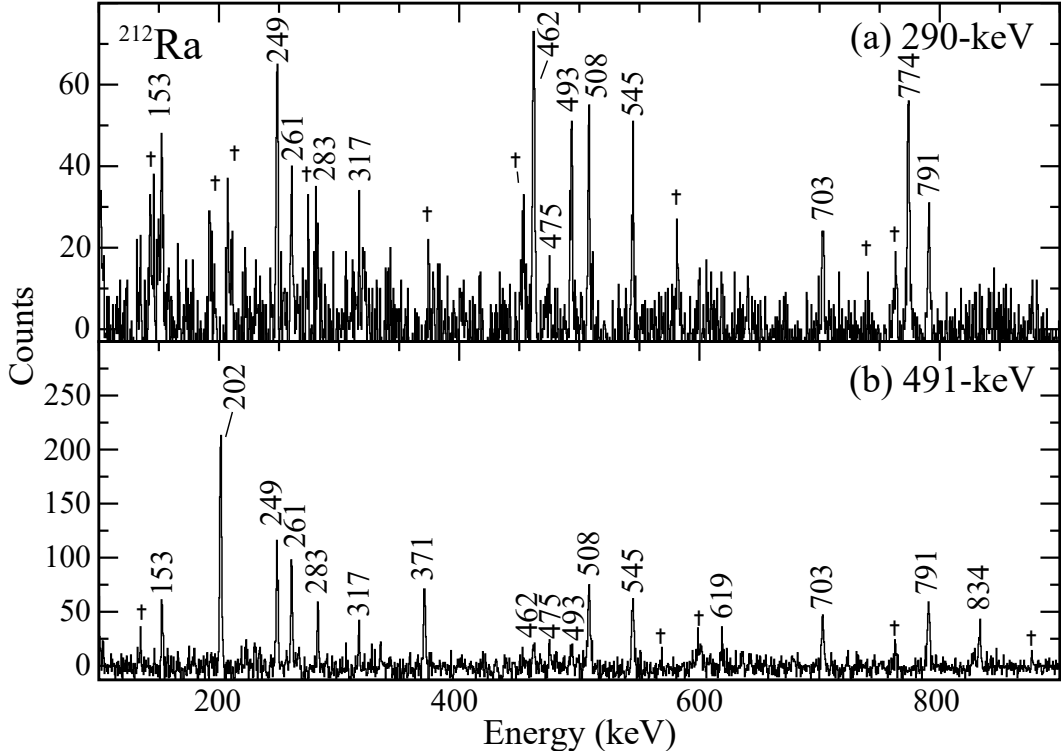


FIG. 7. Background-subtracted, in-beam ( $-13$  ns to  $+30$  ns around the beam pulse) coincidence spectra gated on the (a) 290-keV and (b) 491-keV,  $J^\pi = 19^+ \rightarrow 18^-$  transitions in  $^{212}\text{Ra}$  that demonstrate the presence of short-lived states above the level at 5041 keV. Contaminant  $\gamma$ -ray transitions indicated by the symbol  $\dagger$  come from a number of excited nuclei populated in the reaction, for example  $^{204}\text{Pb}$ .

### A. Shell model calculations and structure of $^{213}\text{Ra}$

#### 1. Weak-coupling approximation.

The observed states in  $^{213}\text{Ra}$  can be formed by the coupling of a  $\nu p_{1/2}$  or  $\nu f_{5/2}$  neutron hole to excited states in  $^{214}\text{Ra}$ . Before performing the detailed semiempirical shell model calculations, it is instructive to begin with a simplified calculation of the level scheme of  $^{213}\text{Ra}$  by weakly coupling a neutron hole in either the  $\nu p_{1/2}$  or  $\nu f_{5/2}$  orbit to the observed level structure in  $^{214}\text{Ra}$ . We assume that (1) the resultant state in  $^{213}\text{Ra}$  has the maximum spin coupling, and (2) the residual interactions are equal in all states (as a consequence of the weak-coupling approximation). Thus the excited states associated with  $\nu p_{1/2}$  have the same excitation energies as in  $^{214}\text{Ra}$  but have the spin increased by  $\frac{1}{2}\hbar$ . Similarly, the states associated

with the  $\nu f_{5/2}$  hole have the  $^{214}\text{Ra}$  level spins increased by  $\frac{5}{2}\hbar$  and their energies shifted up by 570 keV (the excitation energy of the first-excited  $J^\pi = 5/2^-$  state in  $^{207}\text{Pb}$ ). Figure 13 shows the results of this calculation.

As evident from Figure 13, many of the excited states observed in  $^{213}\text{Ra}$  exhibit clear relationships to the  $^{214}\text{Ra}$  level scheme. Focusing first on states associated with levels in  $^{214}\text{Ra}$  up to the first  $J^\pi = 8^+$  state, nominally from the  $\pi h_{9/2}^6$  configuration, we see that the  $J^\pi = 1/2^-$  ground state is associated with  $(^{214}\text{Ra}; J_p = 0_1^+) \otimes \nu p_{1/2}^{-1}$ . ( $J_p$  represents the spin of the protons.) Likewise, the sequence of negative parity states with  $\Delta J = 2$  from  $J^\pi = 9/2^-$  to  $J^\pi = 17/2^-$  is associated with coupling the  $\nu p_{1/2}$  hole to the  $J^\pi = 4^+$ ,  $J^\pi = 6^+$  and  $J^\pi = 8^+$  members of the nominal  $\pi h_{9/2}^6$  configuration in  $^{214}\text{Ra}$ . The observed  $J^\pi = 5/2^-$  state is associated with  $(^{214}\text{Ra}; J_p = 0_1^+) \otimes \nu f_{5/2}^{-1}$ , whereas the alternative

TABLE IV. Transition strengths for isomeric decays in  $^{212}\text{Ra}$  and  $^{213}\text{Ra}$ . Transition strengths in  $^{214}\text{Ra}$  as well as  $^{210,211,212}\text{Rn}$  have been included for comparison [6, 8, 19–21].

Nucleus	$E_{\text{level}}$ (keV)	$J_i$	$\tau$ (ns)	$E_{\gamma}$ (keV)	$\sigma L$	Transition Strength (W.u.)	Reference
$^{212}\text{Ra}$	2613	11 $^-$	$1.2(2) \times 10^3$ <sup>a</sup>	505	$E3$	14.4(33)	present work
				655	$E3$	2.1(6)	present work
				36	$E1$	$9.6(2) \times 10^{-7}$	present work
$^{213}\text{Ra}$	5041	19 $^+$	31(3)	491	$E1$	$7.4(7) \times 10^{-8}$	present work
				323	$E1$	$2.7(3) \times 10^{-7}$	present work
				170	$E2$	$5.3(6) \times 10^{-3}$	present work
				41	$M1$	$1.76(11) \times 10^{-4}$	present work
				606	$M2^b$	$2.5(2) \times 10^{-4}$	present work
				606	$E3^b$	36(3)	present work
$^{214}\text{Ra}$	2683	11 $^-$	426(10)	609	$E3$	21.7(6)	[8]
				818	$E3$	3.1(1)	[8]
	4810	18 $^+$	1.1(3)	409	$E1$	$1.2(3) \times 10^{-6}$	[8]
				663	$E1$	$4(1) \times 10^{-7}$	[8]
	6530	(24 $^+$ )	2.3(4)	48	$M1$	$\sim 4 \times 10^{-3}$ <sup>c</sup>	[8]
				240	$E2$	$\sim 0.2$ <sup>c</sup>	[8]
$^{210}\text{Rn}$	2563	11 $^-$	92(5)	186	$E1$	$3.5(2) \times 10^{-7}$	[19]
				898	$E3$	2.7(3)	[19]
$^{211}\text{Rn}$	2650+ $\Delta$	23/2 $^+$	9.6(4)	503	$E1$	$2.2(1) \times 10^{-7}$	[20, 21]
				1073	$E3$	1.1(4)	[20]
$^{212}\text{Rn}$	2761	11 $^-$	8(3)	106	$E1$	$2.1(1) \times 10^{-5}$	[6]

<sup>a</sup> Lifetime from Ref. [13].

<sup>b</sup> Alternative multipolarities. Strengths assume either a pure  $M2$  or a pure  $E3$  transition.

<sup>c</sup> Tentative values since the initial state was not firmly assigned in Ref. [8].

$(^{214}\text{Ra}; J_p = 2_1^+)$   $\otimes \nu p_{1/2}^{-1}$  is not observed because it is non-yrast. The  $J^\pi = 21/2^-$  level can be assigned as  $(^{214}\text{Ra}; J_p = 8^+)$   $\otimes \nu p_{5/2}^{-1}$ . There is a second  $J^\pi = 8^+$

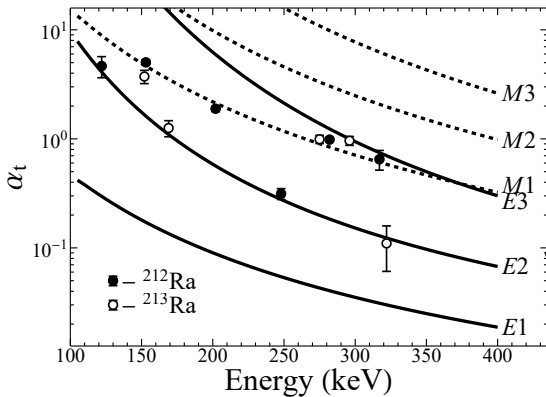


FIG. 8. Total internal conversion coefficients deduced from intensity balances of low-energy transitions in  $^{212}\text{Ra}$  (filled circles) and  $^{213}\text{Ra}$  (open circles). Solid and dashed lines are theoretical values for electric and magnetic transitions, respectively, calculated using BRICC [14].

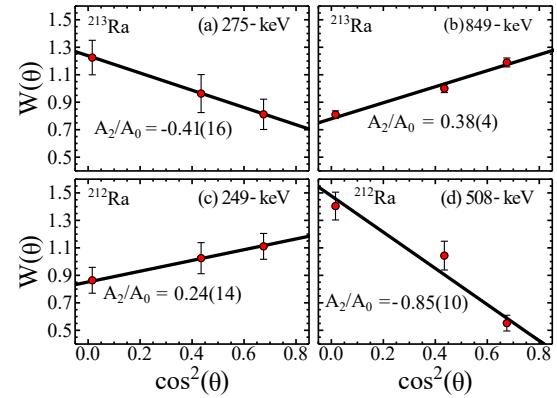


FIG. 9. Measured angular distributions plotted for the (a) 275-keV and (b) 849-keV transitions in  $^{213}\text{Ra}$ , and the (c) 249-keV and (d) 508-keV (d) transitions in  $^{212}\text{Ra}$ . The data points correspond to the three detector pairs positioned in the vertical plane relative to the beam axis at  $\pm 34^\circ$ ,  $\pm 48^\circ$  and  $\pm 82^\circ$ .

state in  $^{214}\text{Ra}$  which has no analog in the observed  $^{213}\text{Ra}$  level scheme.

The  $J^\pi = 23/2^+$  level at 2610 +  $\Delta$  keV can be as-

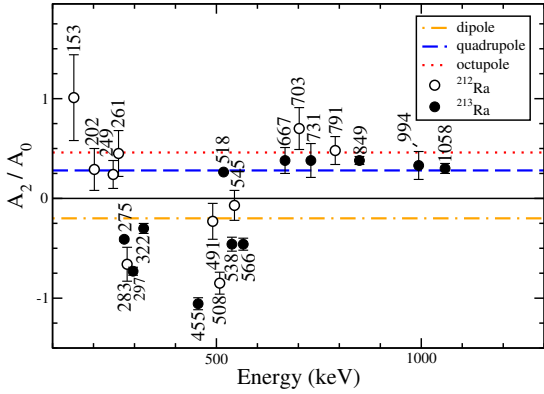


FIG. 10. Extracted values of  $A_2/A_0$  obtained for  $\gamma$ -ray transitions in  $^{212}\text{Ra}$  (open circles) and  $^{213}\text{Ra}$  (closed circles). Dashed horizontal lines at  $-0.2$ ,  $0.26$  and  $0.46$  are the calculated values for pure dipole, quadrupole and octupole transitions assuming an alignment due to a Gaussian  $m$ -substate distribution with  $\sigma/J = 0.3$  (see, for example, Ref. [17]). A significant deviation from these lines is an indication of a mixed multipolarity transition.

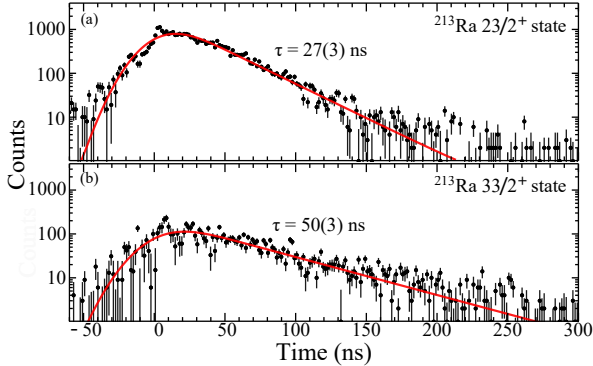


FIG. 11. The  $\gamma\gamma$  time-difference spectra showing the mean lives of the (a)  $J^\pi = 23/2^+$  and (b)  $J^\pi = 33/2^+$  isomers in  $^{213}\text{Ra}$  (see text for gating transition details).

sociated with the  $(^{214}\text{Ra}; J_p = 11^-) \otimes \nu p_{1/2}^{-1}$  configuration, where the  $^{214}\text{Ra}$   $J^\pi = 11^-$  level is nominally from the configuration  $\pi h_{9/2}^5 i_{13/2}$ . However, above this level, the identification of corresponding experimental and calculated levels becomes more challenging. In the case of the yrast  $J^\pi = 25/2^+$  state, there is no predicted level; presumably this level originates from a  $(^{214}\text{Ra}; J_p = 12^-) \otimes \nu p_{1/2}^{-1}$  coupling, but, as discussed further below, the relevant experimental level in  $^{214}\text{Ra}$  is not observed. In other cases there are several possible calculated configurations for the observed states, and

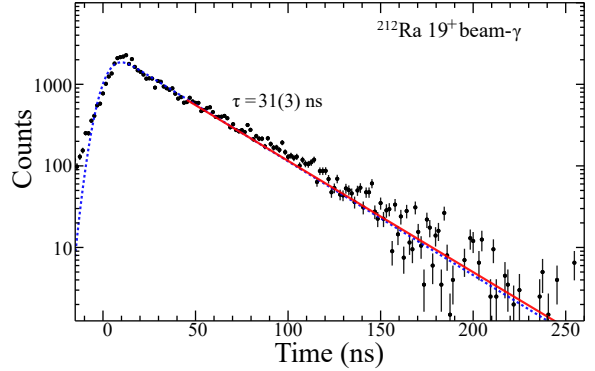


FIG. 12. Histogram of the number of 491-keV  $\gamma$  rays versus time between beam pulses, which define  $t = 0$ . A mean life of  $31(3)$  ns was obtained by combining results from fitting the decay curve with either the slope (solid red), or including the full prompt and slope components (dotted blue).

configuration mixing must be expected. For example, the  $J^\pi = 9/2^-$  states from  $(^{214}\text{Ra}; J_p = 4^+) \otimes \nu p_{1/2}^{-1}$  and  $(^{214}\text{Ra}; J_p = 2^+) \otimes \nu f_{5/2}^{-1}$ , are quite close in energy.

Three  $J^\pi = 25/2^-$  states are observed near 3.2 MeV excitation energy. Two of these can be explained by the coupling of a  $\nu p_{1/2}^{-1}$  neutron hole to the two  $J^\pi = 12^+$  states in  $^{214}\text{Ra}$ . The third arises from the coupling of a  $\nu f_{5/2}^{-1}$  neutron hole to the  $J^\pi = 10^+$  state and exists, as in experiment, on the order of 100 keV higher than the other two. The  $J^\pi = 27/2^-$  state in  $^{213}\text{Ra}$  has no corresponding state in  $^{214}\text{Ra}$ , although it is likely to arise from a  $\nu p_{1/2}^{-1}$  neutron hole coupled to a  $(h_{9/2}^5 \otimes f_{7/2})_{13+}$  proton configuration. The  $J^\pi = 29/2^-$  state near 3.4 MeV could be produced by four possible couplings: a  $\nu p_{1/2}^{-1}$  neutron hole coupled to one of two  $J^\pi = 14^+$  states; or the  $\nu f_{5/2}^{-1}$  neutron hole coupled to one of the two  $J^\pi = 12^+$  states. The lowest in energy of these possible configurations,  $(^{214}\text{Ra}; J_p = 14^+) \otimes \nu p_{1/2}$ , nominally  $\pi(h_{9/2}^5 f_{7/2})_{14+} \otimes \nu p_{1/2}$ , is closest in energy to the observed state, and is therefore the most likely candidate.

Two  $J^\pi = 33/2^-$  states are predicted that have not been observed in  $^{213}\text{Ra}$ . However, weak decay paths were observed which bypass the  $J^\pi = 33/2^+$  isomer through states that could not be placed in the experimental level scheme (see Table II). Some of these unplaced states could be candidates for the unobserved predicted states.

The splitting of the experimental level scheme of  $^{213}\text{Ra}$  into separate cascades connecting either positive or negative states is evident in Fig. 1, between the  $J^\pi = 21/2^-$  and  $J^\pi = 33/2^+$  states. The weak-coupling calculations better reproduce the negative parity sequence than the positive parity states, where predictions are missing for some observed states.

Overall, of the seven positive-parity states observed

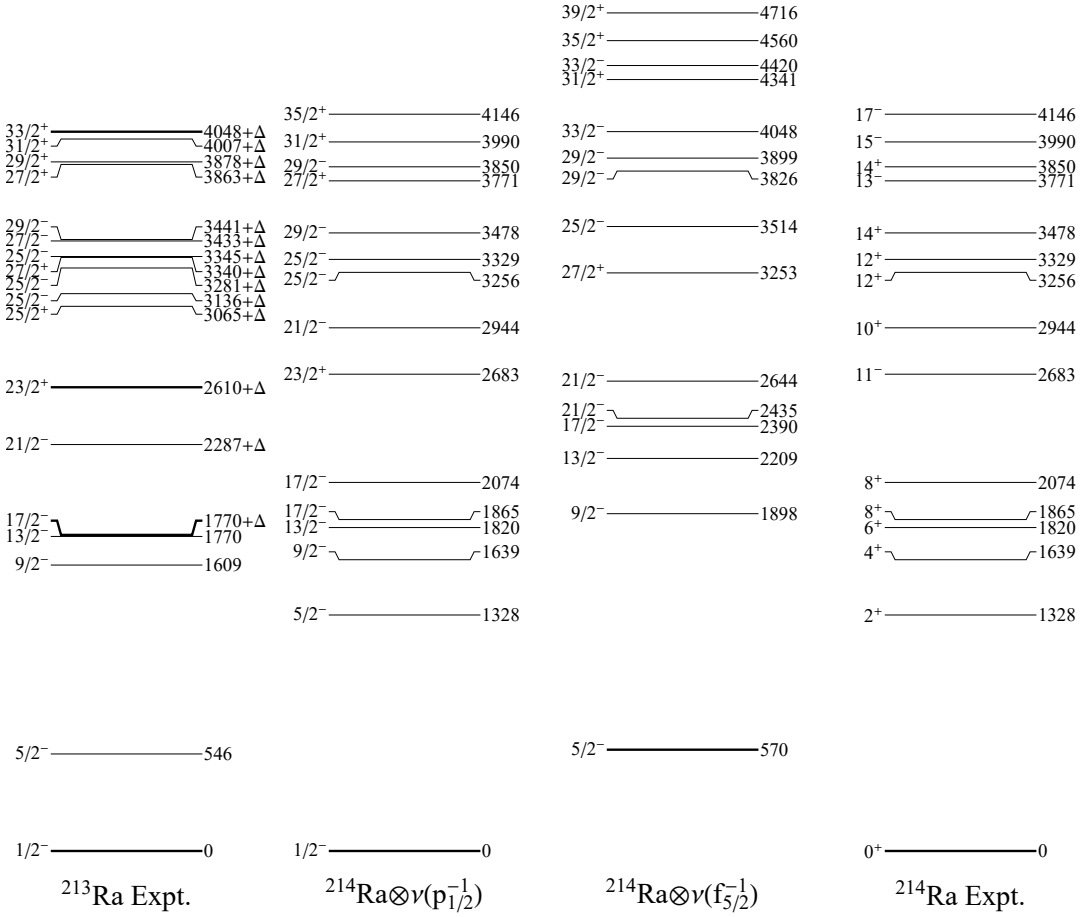


FIG. 13. Calculated level schemes for the weak coupling of either a  $\nu p_{1/2}^{-1}$  or  $\nu f_{5/2}^{-1}$  neutron hole to the known excited states in  $^{214}\text{Ra}$  [8], which is shown to the right for reference. The  $^{213}\text{Ra}$  level scheme is shown to the left. Isomeric states in  $^{213}\text{Ra}$  are indicated by thicker lines.

in  $^{213}\text{Ra}$ , five are predicted by the weak-coupling calculation. As already noted, the  $J^\pi = 23/2^+$  isomer in  $^{213}\text{Ra}$  is explained by the coupling of the  $\nu p_{1/2}^{-1}$  neutron to the  $J^\pi = 11^-$  state in  $^{214}\text{Ra}$ , i.e. it has nominal configuration  $\pi(h_{9/2}^5 \otimes i_{13/2})_{11-} \otimes \nu p_{1/2}^{-1}$ . Above this state, both  $J^\pi = 27/2^+$  states are reproduced, one from  $\pi(h_{9/2}^5 \otimes i_{13/2})_{13-} \otimes \nu p_{1/2}^{-1}$  and the other from  $\pi(h_{9/2}^5 \otimes i_{13/2})_{11-} \otimes \nu f_{5/2}^{-1}$ . The energy spacing between the predicted  $J^\pi = 27/2^+$  states is consistent with the experimental difference of  $\sim 520$  keV. However, predictions for the  $J^\pi = 25/2^+$ ,  $J^\pi = 29/2^+$  and  $J^\pi = 33/2^+$  states in  $^{213}\text{Ra}$  are missing. Clearly, to predict these positive parity states in  $^{213}\text{Ra}$ , the simple weak-coupling model requires the observation of the associated negative-

parity state in  $^{214}\text{Ra}$ . The relevant states have  $J^\pi = 10^-$ ,  $J^\pi = 12^-$ ,  $J^\pi = 14^-$  and  $J^\pi = 16^-$ . These states are not observed in  $^{214}\text{Ra}$  because the observed near-yrast cascade from  $J^\pi = 17^-$  to  $J^\pi = 11^-$  in  $^{214}\text{Ra}$  by-passes the even- $J$ , odd-parity states.

At higher excitation energies, two  $J^\pi = 31/2^+$  and two  $J^\pi = 35/2^+$  states are predicted, but only one of each is observed. The  $\nu p_{1/2}^{-1}$  coupling to  $J^\pi = 15^-$  well reproduces the  $J^\pi = 31/2^+$  state, and, as the other level is higher and non-yrast, its non-observation is to be expected. In contrast, the short-comings of this simple approach are becoming apparent in the predictions of the  $J^\pi = 35/2^+$  states. The  $\nu f_{5/2}^{-1}$  neutron-hole coupling to  $J^\pi = 15^-$  closely matches the experimental energy of the experimental  $J^\pi = 35/2^+$  state, but the predicted lower

state is not observed, which is problematic because if it were yrast, as predicted, it should have been observed.

To sum up this section, the weak-coupling model calculations have allowed us to assign likely configurations to most of the observed excited states in  $^{213}\text{Ra}$ . The good agreement achieved for states up to the  $J^\pi = 23/2^+$  level is particularly important to confirm that the level structure observed above the  $J^\pi = 17/2^-$  isomer is indeed in  $^{213}\text{Ra}$ , since we are unable to perform  $\gamma$ - $\gamma$  coincidences across this long-lived isomer. One limitation of the model is that it relies on the observation of all parent states in  $^{214}\text{Ra}$ , a condition that is not always met. Another limitation is that it assumes all residual proton-neutron interactions are equal, which leads to poor predictions of level energies in some cases.

## 2. Semiempirical shell-model calculations

More comprehensive semiempirical shell-model calculations were performed. These calculations provide the means to assign configurations to the experimentally observed excited states and to discuss the transition strengths in cases where they have been measured.

The calculated levels for  $^{213}\text{Ra}$  are shown in Fig. 14 and the assigned configurations are listed in Table V. The experimental energies of the low-excitation, low-seniority states are overestimated in the calculations, as is expected when configuration mixing is neglected. Overall, however, there are many cases in which the predictions deviate from experiment by only tens of keV, allowing configuration assignments with some confidence. In most cases where alternative configurations are available, that lying closest in energy to the experimental level is expected to be dominant in the wavefunction. As will be discussed in greater detail below, the  $\pi(h_{9/2}^6 i_{13/2}) \otimes \nu p_{1/2}^{-1}$  configuration consistently under predicted the experimental energies, and the states associated with this configuration have been moved up in energy by 250 keV throughout the following discussion, including in the Figures and Tables.

### Negative-parity configurations

The following configurations account for the observed negative-parity states in  $^{213}\text{Ra}$ :

- $\pi h_{9/2}^6 \otimes \nu p_{1/2}^{-1}$ ;
- $\pi h_{9/2}^6 \otimes \nu f_{5/2}^{-1}$ ; and
- $\pi(h_{9/2}^5 f_{7/2}^1) \otimes \nu p_{1/2}^{-1}$ .

The  $\pi h_{9/2}^6 \otimes \nu p_{1/2}^{-1}$  configuration can produce states up to a maximum  $J^\pi = 25/2^-$ . As expected, the low-seniority states associated with this configuration and  $\pi h_{9/2}^6 \otimes \nu f_{5/2}^{-1}$  are poorly reproduced as the effects of configuration mixing are not considered [6, 8, 9]. For

instance, the energy of the ground state, where additional (pairing) correlations are present, is overestimated by 384 keV. However, the calculations do reproduce the energy separation of the first-excited  $J^\pi = 5/2^-$  state and the ground state, confirming the conclusion of the weak-coupling calculation that the  $J^\pi = 5/2^-$  state is predominantly due to the movement of the neutron hole from the  $\nu p_{1/2}^1$  orbital to the  $\nu f_{5/2}^{-1}$  orbital. At higher spin (and higher seniority for  $\pi h_{9/2}^6$ ) the calculated energies are closer to experiment. The energy separation between the  $J^\pi = 17/2^-$ , 1770 +  $\Delta$ -keV state and the  $J^\pi = 21/2^-$ , 2287 +  $\Delta$ -keV state is well described and these states are associated with  $\pi(h_{9/2}^6)_{8+} \otimes \nu p_{1/2}^{-1}$  and  $\pi(h_{9/2}^6)_{8+} \otimes \nu f_{5/2}^{-1}$ , respectively. Thus the 518-keV  $J^\pi = 21/2^- \rightarrow 17/2^-$  transition is analogous to the 546-keV  $J^\pi = 5/2^- \rightarrow 1/2^-$  transition.

The calculation accounts for the existence of the three  $J^\pi = 25/2^-$  states near 3.2 MeV excitation energy. Configuration mixing must be expected, however the order in the calculated level scheme is in reasonable agreement with experiment, suggesting dominant configurations, in order of excitation energy, of  $\pi h_{9/2}^6 \otimes \nu p_{1/2}^{-1}$ ,  $\pi(h_{9/2}^5 f_{7/2}) \otimes \nu p_{1/2}^{-1}$ , and  $\pi h_{9/2}^6 \otimes \nu f_{5/2}^{-1}$ . All three states decay by  $E2$  transitions to the  $J^\pi = 21/2^-$  state, which is expected to have significant  $\pi(h_{9/2}^6)_{10+} \otimes \nu p_{1/2}^{-1}$  admixtures along with the leading term  $\pi(h_{9/2}^6)_{8+} \otimes \nu f_{5/2}^{-1}$ . Thus the  $E2$  transitions can be attributed mainly to  $\pi(h_{9/2}^6)_{10+} \otimes \nu f_{5/2}^{-1} \rightarrow \pi(h_{9/2}^6)_{8+} \otimes \nu f_{5/2}^{-1}$  and  $\pi(h_{9/2}^6)_{12+} \otimes \nu p_{1/2}^{-1} \rightarrow \pi(h_{9/2}^6)_{10+} \otimes \nu p_{1/2}^{-1}$  components.

The  $J^\pi = 27/2^-$  and  $J^\pi = 29/2^-$  states at 3433 +  $\Delta$  keV and 3441 +  $\Delta$  keV have configurations that differ only by recoupling the proton spin to  $\pi(h_{9/2}^5 f_{7/2})_{13+} \otimes \nu p_{1/2}^{-1}$  and  $\pi(h_{9/2}^5 f_{7/2})_{14+} \otimes \nu p_{1/2}^{-1}$ , respectively. In this scenario, the small energy spacing between the  $J^\pi = 27/2^-$  and  $J^\pi = 29/2^-$  states is accounted for. The  $J^\pi = 29/2^- \rightarrow 27/2^- M1$  transition can be associated with  $\pi(h_{9/2}^5 f_{7/2})_{14+} \otimes \nu p_{1/2}^{-1} \rightarrow \pi(h_{9/2}^5 f_{7/2})_{13+} \otimes \nu p_{1/2}^{-1}$ , with a strength proportional to  $(g_{h_{9/2}} - g_{f_{7/2}})^2$  where  $g_{h_{9/2}}$  and  $g_{f_{7/2}}$  are the  $g$  factors of the  $\pi h_{9/2}$  and  $\pi f_{7/2}$  orbits, respectively [33, 34]. In this case, and for similar cases in neighbouring Ra and Rn isotopes [8, 19], the transition strength is of the order of 0.1 W.u., which explains the lack of an observable lifetime for the 8-keV transition.

To sum up, the negative-parity states observed in  $^{213}\text{Ra}$  can be attributed to the  $\pi h_{9/2}^6 \otimes \nu p_{1/2}^{-1}$ ,  $\pi h_{9/2}^6 \otimes \nu f_{5/2}^{-1}$  and  $\pi(h_{9/2}^5 f_{7/2}) \otimes \nu p_{1/2}^{-1}$  configurations.

### Positive-parity configurations

Two configurations giving rise to positive-parity states were considered:

- $\pi(h_{9/2}^5 i_{13/2}) \otimes \nu p_{1/2}^{-1}$ ; and
- $\pi(h_{9/2}^5 i_{13/2}) \otimes \nu f_{5/2}^{-1}$ .

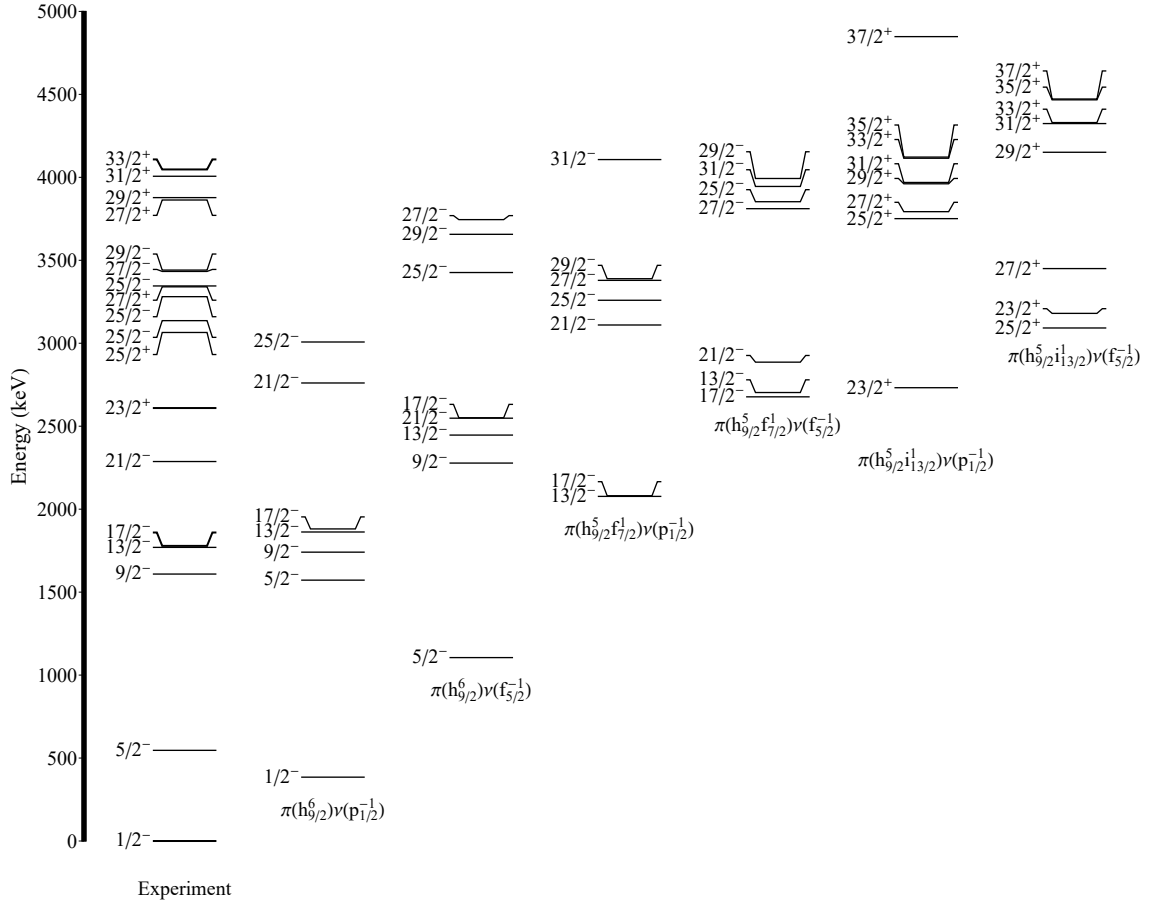


FIG. 14. Comparison between the experimental level scheme of  $^{213}\text{Ra}$  and predictions from the semiempirical shell-model calculations described in the text. Experimental data are shown on the left, while predictions from selected valence particle configurations are shown to the right. The calculated levels for  $\pi[(h_{9/2}^5 i_{13/2}^1) \otimes \nu p_{1/2}^{-1}]$  have been shifted up by 250 keV; see text.

The lowest-energy, positive-parity state observed in  $^{213}\text{Ra}$ , the  $J^\pi = 23/2^+$  isomer, is analogous to the  $J^\pi = 11^-$  isomer in  $^{214}\text{Ra}$  with the additional coupling of a  $\nu p_{1/2}^{-1}$  neutron hole. The dominant configuration is  $\pi(h_{9/2}^5 i_{13/2}^1)_{11-} \otimes \nu p_{1/2}^{-1}$ . In most even-even nuclei in this region, the  $J^\pi = 11^-$  state decays via one or more  $E3$  branches to  $J^\pi = 8^+$  states. In  $^{213}\text{Ra}$ , no  $E3$  transition to the  $J^\pi = 17/2^-$  state was observed. This non-observation of the  $E3$  decay is evidently due, in part, to the intermediate  $J^\pi = 21/2^-$  state, which allows a decay via the 323-keV  $E1$  transition. In the neighboring nucleus,  $^{211}\text{Rn}$ , the corresponding  $E1$  and  $E3$  decays of the  $J^\pi = 23/2^+$  state were observed with a branching ratio of  $I(E3)/I(E1) = (3 \pm 1)\%$ . Scaling by the transition energies, the expected intensity of the  $E3$  branch in  $^{213}\text{Ra}$

would be  $\sim 2\%$ . The experimental limit on the intensity of the expected 840 keV  $E3$  transition is  $< 2.1\%$ , relative to the 323-keV  $E1$  transition intensity. Thus, the expected  $E3$  intensity is at our detection limit.

Moving up the level scheme, the semiempirical shell-model calculations predict the occurrence of the  $J^\pi = 25/2^+$  state (which was missed in the simplified calculations) and place it close to the experimentally observed energy of  $3065 + \Delta$  keV. The level arises predominantly from the coupling of the  $\nu f_{5/2}^{-1}$  neutron hole to valence protons in the  $\pi(h_{9/2}^5 i_{13/2}^1)_{10+}$  configuration.

The interpretation of the higher-spin positive-parity levels became relatively straight forward once it was recognized that the semiempirical shell model calculations for the  $\pi(h_{9/2}^5 i_{13/2}^1) \otimes \nu p_{1/2}^{-1}$  configuration are underesti-

TABLE V. Configuration assignments in  $^{213}\text{Ra}$ .

$E_x$ (keV)	$J^\pi$	Nominal Configuration	$E_{\text{calc}}$ (keV)	$E_{\text{calc}} - E_x$ (keV)
0	1/2 <sup>-</sup>	$\pi(h_{9/2}^6)_{0+} \otimes \nu p_{1/2}^{-1}$	385	385
546	5/2 <sup>-</sup>	$\pi(h_{9/2}^6)_{0+} \otimes \nu f_{5/2}^{-1}$	1105	559
1609	9/2 <sup>-</sup>	$\pi(h_{9/2}^6)_{4+} \otimes \nu p_{1/2}^{-1}$	1741	132
1770	13/2 <sup>-</sup>	$\pi(h_{9/2}^6)_{6+} \otimes \nu p_{1/2}^{-1}$	1862	92
1770 + $\Delta$	17/2 <sup>-</sup>	$\pi(h_{9/2}^6)_{8+} \otimes \nu p_{1/2}^{-1}$	1881	111 - $\Delta$
2287 + $\Delta$	21/2 <sup>-</sup>	$\pi(h_{9/2}^6)_{8+} \otimes \nu f_{5/2}^{-1}$	2548	261 - $\Delta$
2610 + $\Delta$	23/2 <sup>+</sup>	$\pi[(h_{9/2}^5)_{9/2}i_{13/2}]_{11-} \otimes \nu p_{1/2}^{-1}$	2732 <sup>a</sup>	122 - $\Delta$
3065 + $\Delta$	25/2 <sup>+</sup>	$\pi[(h_{9/2}^5)_{9/2}i_{13/2}]_{10-} \otimes \nu f_{5/2}^{-1}$	3092 <sup>a</sup>	-27 - $\Delta$
3136 + $\Delta$	25/2 <sup>-</sup>	$\pi(h_{9/2}^6)_{12+} \otimes \nu p_{1/2}^{-1}$	3008	-128 - $\Delta$
3281 + $\Delta$	25/2 <sup>-</sup>	$\pi[(h_{9/2}^5)_{17/2}f_{7/2}]_{12+} \otimes \nu p_{1/2}^{-1}$	3259	-22 - $\Delta$
3340 + $\Delta$	27/2 <sup>+</sup>	$\pi[(h_{9/2}^5)_{9/2}i_{13/2}]_{11-} \otimes \nu f_{5/2}^{-1}$	3590	110 - $\Delta$
3345 + $\Delta$	25/2 <sup>-</sup>	$\pi(h_{9/2}^6)_{10+} \otimes \nu f_{5/2}^{-1}$	3426	81 - $\Delta$
3433 + $\Delta$	27/2 <sup>-</sup>	$\pi[(h_{9/2}^5)_{21/2}f_{7/2}]_{13+} \otimes \nu p_{1/2}^{-1}$	3379	-54 - $\Delta$
3441 + $\Delta$	29/2 <sup>-</sup>	$\pi[(h_{9/2}^5)_{21/2}f_{7/2}]_{14+} \otimes \nu p_{1/2}^{-1}$	3389	-52 - $\Delta$
3863 + $\Delta$	27/2 <sup>+</sup>	$\pi[(h_{9/2}^5)_{13/2}i_{13/2}]_{13-} \otimes \nu p_{1/2}^{-1}$	3793 <sup>a</sup>	-70 - $\Delta$
3878 + $\Delta$	29/2 <sup>+</sup>	$\pi[(h_{9/2}^5)_{17/2}i_{13/2}]_{14-} \otimes \nu p_{1/2}^{-1}$	3961 <sup>a</sup>	83 - $\Delta$
4007 + $\Delta$	31/2 <sup>+</sup>	$\pi[(h_{9/2}^5)_{17/2}i_{13/2}]_{15-} \otimes \nu p_{1/2}^{-1}$	3969 <sup>a</sup>	-38 - $\Delta$
4048 + $\Delta$	33/2 <sup>+</sup>	$\pi[(h_{9/2}^5)_{21/2}i_{13/2}]_{16-} \otimes \nu p_{1/2}^{-1}$	4115 <sup>a</sup>	67 - $\Delta$
-	35/2 <sup>+</sup>	$\pi[(h_{9/2}^5)_{21/2}i_{13/2}]_{16-} \otimes \nu p_{1/2}^{-1}$	4122 <sup>a</sup>	-
-	37/2 <sup>+</sup>	$\pi[(h_{9/2}^5)_{21/2}i_{13/2}]_{16-} \otimes \nu p_{1/2}^{-1}$	4848 <sup>a</sup>	-
-	35/2 <sup>+</sup>	$\pi[(h_{9/2}^5)_{21/2}i_{13/2}]_{16-} \otimes \nu f_{5/2}^{-1}$	4467	-
-	37/2 <sup>+</sup>	$\pi[(h_{9/2}^5)_{21/2}i_{13/2}]_{16-} \otimes \nu f_{5/2}^{-1}$	4472	-

<sup>a</sup> Calculated energy of this state has been increased by 250 keV as discussed in the text.

mating the level energies by about 250 keV. Once the calculations are adjusted upwards by this amount, the predicted and experimental levels come into good agreement. Figure 14 and Table V show the calculated states from the  $\pi[(h_{9/2}^5)i_{13/2}] \otimes \nu p_{1/2}^{-1}$  and  $\pi[(h_{9/2}^5)i_{13/2}] \otimes \nu f_{5/2}^{-1}$  configurations with this shift included. It thus becomes evident that the lower  $J^\pi = 27/2^+$  state is associated with a dominant configuration of  $\pi[(h_{9/2}^5)_{9/2}i_{13/2}]_{11} \otimes \nu f_{5/2}^{-1}$ , and the upper one with  $\pi[(h_{9/2}^5)_{13/2}i_{13/2}]_{13} \otimes \nu p_{1/2}^{-1}$ . The  $J^\pi = 27/2^+$  states are no doubt mixed, so decays of the  $J^\pi = 27/2^+$  states to the  $J^\pi = 25/2^+$  state, which is predominantly  $\pi(h_{9/2}^5)_{11/2}i_{13/2} \otimes \nu f_{5/2}^{-1}$ , are likely originating from  $M1$  transitions between alternative spin couplings of this configuration in the initial and final states. Such transitions are relatively strong, which may explain why this part of the level scheme is decoupled from the neighboring states.

A single  $J^\pi = 29/2^+$  state is observed that can be associated with a dominant  $\pi[(h_{9/2}^5)_{17/2}i_{13/2}]_{14} \otimes \nu p_{1/2}^{-1}$  configuration. An  $E1$  decay to the  $J^\pi = 29/2^-$  level can compete with  $M1$  and/or  $E2$  decays to the positive parity states, which for the dominant configurations are either forbidden (as is the case for the first  $J^\pi = 27/2^+$  state at 3340 +  $\Delta$  keV) or suppressed by low transition energy and mid-shell cancellation between states of the seniority-two  $\pi(h_{9/2}^5)$  configuration (as is the case for the second  $J^\pi = 27/2^+$  state at 3863 +  $\Delta$  keV) [35]. The  $J^\pi = 31/2^+$

state with dominant configuration  $\pi[(h_{9/2}^5)_{17/2}i_{13/2}]_{15} \otimes \nu p_{1/2}^{-1}$  is predicted just above the  $J^\pi = 29/2^+$  state, in agreement with experiment.

The isomeric  $J^\pi = 33/2^+$  level is also associated with the same configuration, with dominant coupling  $\pi[(h_{9/2}^5)_{21/2}i_{13/2}]_{16} \otimes \nu p_{1/2}^{-1}$ . The retarded 170-keV  $E2$  transition to the  $J^\pi = 29/2^+$  state is thus associated with  $\pi[(h_{9/2}^5)_{21/2}] \rightarrow \pi[(h_{9/2}^5)_{17/2}]$ , which is inhibited (0.005 W.u. in  $^{213}\text{Ra}$ ) because it represents a transition between states of the same seniority with a half-filled orbit [35]. The equivalent decay in  $^{213}\text{Fr}$  has a strength of  $\sim 0.05$  W.u.

The 41-keV  $M1$  transition to the  $J^\pi = 31/2^+$  state can be attributed to a small  $\pi[(h_{9/2}^5)_{21/2}i_{13/2}]_{15} \otimes \nu p_{1/2}^{-1}$  component in the  $J^\pi = 31/2^+$  level; the  $\pi[(h_{9/2}^5)_{21/2}i_{13/2}]_{16} \rightarrow \pi[(h_{9/2}^5)_{21/2}i_{13/2}]_{15}$  transition has a strength of about 0.1 W.u., so only small admixtures are required to account for the observed transition strength of  $\sim 10^{-4}$  W.u.

A 606-keV transition from the  $J^\pi = 33/2^+$  isomer to the  $J^\pi = 29/2^-$  level is also observed, which can have mixed  $M2 + E3$  multipolarity. We have shown the experimental transition strengths for the extremes of pure  $M2$  and pure  $E3$  multipolarity in Table IV. Assuming pure multipolarity, the  $M2$  strength is very weak whereas the  $E3$  is unrealistically strong. The nomi-

nal configuration change,  $\pi[(h_{9/2}^5)_{21/2}i_{13/2}]_{16} \otimes \nu p_{1/2}^{-1} \rightarrow \pi[(h_{9/2}^5)_{21/2}f_{7/2}]_{14} \otimes \nu p_{1/2}^{-1}$  does not permit an  $M2$  transition, but does allow an  $E3$  transition. The expected  $E3$  strength can be scaled from the parent  $\pi[(h_{9/2}^5)_{21/2}i_{13/2}]_{17^-} \rightarrow \pi[(h_{9/2}^5)_{21/2}i_{13/2}]_{14^+}$  transition in  $^{214}\text{Ra}$  to give an expected strength of  $\sim 10$  W.u. (The scale factor is given by the ratio of Racah coefficients,  $[W(\frac{21}{2} \frac{13}{2} 14^- 3; 16\frac{7}{2})/W(\frac{21}{2} \frac{13}{2} 14^- 3; 17\frac{7}{2})]^2$ .) Thus an observed transition strength of 36 W.u. for a pure  $E3$  transition (Table IV) is unrealistic, and an  $M2$  component must be present.

An  $M2$  component in the 606-keV transition could be explained by small mixing of the configuration  $\pi[h_{9/2}^4 f_{7/2} i_{13/2}]_{16^-} \otimes \nu p_{1/2}^{-1}$  in the  $J^\pi = 33/2^+$  level. Although this configuration is not needed to explain the yrast spectroscopy of  $^{213}\text{Ra}$ , the parent proton configurations  $\pi[h_{9/2}^5 i_{13/2}]$  and  $\pi[h_{9/2}^4 f_{7/2} i_{13/2}]$  are identified in  $^{214}\text{Ra}$ . Only a small contribution is needed because the allowed  $M2$  transition  $\pi i_{13/2} \rightarrow \pi h_{9/2}$  has a strength of the order of 1 W.u. [36].

Theory and experiment can be brought into harmony if the 606-keV transition has mixed multipolarity with mixing ratio  $|\delta(E3/M2)| \sim 0.7$ .

It is not clear why the upward shift of  $\sim 250$  keV is necessary for the  $\pi[(h_{9/2}^5)_{13/2}] \otimes \nu p_{1/2}^{-1}$  configuration. However, it has to be kept in mind that the semiempirical shell model calculations do not include configuration mixing. Another consideration is that the empirical single-particle energies and two-body residual interactions include octupole-coupled components due to the octupole vibration of the  $^{208}\text{Pb}$  core [37]. Such components could be double counted in the evaluation of more complex configurations, or affected by Pauli-blocking. Overall, given their simplicity, the agreement of the semiempirical single-configuration calculations with experiment at the level of a few hundred keV is rather remarkable.

A number of additional  $\gamma$ -ray transitions were observed in the experiment that must originate from higher-excited states in  $^{213}\text{Ra}$ , but we were not able to place them firmly in the level scheme. The calculations predict a  $J^\pi = 35/2^+$  state within 20 keV of the  $J^\pi = 33/2^+$  state for which we could not find firm experimental evidence. An  $M1$  transition between the proposed configurations of the  $J^\pi = 33/2^+$  and  $J^\pi = 35/2^+$  states would not be isomeric unless its energy was less than about 20 keV. The strongest observed line above the  $J^\pi = 33/2^+$  isomer has an energy of 459-keV and is likely an  $M1$  transition. Should this transition be placed above the proposed but unobserved low-energy  $M1$  transition between the  $J^\pi = 35/2^+$  and  $J^\pi = 33/2^+$  states, it would de-populate a  $J^\pi = 37/2^+$  state at an excitation energy of about 4.5 MeV, for which there is a predicted candidate state with configuration  $\pi[(h_{9/2}^5)_{21/2}i_{13/2}]_{17} \otimes \nu f_{5/2}^{-1}$  at an energy of 4472 keV.

In summary, we are able to assign dominant configurations to the observed states in  $^{213}\text{Ra}$  up to the  $J^\pi = 33/2^+$  isomer, obtaining reasonable agreement with

the level energies and at least a qualitative understanding of the observed electromagnetic transitions.

### 3. $^{212}\text{Ra}$ Calculation

At the level of the weak-coupling model discussed above in relation to  $^{213}\text{Ra}$ , an equivalent assumption for  $^{212}\text{Ra}$  is that the two neutron holes couple to spin-parity  $J^\pi = 0^+$  such that the level scheme of  $^{212}\text{Ra}$  then should resemble that of  $^{214}\text{Ra}$ . A weak-coupling model calculation along these lines was performed by Kohno *et al.* [13]. A comparison of the level schemes of  $^{212}\text{Ra}$  and  $^{214}\text{Ra}$  suggests equivalence of the following yrast states:  $J^\pi = 0^+$ ,  $J^\pi = 6^+$ ,  $J^\pi = 8^+$ ,  $J^\pi = 11^-$ , and  $J^\pi = 17^-$ , along with the second  $J^\pi = 8^+$  state. Otherwise, more detailed conclusions cannot be drawn. In fact, when it comes to the semiempirical shell model calculations, the two neutron holes in  $^{212}\text{Ra}$  open up a larger array of available configurations, including two-proton and two-neutron excitations from the lowest energy configuration,  $\pi h_{9/2}^6 \otimes \nu p_{1/2}^{-2}$ . Of the many possible combinations that were examined, only the nine most relevant to the observed states will be discussed. These are:

- $\pi h_{9/2}^6 \otimes \nu p_{1/2}^{-2}$
- $\pi h_{9/2}^6 \otimes \nu(p_{1/2}^{-1} f_{5/2}^{-1})$
- $\pi(h_{9/2}^5 f_{7/2}) \otimes \nu p_{1/2}^{-2}$
- $\pi(h_{9/2}^5 f_{7/2}) \otimes \nu(p_{1/2}^{-1} f_{5/2}^{-1})$
- $\pi(h_{9/2}^5 i_{13/2}) \otimes \nu p_{1/2}^{-2}$
- $\pi(h_{9/2}^5 i_{13/2}) \otimes \nu(p_{1/2}^{-1} f_{5/2}^{-1})$
- $\pi(h_{9/2}^4 f_{7/2} i_{13/2}) \otimes \nu p_{1/2}^{-2}$
- $\pi(h_{9/2}^4 i_{13/2}^2) \otimes \nu p_{1/2}^{-2}$
- $\pi(h_{9/2}^4 i_{13/2}^2) \otimes \nu(p_{1/2}^{-1} f_{5/2}^{-1})$

The semiempirical shell model calculations for  $^{212}\text{Rn}$  are compared with experiment in Fig. 15. As usual, the energies of the low-seniority, low-excitation states, particularly the ground state and first-excited  $J^\pi = 2^+$  state, are over-estimated by the calculation. The ground-state configuration is nominally  $\pi h_{9/2}^6 \otimes \nu p_{1/2}^{-2}$ . Like in  $^{213}\text{Ra}$ , the first-excited state is associated with the excitation of a neutron hole,  $\nu p_{1/2}^{-1} \rightarrow \nu f_{5/2}^{-1}$ . However there is evidently considerable configuration mixing as the lowest calculated  $J^\pi = 2^+$  state, associated with  $\pi h_{9/2}^6 \otimes \nu(p_{1/2}^{-1} f_{5/2}^{-1})$ , is approximately 600 keV higher than the experimental energy.

By contrast, the  $J^\pi = 6^+$  and  $J^\pi = 8^+$  states are well explained by the pure  $\pi h_{9/2}^6 \otimes \nu(p_{1/2}^{-2})$  configuration. The second  $J^\pi = 8^+$  state is well explained by the

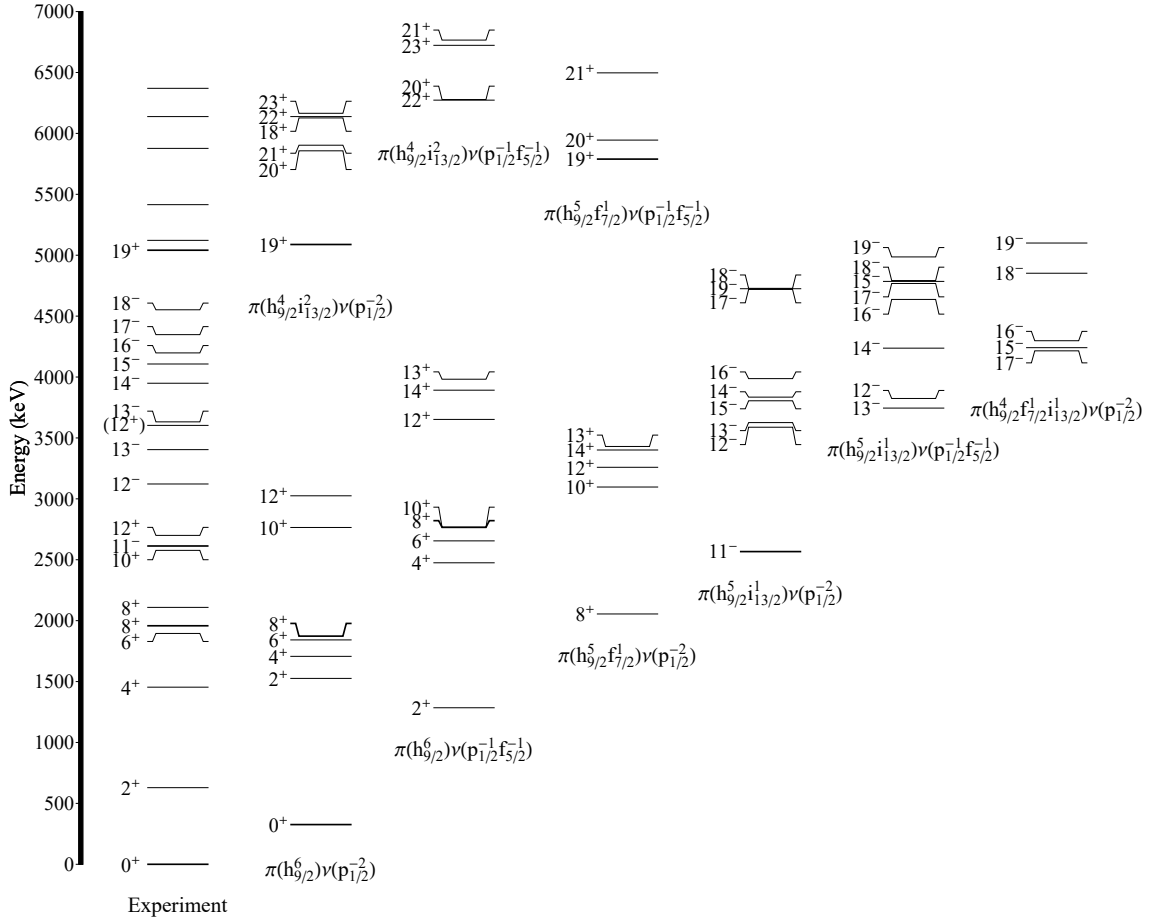


FIG. 15. Comparison between the experimental level scheme of  $^{212}\text{Ra}$  and predictions from the semiempirical shell-model calculations described in the text. Experimental data are shown on the left, while predictions for selected configurations are shown to the right. For the  $J > 19$  levels, no spin or parity assignments have been made.

pure  $\pi(h_{9/2}^5 f_{7/2}) \otimes \nu p_{1/2}^{-2}$  configuration, with the same  $\pi f_{7/2}$  proton excitation creating the corresponding state in  $^{214}\text{Ra}$  [8].

The  $J^\pi = 11^-$  state in  $^{212}\text{Ra}$  is produced by the same  $\pi i_{13/2}$  proton excitation as in  $^{214}\text{Ra}$ , and is also analogous to the  $J^\pi = 23/2^+$  yrast state in  $^{213}\text{Ra}$ . In each of these isotopes the related states lie at an excitation energy of approximately 2600 keV and are isomeric due to the change in configuration, which includes a parity change. In  $^{214}\text{Ra}$ , two  $E3$  transitions to the  $J^\pi = 8^+$  states carry 100% of the decay intensity from the  $J^\pi = 11^-$  state, while in  $^{212}\text{Ra}$  a 36-keV  $E1$  transition to the  $J^\pi = 10^+$  state is the dominant branch, with the two  $E3$  transitions to the  $J^\pi = 8^+$  states sharing half of the decay intensity. The transition strengths in  $^{214}\text{Ra}$  are 3.1(1) W.u for the nominal  $\pi(h_{9/2}^5 i_{13/2}) \rightarrow h_{9/2}^6$  transition and 21.7(6) W.u.

for the nominal  $\pi(h_{9/2}^5 i_{13/2}) \rightarrow \pi(h_{9/2}^5 f_{7/2})$  transition. In  $^{212}\text{Ra}$ , the  $E3$  strengths have decreased slightly but their proportionality has remained the same, namely 2.1(6) W.u for  $\pi i_{13/2} \rightarrow \pi h_{9/2}$  and 14.4(3) W.u. for  $\pi i_{13/2} \rightarrow \pi f_{7/2}$ . This similarity between  $^{214}\text{Ra}$  and  $^{212}\text{Ra}$  supports the configuration assignments for the two  $J^\pi = 8^+$  states and the  $J^\pi = 11^-$  isomer.

Compared with  $^{214}\text{Ra}$ , the  $J^\pi = 10^+$  state in  $^{212}\text{Ra}$  has been driven below the  $J^\pi = 11^-$  state; the same behavior has been observed in the  $N = 124$  isotope,  $^{210}\text{Rn}$  [19]. The calculations predict three  $J^\pi = 10^+$  states due to the  $\pi h_{9/2}^6 \otimes \nu p_{1/2}^{-2}$ ,  $\pi h_{9/2}^6 \otimes \nu(p_{1/2}^{-1} f_{5/2}^{-1})$  and  $\pi(h_{9/2}^5 f_{7/2}) \otimes \nu p_{1/2}^{-2}$  configurations, all higher in energy than the  $J^\pi = 11^-$  state. However, if mixing were taken into account, it can be expected that the yrast  $J^\pi = 10^+$  state would

be pushed down in energy and could come below the  $J^\pi = 11^-$  level, as is observed.

Above the  $J^\pi = 11^-$  state, it becomes difficult to match the semiempirical shell-model configurations with the observed excited states. Nevertheless, the experimental states between  $J^\pi = 11^-$  and  $J^\pi = 18^-$  appear to be associated with three dominant negative-parity configurations,  $\pi(h_{9/2}^5 i_{13/2}) \otimes \nu p_{1/2}^{-2}$ ,  $\pi(h_{9/2}^5 i_{13/2}) \otimes \nu(p_{1/2}^{-1} f_{5/2}^{-1})$ , and  $\pi(h_{9/2}^4 f_{7/2} i_{13/2}) \otimes \nu p_{1/2}^{-2}$ . The high level density implies that a high level of configuration mixing may be required to describe this portion of the level scheme. The incremental sequence of negative-parity states from  $J^\pi = 13^-$  to  $J^\pi = 18^-$  means that the  $J^\pi = 17^-$  state, which is isomeric in  $^{214}\text{Ra}$ , is no longer an isomer in  $^{212}\text{Ra}$ . More specifically, in  $^{214}\text{Ra}$ , the yrast  $J^\pi = 17^-$  state decays via an enhanced  $E3$  transition to the yrast  $J^\pi = 14^+$  state. The  $J^\pi = 17^-$  level is nominally associated with the  $\pi(h_{9/2}^5 i_{13/2})$  configuration and includes mixing with  $\pi(h_{9/2}^4 f_{7/2} i_{13/2})$ , which can be included using the multiparticle octupole coupling model approach [6, 8, 38]. In  $^{212}\text{Ra}$ , however, the yrast  $J^\pi = 14^+$  state is not observed and the  $J^\pi = 17^-$  state is not isomeric, decaying via an  $M1$  transition to  $J^\pi = 16^-$ .

The  $J^\pi = 19^+$  isomer can be identified with the  $\pi(h_{9/2}^4 i_{13/2}^2) \otimes \nu(p_{1/2}^{-2})$  configuration. It decays via an  $E1$  transition to the  $J^\pi = 18^-$  state with a typical  $E1$  strength of  $6.7(8) \times 10^{-8}$  W.u.. A search was made for possible  $E3$  transitions from this state, but none could be found. In most cases, the strong  $E3$  transitions take place between the maximal spin couplings of the initial and final configurations, whereas, in this case in  $^{212}\text{Ra}$ , the angular momentum coupling of the initial and final states inhibits  $E3$  transitions.

It is noteworthy that the corresponding  $J^\pi = 19^+$  state is not observed in  $^{214}\text{Ra}$ , and instead the  $J^\pi = 18^+$  state of the  $\pi(h_{9/2}^4 i_{13/2}^2)$  configuration is observed. The addition of the two neutron holes leads to a considerable re-ordering of the spin sequence within the proton configuration such that the  $J^\pi = 18^+$  level does not appear in the experimental level scheme of  $^{212}\text{Ra}$ . The calculation predicts that it is pushed above the  $J^\pi = 21^+$  state. Such relatively small changes in the level ordering can have a profound influence on the experimentally accessi-

ble near-yrast level sequence and decay scheme.

Several states lying above  $J^\pi = 19^+$  were observed but have no firm spin-parity assignments.

## V. CONCLUSIONS

The radium isotopes with one and two neutron holes in the  $N = 126$  closed shell have been investigated experimentally,  $^{213}\text{Ra}$  to spins of about  $33/2\hbar$  and excitation energies of about 4 MeV, and  $^{212}\text{Ra}$  to spins of about  $20\hbar$  and excitation energies of about 6 MeV. Knowledge of  $^{213}\text{Ra}$  has been extended beyond the  $J^\pi = 17/2^-, \tau = 3$ -ms metastable state. Two new isomers with  $J^\pi = 23/2^+$ ,  $\tau = 27(3)$  ns and  $J^\pi = 33/2^+, \tau = 50(3)$  ns have been identified. In  $^{212}\text{Ra}$ , an isomer with  $J^\pi = 19^+$  and  $\tau = 31(3)$  ns has been identified.

Semiempirical shell-model calculations give a satisfactory description of the excitation energies and decay rates in  $^{213}\text{Ra}$  up to the  $J^\pi = 33/2^+$  isomer. A reasonable account can also be given for  $^{212}\text{Ra}$ . Large-basis shell-model calculations are now feasible in many regions of the nuclear chart, however the region near  $^{208}\text{Pb}$  has been largely neglected to date; it would be timely to re-visit this region. The success of the semiempirical shell-model calculations suggests that deeper insights into the evolution of nuclear structure and the onset of collectivity could be gained by developing a more sophisticated theory that includes configuration interactions.

## ACKNOWLEDGMENTS

The authors are grateful to the academic and technical staff of the Department of Nuclear Physics (Australian National University) and the Heavy Ion Accelerator Facility for their continued support. This research was supported in part by the Australian Research Council grants numbers DP120101417, DP130104176, DP140102986, DP140103317, and FT100100991. A.A. and M.S.M.G. acknowledge support of the Australian Government Research Training Program.

- 
- [1] M. G. Mayer, Phys. Rev. **74**, 235 (1948).
  - [2] L. Coraggio, A. Covello, A. Gargano, and N. Itaco, Phys. Rev. C **80**, 021305 (2009).
  - [3] A. Gargano, L. Coraggio, A. Covello, and N. Itaco, Journal of Physics: Conference Series **168**, 012013 (2009).
  - [4] G. D. Dracoulis, G. J. Lane, A. P. Byrne, P. M. Davidson, T. Kibédi, P. Nieminen, K. H. Maier, H. Watanabe, and A. N. Wilson, Phys. Rev. C **77**, 034308 (2008).
  - [5] S. Bayer, A. P. Byrne, G. D. Dracoulis, A. M. Baxter, T. Kibédi, and F. G. Kondev, Nuclear Physics A **694**, 3 (2001).
  - [6] A. E. Stuchbery, G. D. Dracoulis, A. P. Byrne, and A. R. Poletti, Nuclear Physics A **486**, 397 (1988).
  - [7] A. P. Byrne, G. D. Dracoulis, C. Fahlander, H. Hübel, A. R. Poletti, A. E. Stuchbery, J. Gerl, R. F. Davie, and S. J. Poletti, Nuclear Physics A **448**, 137 (1986).
  - [8] A. E. Stuchbery, G. D. Dracoulis, T. Kibédi, A. P. Byrne, B. Fabricius, A. R. Poletti, G. J. Lane, and A. M. Baxter, Nuclear Physics A **548**, 159 (1992).
  - [9] A. E. Stuchbery, G. D. Dracoulis, T. Kibédi, A. P. Byrne, B. Fabricius, A. R. Poletti, G. J. Lane, and A. M. Baxter, Nuclear Physics A **641**, 401 (1998).

- [10] G. D. Dracoulis, F. Riess, A. M. Baxter, and A. E. Stuchbery, *Journal of Physics G: Nuclear and Particle Physics* **17**, 1795 (1991).
- [11] M. Aiche, A. Chevallier, J. Chevallier, S. Hulne, S. Khazrouni, N. Schulz, and J. C. Sens, *Journal of Physics G: Nuclear Physics* **14**, 1191 (1988).
- [12] D. G. Raich, H. R. Bowman, R. E. Eppley, J. O. Rasmussen, and I. Rezanka, *Zeitschrift für Physik A Atoms and Nuclei* **279**, 301 (1976).
- [13] T. Kohno, M. Adachi, S. Fukuda, M. Taya, M. Fukuda, H. Taketani, Y. Gono, M. Sugawara, and Y. Ishikawa, *Phys. Rev. C* **33**, 392 (1986).
- [14] T. Kibédi, T. W. Burrows, M. B. Trzhaskovskaya, P. M. Davidson, and C. W. Nestor Jr., *Nuclear Instruments and Methods in Physics Research Section A: Accelerators, Spectrometers, Detectors and Associated Equipment* **589**, 202 (2008).
- [15] J. A. Bearden, *Rev. Mod. Phys.* **39**, 78 (1967).
- [16] V. Margerin, G. J. Lane, G. D. Dracoulis, N. Palalani, M. L. Smith, and A. E. Stuchbery, *Phys. Rev. C* **93**, 064309 (2016).
- [17] M. Morinaga and T. Yamazaki, *In-Beam Gamma-Ray Spectroscopy* (North Holland, Amsterdam, 1976) p. 148.
- [18] G. Neyens, R. Nouwen, G. S'heeren, M. V. D. Bergh, and R. Coussément, *Nuclear Physics A* **555**, 629 (1993).
- [19] A. R. Poletti, A. P. Byrne, G. D. Dracoulis, T. Kibédi, and P. M. Davidson, *Nuclear Physics A* **756**, 83 (2005).
- [20] P. M. Davidson, G. D. Dracoulis, A. P. Byrne, T. Kibédi, B. Fabricius, A. M. Baxter, A. E. Stuchbery, A. R. Poletti, and K. J. Schiffer, *Nuclear Physics A* **560**, 822 (1993).
- [21] A. R. Poletti, G. D. Dracoulis, S. J. Poletti, A. P. Byrne, A. E. Stuchbery, and J. Gerl, *Nuclear Physics A* **442**, 153 (1985).
- [22] E. Caurier, M. Rejmund, and H. Grawe, *Phys. Rev. C* **67**, 054310 (2003).
- [23] A. R. Poletti, G. D. Dracoulis, A. P. Byrne, A. E. Stuchbery, B. Fabricius, T. Kibédi, and P. M. Davidson, *Nuclear Physics A* **615**, 95 (1997).
- [24] A. R. Poletti, G. D. Dracoulis, A. P. Byrne, A. E. Stuchbery, B. Fabricius, T. Kibédi, and P. M. Davidson, *Nuclear Physics A* **665**, 318 (2000).
- [25] A. R. Poletti, G. D. Dracoulis, A. P. Byrne, and A. E. Stuchbery, *Nuclear Physics A* **473**, 595 (1987).
- [26] S. Bayer, A. P. Byrne, G. D. Dracoulis, A. M. Baxter, T. Kibédi, F. G. Kondev, S. M. Mullins, and T. R. McGoram, *Nuclear Physics A* **650**, 3 (1999).
- [27] A. Poletti, G. Dracoulis, C. Fahlander, and A. Byrne, *Nuclear Physics A* **440**, 118 (1985).
- [28] G. D. Dracoulis, P. M. Davidson, A. P. Byrne, B. Fabricius, T. Kibédi, A. M. Baxter, A. E. Stuchbery, A. R. Poletti, and K. J. Schiffer, *Nuclear Physics A* **520**, c353 (1990), nuclear Structure in the Nineties.
- [29] A. E. Stuchbery, G. D. Dracoulis, A. P. Byrne, S. J. Poletti, and A. R. Poletti, *Nuclear Physics A* **482**, 692 (1988).
- [30] G. D. Dracoulis, A. P. Byrne, A. E. Stuchbery, R. A. Bark, and A. R. Poletti, *Nuclear Physics A* **467**, 305 (1987).
- [31] A. P. Byrne, G. J. Lane, G. D. Dracoulis, B. Fabricius, T. Kibédi, A. E. Stuchbery, A. M. Baxter, and K. J. Schiffer, *Nuclear Physics A* **567**, 445 (1994).
- [32] T. T. S. Kuo and G. H. Herling, *Two-Particle and Two-Hole States in the Pb Region. NRL Report No. 2258* (Naval Research Laboratory, Washington, 1971).
- [33] R. D. Lawson, *Theory of the Nuclear Shell Model* (Clarendon, Oxford, 1980) p. 304.
- [34] M. Morinaga and T. Yamazaki, *In-Beam Gamma-Ray Spectroscopy* (North Holland, Amsterdam, 1976) p. 148.
- [35] A. de Shalit and I. Talmi, *Nuclear Shell Theory* (Academic Press, New York, 1963) p. 315.
- [36] O. J. Roberts, C. R. Nită, A. M. Bruce, N. Mărginean, D. Bucurescu, D. Deleanu, D. Filipescu, N. M. Florea, I. Gheorghe, D. Ghiță, T. Glodariu, R. Lica, R. Mărginean, C. Mihai, A. Negret, T. Sava, L. Stroe, R. Șuvăilă, S. Toma, T. Alharbi, T. Alexander, S. Aydin, B. A. Brown, F. Browne, R. J. Carroll, K. Mulholland, Z. Podolyák, P. H. Regan, J. F. Smith, M. Smolen, and C. M. Townsley, *Phys. Rev. C* **93**, 014309 (2016).
- [37] I. Hamamoto, *Physics Reports* **10**, 63 (1974).
- [38] S. J. Poletti, G. D. Dracoulis, A. R. Poletti, A. P. Byrne, A. E. Stuchbery, and J. Gerl, *Nuclear Physics A* **448**, 189 (1986).

# Bibliography

---

- [And72] Andreev, D. *Instruments and Experimental Techniques*, 15:1358, 1972.
- [Ben07] Bengtsson, R. and Moller, P. Nuclear physics: A non-disappearing magic trick. *Nature*, 449:411, 413, 2007.
- [Bla71] Black, J.N., McHarris, W.C., and Kelly, W.H. E6 and M5 transitions observed in  $^{53m}\text{Fe}$  decay. *Phys. Rev. Lett.*, 26:451–454, 1971.
- [Bla75] Black, J.N., et al. Decays of the  $f_{7/2}$  isomers  $^{53}\text{Fe}^g$  and  $^{53}\text{Fe}^m$ . *Phys. Rev. C*, 11:939–951, 1975.
- [Bla93] Blaauw, M. The use of sources emitting coincident  $\gamma$ -rays for determination of absolute efficiency curves of highly efficient Ge detectors. *Nuclear Instruments and Methods in Physics Research Section A: Accelerators, Spectrometers, Detectors and Associated Equipment*, 332(3):493 – 500, 1993.
- [Blu85] Blunden, P., Castel, B., and Toki, H. Quenching of magnetic transitions as an angular momentum effect. *Nuclear Physics A*, 440(4):647 – 652, 1985.
- [Bro77] Brown, B., Arima, A., and McGrory, J. E2 core-polarization charge for nuclei near  $^{16}\text{O}$  and  $^{40}\text{Ca}$ . *Nuclear Physics A*, 277(1):77 – 108, 1977.
- [Bro80] Brown, B.A., Chung, W., and Wildenthal, B.H. Inelastic scattering E4 transition probabilities in the 0d, 1s shell. *Phys. Rev. C*, 21:2600–2612, 1980.
- [Bro11] Brown, B.A. and Rae, W.D.M. E6 gamma decay. *AIP Conference Proceedings*, 1355(1):145–152, 2011.

- 
- [Bro14] Brown, B. and Rae, W. The shell-model code NuShellX@MSU. *Nuclear Data Sheets*, 120(Supplement C):115 – 118, 2014.
  - [Bro17] Brown, B.A. and Rae, W.D.M. E6 transitions in nuclei. *Unpublished Communication*, 2017.
  - [Bur06] Burrows, T. Nuclear data sheets for A = 48. *Nuclear Data Sheets*, 107(7):1747 – 1922, 2006.
  - [Bur07] Burrows, T. Nuclear data sheets for A = 47. *Nuclear Data Sheets*, 108(5):923 – 1056, 2007.
  - [Bur08] Burrows, T. Nuclear data sheets for A = 49. *Nuclear Data Sheets*, 109(8):1879 – 2032, 2008.
  - [Cas84] Castel, B. and Zamick, L. Effects beyond first-order perturbation theory in the polarization charges for E4 transitions. *Zeitschrift für Physik A Atoms and Nuclei*, 315(1):99–101, 1984.
  - [Che11] Chen, J., Singh, B., and Cameron, J.A. Nuclear data sheets for A = 44. *Nuclear Data Sheets*, 112(9):2357 – 2495, 2011.
  - [Coc71] Cochavi, S. and Nagatani, K. Study of low-lying states in  $^{53}\text{Fe}$  by the reaction  $^{50}\text{Cr}(\alpha, n\gamma)^{53}\text{Fe}$ . *Phys. Rev. C*, 4:2083–2089, 1971.
  - [DL81] De Leo, R., et al. Proton excitation of  $^{24}\text{Mg}$ ,  $^{26}\text{Mg}$ , and  $\gamma$  bands. *Phys. Rev. C*, 23:1355–1363, 1981.
  - [Don14] Dong, Y. and Junde, H. Nuclear data sheets for A = 54. *Nuclear Data Sheets*, 121(Supplement C):1 – 142, 2014.
  - [Don15] Dong, Y. and Junde, H. Nuclear data sheets for A = 52. *Nuclear Data Sheets*, 128(Supplement C):185 – 314, 2015.
  - [Dra08] Dracoulis, G., et al. High-spin isomers in  $^{212}\text{Rn}$  in the region of triple neutron core-excitations. *submitted to Physical Review C*, 662(1):19 – 25, 2008.

- 
- [Ele11] Elekes, Z., Timar, J., and Singh, B. Nuclear data sheets for A = 50. *Nuclear Data Sheets*, 112(1):1 – 131, 2011.
  - [End79] Endt, P. Strengths of gamma-ray transitions in A = 45–90 nuclei. *Atomic Data and Nuclear Data Tables*, 23(6):547 – 585, 1979.
  - [Gad05] Gadea, A., et al. Hindered E4 decay of the 12<sup>+</sup> yrast trap in <sup>52</sup>Fe. *Physics Letters B*, 619(1):88 – 94, 2005.
  - [Gav80] Gavron, A. Statistical model calculations in heavy ion reactions. *Phys. Rev. C*, 21:230–236, 1980.
  - [Gee76] Geesaman, D.F. *A study of the spin gap isomers in <sup>52</sup>Fe, <sup>53</sup>Fe, and <sup>54</sup>Co*. 1976.
  - [Geh77] Gehrke, R., Helmer, R., and Greenwood, R. Precise relative  $\gamma$ -ray intensities for calibration of Ge semiconductor detectors. *Nuclear Instruments and Methods*, 147(2):405 – 423, 1977.
  - [Gla67] Glaudemans, P., Brussaard, P., and Wildenthal, B. Two-body matrix elements from a modified surface delta interaction. *Nuclear Physics A*, 102(3):593 – 601, 1967.
  - [Glo75] Gloeckner, D.H. and Lawson, R.D. E6 transition in <sup>53</sup>Fe. *Phys. Rev. C*, 11:1832–1835, 1975.
  - [Gol51] Goldhaber, M. and Sunyar, A.W. Classification of nuclear isomers. *Phys. Rev.*, 83:906–918, 1951.
  - [Hon02] Honma, M., et al. Effective interaction for pf-shell nuclei. *Phys. Rev. C*, 65:061301, 2002.
  - [Jaq84] Jaqaman, H.R. and Zamick, L. High multipole moments in nuclei. *Phys. Rev. C*, 30:1719–1730, 1984.
  - [Jul59] Juliano, J.O., et al. Disintegration of iron-52 and iron-53. *Phys. Rev.*, 113:602–608, 1959.
  - [Jun08] Junde, H. Nuclear data sheets for A = 55. *Nuclear Data Sheets*, 109(4):787 – 942, 2008.

- 
- [Jun09] Junde, H. Nuclear data sheets for A = 53. *Nuclear Data Sheets*, 110(11):2689 – 2814, 2009.
- [Kib08] Kibédi, T., et al. Evaluation of theoretical conversion coefficients using BrIcc. *Nuclear Instruments and Methods in Physics Research Section A: Accelerators, Spectrometers, Detectors and Associated Equipment*, 589(2):202 – 229, 2008.
- [Kno10] Knoll, G. *Radiation Detection and Measurement*. John Wiley & Sons, 2010.
- [Kra87] Krane, K. *Introductory Nuclear Physics*. Wiley, 1987.
- [Kuo68] Kuo, T. and Brown, G. Reaction matrix elements for the 0f – 1p shell nuclei. *Nuclear Physics A*, 114(2):241 – 279, 1968.
- [Kut78] Kutschera, W., Brown, B.A., and Ogawa, K. The empirical  $(1f_{7/2})^n$  model. *La Rivista del Nuovo Cimento (1978-1999)*, 1(12):1–116, 1978.
- [Law80] Lawson, R. *Theory of the nuclear shell model*. Oxford Studies in Nuclear Physics Series. Clarendon Press, 1980.
- [Lig83] Lightbody, J.W., et al. Elastic and inelastic electron scattering from  $^{50,52,54}\text{Cr}$ . *Phys. Rev. C*, 27:113–132, 1983.
- [May49] Mayer, M.G. On closed shells in nuclei. II. *Phys. Rev.*, 75:1969–1970, 1949.
- [McC75] McCallum, G.J. and Coote, G.E. Influence of source-detector distance on relative intensity and angular correlation measurements with Ge(Li) spectrometers. *Nuclear Instruments and Methods in Physics Research*, 130(1):189 – 197, 1975.
- [Met81] Metsch, B. and Glaudemans, P. Spectroscopic properties and collective structure from a shell-model description of A = 53 nuclei. *Nuclear Physics A*, 352(1):60 – 82, 1981.
- [Nel73] Nelson, R., et al. Study of low-lying levels of  $^{53}\text{Fe}$ . *Nuclear Physics A*, 215(3):541 – 556, 1973.

- 
- [Oue13] Ouellet, C. and Singh, B. Nuclear data sheets for A=31. *Nuclear Data Sheets*, 114(2):209 – 396, 2013.
  - [Pal17] Palazzo, T. High-spin spectroscopy and shell-model interpretation of the N < 126 radium isotopes  $^{212}\text{Ra}$  and  $^{213}\text{Ra}$ . *Nuclear Physics A*, 2017.
  - [Pov81] Poves, A. and Zuker, A. Theoretical spectroscopy and the fp shell. *Physics Reports*, 70(4):235 – 314, 1981.
  - [Rad95] Radford, D. ESCL8R and LEVIT8R: Software for interactive graphical analysis of HPGe coincidence data sets. *Nuclear Instruments and Methods in Physics Research Section A: Accelerators, Spectrometers, Detectors and Associated Equipment*, 361(1-2):297–305, 1995.
  - [Ric91] Richter, W., et al. New effective interactions for the 0f1p shell. *Nuclear Physics A*, 523(2):325 – 353, 1991.
  - [Rie05] Rietz, R.d., et al. Investigation of high-spin states in  $^{53}\text{Fe}$ . *Phys. Rev. C*, 72:014307, 2005.
  - [Sag79] Sagawa, H. Core polarization charge for E6 transition. *Phys. Rev. C*, 19:506–510, 1979.
  - [Saw73] Sawa, Z.P. On  $1\text{f}_{7/2}$  nuclei. gamma ray spectroscopic studies on states in  $^{53}\text{Mn}$  and  $^{53}\text{Fe}$  using the  $^{50}\text{Cr} + \alpha$  reaction. *Physica Scripta*, 7(1-2):5, 1973.
  - [Soo95] Sood, P.C., Sheline, R.K., and Singh, B. Evidence for hexadecapole collectivity in closed-shell nuclei. *Phys. Rev. C*, 51:2798–2800, 1995.
  - [Stu92] Stuchbery, A., et al. Spectroscopy and shell model interpretation of high-spin states in the N = 126 nucleus  $^{214}\text{Ra}$ . *Nuclear Physics A*, 548(1):159 – 188, 1992.
  - [Ur98] Ur, C.A., et al. Excited states in  $^{52}\text{Fe}$  and the origin of the yrast trap at  $I^\pi = 12^+$ . *Phys. Rev. C*, 58:3163–3170, 1998.
  - [Vau72] Vautherin, D. and Brink, D.M. Hartree-fock calculations with skyrme's interaction. I. spherical nuclei. *Phys. Rev. C*, 5:626–647, 1972.

- [Wil85] Wildenthal, B.H., Brown, B.A., and Sick, I. Electric hexadecupole transition strength in  $^{32}\text{S}$  and shell-model predictions for E4 systematics in the sd shell. *Phys. Rev. C*, 32:2185–2188, 1985.
- [Xia06] Xiaolong, H. Nuclear data sheets for  $A = 51$ . *Nuclear Data Sheets*, 107(8):2131 – 2322, 2006.
- [Yok97] Yokoyama, A. Two-body part of effective transition operators and higher-multipole transitions in the  $1\text{f}_{7/2}$ -shell nuclei. *Phys. Rev. C*, 55:1282–1287, 1997.